

Frank Knappe

---

**Waveguide structuring and Bragg grating  
fabrication by ultraviolet light induced  
refractive index changes in photosensitive  
optical materials**

---



Cuvillier Verlag Göttingen

# **Waveguide structuring and Bragg grating fabrication by ultraviolet light induced refractive index changes in photosensitive optical materials**

Vom Promotionsausschuss der  
Technischen Universität Hamburg-Harburg  
zur Erlangung des akademischen Grades  
Doktor-Ingenieur (Dr.-Ing.)  
genehmigte Dissertation

von  
Frank Knappe  
aus Hagenow

2006

## **Bibliografische Information Der Deutschen Bibliothek**

Die Deutsche Bibliothek verzeichnet diese Publikation in der Deutschen Nationalbibliografie; detaillierte bibliografische Daten sind im Internet über <http://dnb.ddb.de> abrufbar.

1. Aufl. - Göttingen : Cuvillier, 2007

Zugl.: (TU) Hamburg-Harburg, Univ., Diss., 2006

978-3-86727-414-2

1. Gutachter: Prof. Dr. Ernst Brinkmeyer, TU Hamburg-Harburg

2. Gutachter: Prof. Dr.-Ing. habil. Jörg Müller, TU Hamburg-Harburg

Tag der mündlichen Prüfung: 20. 12. 2006

© CUVILLIER VERLAG, Göttingen 2007

Nonnenstieg 8, 37075 Göttingen

Telefon: 0551-54724-0

Telefax: 0551-54724-21

[www.cuvillier.de](http://www.cuvillier.de)

Alle Rechte vorbehalten. Ohne ausdrückliche Genehmigung des Verlages ist es nicht gestattet, das Buch oder Teile daraus auf fotomechanischem Weg (Fotokopie, Mikrokopie) zu vervielfältigen.

1. Auflage, 2007

Gedruckt auf säurefreiem Papier

978-3-86727-414-2

For my family and friends



# Acknowledgement

Although it is the nature of a PhD thesis that I'm the sole author of this work, I couldn't have done it without the help of a lot of people. First of all, I would like to thank Prof. Dr. Ernst Brinkmeyer for giving me the opportunity to work in his group, for his helpful inspiration and for countless discussions and explanations.

I am very grateful to all the people I worked with in the "Optical Communication Technology" research group for their valuable contributions and creating a great and stimulating working atmosphere. Especially I want to thank Sven Kieckbusch for his support on Bragg grating characterization, Christian Knothe for his valuable expertise in opto-mechanical engineering, Michael Krause for numerous support and Hagen Renner for critical proof reading of paper submissions. Special thanks goes to Hartmut Gieseler, Jörg Voigt and Tim Pakendorf for their advice and help in bringing my ideas into reality. I would also like to acknowledge Arndt Monicke, Ingrid Böttcher, Holger Lizkowski, Florian Dürr, Knut Hildebrandt, Frauke Martens, Jens Naujokat, Marco Alke, Friedher Rumpel and Oliver Pabst for their commitment during their Studien- and Diplomarbeiten.

A significant part of this thesis was done within the framework of the European research project PLATON. I would like to acknowledge Isabel Riant and Marc Douay for their role as coordinators. I also want to thank all the people involved in this project, especially Bertrand Poumellec, Elena Billi, Hans Limberger, Claudia Aichele and Dieter Werner. A very special thanks goes to the organizers of the project meetings.

I would like to thank Yvonne Menke and Jörg Gehler for their collaboration on bulk glasses and UV trimming of arrayed waveguide gratings, respectively.

Ein ganz herzlicher Dank gebührt meinen Eltern, Waltraud und Helmuth Knappe, die mich auf all meinen Wegen sowohl finanziell, als auch in allen weiteren Belangen, immer unterstützt haben. In the same way my deepest thanks goes to my sister, Dorit Knappe, for her moral support and lots of help in non-scientific related areas.

And last but not least I would like to thank all of my friends.

*Livingston, July 2007*

*Frank Knappe*



# Contents

<b>1. Introduction</b>	<b>1</b>
<b>2. Waveguide and Bragg grating theory</b>	<b>5</b>
2.1. Optical waveguide theory . . . . .	5
2.2. Coupled mode theory . . . . .	7
2.2.1. Directional couplers . . . . .	7
2.2.2. Bragg gratings . . . . .	9
<b>3. Mechanisms of UV-induced refractive index changes</b>	<b>12</b>
3.1. Origins of photosensitivity . . . . .	12
3.1.1. Color-center model . . . . .	13
3.1.2. Compaction model . . . . .	13
3.2. Techniques for photosensitivity enhancement . . . . .	14
3.3. Conclusion . . . . .	15
<b>4. Measurement techniques</b>	<b>16</b>
4.1. Introduction . . . . .	16
4.2. Visual inspection of waveguide structures . . . . .	16
4.3. Transmission/Losses . . . . .	17
4.4. Mode field . . . . .	17
4.5. UV-induced refractive index changes . . . . .	19
4.5.1. Linnik interferometer . . . . .	19
4.5.2. Refracted near-field method . . . . .	21
4.5.3. Other techniques . . . . .	23
4.6. Group delay and chromatic dispersion . . . . .	24
4.7. Spatial reconstruction of Bragg gratings . . . . .	26
4.8. Conclusion . . . . .	27
<b>5. Direct UV-writing of waveguide structures</b>	<b>29</b>
5.1. Motivation . . . . .	29
5.2. UV writing setup . . . . .	31

## Contents

5.3. Material systems used . . . . .	33
5.4. Building blocks . . . . .	34
5.4.1. Straight waveguides . . . . .	34
5.4.2. S-bends . . . . .	40
5.4.3. Directional couplers . . . . .	41
5.5. Multi-mode interference couplers . . . . .	43
5.5.1. Motivation . . . . .	43
5.5.2. Experimental setup . . . . .	45
5.5.3. Results . . . . .	46
5.6. UV-induced refractive index changes in germanium-free materials	47
5.6.1. Material preparation and UV-writing . . . . .	47
5.6.2. Results . . . . .	48
5.7. Waveguide structuring by means of UV-induced refractive index decreases . . . . .	53
5.7.1. MDECR reactor and performance . . . . .	53
5.7.2. Photosensitivity experiments . . . . .	55
5.7.3. Photosensitivity mechanisms . . . . .	58
5.7.4. Waveguide structuring . . . . .	67
5.8. UV-written waveguides in bulk materials . . . . .	71
5.8.1. Motivation . . . . .	71
5.8.2. Preparation/Description of the material . . . . .	74
5.8.3. Vertical slab waveguide inscription . . . . .	75
5.8.4. Channel waveguide inscription . . . . .	78
5.9. UV-Trimming of arrayed waveguide gratings . . . . .	81
5.9.1. Motivation . . . . .	82
5.9.2. Trimming procedure . . . . .	83
5.9.3. Trimming results . . . . .	85
5.10. Conclusion . . . . .	87
<b>6. Design and realization of Bragg gratings</b>	<b>88</b>
6.1. Introduction . . . . .	88
6.2. Bragg gratings for add/drop-multiplexer . . . . .	90
6.3. Bragg grating design by layer-peeling algorithm . . . . .	92
6.3.1. Commercial Bragg grating design program . . . . .	92
6.3.2. Spectrally assisted layer-peeling algorithm . . . . .	95
6.4. Bragg grating design by optimization algorithm . . . . .	99
6.4.1. Algorithm . . . . .	99

6.4.2. Designs . . . . .	101
6.5. Writing setup . . . . .	106
6.6. Realization in fibers . . . . .	107
6.6.1. Bragg gratings without $\pi$ -phase shifts . . . . .	108
6.6.2. Bragg gratings with $\pi$ -phase shifts . . . . .	111
6.7. Realization in channel waveguides . . . . .	113
6.8. Conclusion . . . . .	117
<b>7. Conclusion</b>	<b>118</b>
<b>A. Photosensitivity of amorphous aluminium oxide</b>	<b>121</b>
A.1. Motivation . . . . .	121
A.2. Results . . . . .	122
<b>B. Thermal stability of directly UV-written waveguides</b>	<b>125</b>
<b>C. Fiber Bragg grating characterization by OSD</b>	<b>127</b>
C.1. Motivation . . . . .	127
C.2. Measurement principle . . . . .	128
C.3. Experiments . . . . .	129
C.4. Results and discussion . . . . .	130
C.5. Conclusion . . . . .	132
<b>D. Sample data</b>	<b>134</b>
<b>List of publications</b>	<b>137</b>
<b>Bibliography</b>	<b>140</b>

## **Abstract**

The refractive index of photosensitive optical materials can be permanently changed by UV-irradiation. With a focussed UV-laser beam refractive index increases and decreases are realized in a variety of different materials and are employed to structure waveguides or to postprocess optical devices. Another important application for UV-induced refractive index changes are Bragg gratings in optical waveguides. Low chromatic dispersion Bragg gratings are designed and afterwards fabricated by using a holographic writing setup.

## **Kurzfassung**

Die Brechzahl von photosensitiven optischen Materialien kann durch UV-Bestrahlung permanent verändert werden. Mit Hilfe eines fokussierten Laserstrahls werden Brechzahlerhöhungen und -erniedrigungen in verschiedenen Materialien erzielt und für die Strukturierung von Wellenleitern und die Nachbehandlung von optischen Komponenten verwendet. Ein zweites wichtiges Anwendungsgebiet für Brechzahländerungen sind Bragg-Gitter in optischen Wellenleitern. Bragg Gitter mit geringer chromatischer Dispersion werden entworfen und mit Hilfe eines holographischen Herstellungsverfahrens realisiert.

## Summary

The refractive index of photosensitive optical materials can be permanently changed by UV-irradiation. The objective of this thesis was to use such refractive index changes for the fabrication of waveguides and Bragg gratings.

Integrated optics allows for the integration of optical functionality on a small footprint. A technique to realize integrated optical waveguides is the direct writing technique where a focussed UV-laser is scanned over a photosensitive sample. This fabrication method is of particular interest as no mask technology is involved, which is advantageous during the prototyping phase of new devices. UV-induced refractive index changes in excess of  $10 \times 10^{-3}$  were achieved in hydrogen-loaded germanium-doped silica layers and employed to fabricate straight waveguides, S-bends, directional couplers and multi-mode interference couplers. In one of the tested material systems the refractive index was decreased by the UV-irradiation rather than increased. Without any presensitization refractive index changes down by  $-10 \times 10^{-3}$  were observed. Waveguides were realized in this material system by the negative direct writing technique, i. e. the waveguide cladding instead of the core was written. The fabrication of waveguide structures by UV-induced refractive index changes is not limited to layered material systems as described so far. Directly UV-written buried X-shaped waveguides in a bulk multicomponent silicate glass have been produced by a special X-shaped writing geometry. As an example for the use of UV-induced refractive index changes for the post processing of optical devices the crosstalk in an arrayed waveguide grating was significantly reduced.

Bragg gratings play a crucial role in modern optical communication systems. One interesting application area is the use as narrow-band channel filters in add/drop-multiplexers, where low chromatic dispersion values in reflection and transmission are required. Different design procedures were employed for the design of such Bragg grating structures. An optimization algorithm allowed for the consideration of constraints imposed by the writing facility which is later used for the fabrication. Bragg gratings of different lengths with and without  $\pi$ -phase shifts were designed. The designed Bragg gratings were fabricated afterwards by using a holographic writing setup which enables full control over local grating strength and period.



# 1. Introduction

In the last decade there has been an astounding growth in the data transmission capacity over optical fibers. The majority of this growth is based on the increasing popularity of the internet and its use for a myriad of different applications. These applications, like television or games, triggered the demand for high data rate access to the provided data or content. 100 Mbit/s connections are now available for private households and even over mobile channels data rates in excess of 10 Mbit/s are possible. In order to allow for such high transmission rates in the access networks efficient back bones are necessary. For this task optical communication systems have been proven superior to any other technology. The main advantage of optical transmission systems is the high carrier frequency of  $\sim 200$  THz, which is several orders of magnitude higher than used in microwave based transmission systems ( $\sim 10$  GHz). This results in a larger usable bandwidth. Therefore all major telecommunication links are now based on optical technologies.

Several technological breakthroughs mark the development of optical communication systems during the last nearly 50 years [19]. The invention of the laser by Maiman in 1960 [20] was the starting point for the development of the semiconductor laser diodes, which are employed as transmitters in today's fiber optic networks. The use of optical fibers as transmission medium was proposed in 1966 [21] and in 1979 the low predicted losses of 0.2 dB/km at 1550 nm were achieved [22].

An amplification of the optical signals is necessary after approximately every 100 km even with these low loss levels. Until the end of the 1980s this was achieved by optoelectronic repeaters, where the optical signal is first converted into an electrical signal, amplified and then sent again using a laser diode. As this approach works on a per-channel basis such regenerators become quite expensive for transmission systems with several wavelength channels (WDM: wavelength division multiplex). With the invention of the erbium-doped fiber amplifier in 1987 [23] the direct amplification of optical signals without requiring its conversion into the electrical domain was made possible. Such optical

## 1. Introduction

amplifiers offer a broad amplification bandwidth (up to 100 nm) and the amplification is independent of the data rate and modulation format. Ultra long haul transmission systems in excess of 10000 km length have been realized with the help of such amplifiers.

There are still electrical components at the beginning and at the end of each optical transmission system. Their maximum modulation frequencies currently limit the data rate in the electrical domain to 40 Gbit/s. In order to go beyond these limits imposed in the electrical domain several multiplexing schemes are used. With the combination of optical time domain multiplexing (OTDM) and polarization multiplexing a transmission at 2.56 TBit/s within a single wavelength channel has been reported [24]. Even higher data rates over a single fiber have been achieved with a wavelength division multiplexing scheme. By using more than 250 wavelength channels, each modulated with 40 Gbit/s, a total transmission capacity of nearly 11 TBit/s has been demonstrated in laboratory experiments [25, 26].

Older fibers still have an absorption peak at 1.4  $\mu\text{m}$  due to OH-contamination. New fabrication methods have eliminated this loss contribution and fibers with losses below 0.3 dB/km from 1300 to 1700 nm are now available [27]. This broad region with low losses results in a usable transmission window in excess of 50 THz. Optical amplification can be achieved in this full wavelength range by the combined use of rare earth doped fiber amplifiers and raman amplification [28].

At the moment the majority of the network management functionality is still realized in the electrical domain. One of the current challenges is to develop components for an all-optical network [29], where routing and switching is implemented in the optical domain. Only a few passive functions can be realized directly in optical fibers. The most notable examples for this are filters based on fiber Bragg gratings or long period gratings. Devices built out of bulk elements with interconnections realized by fibers are both expensive and unstable due to the possibility of misalignment. Therefore, as early as 1969, the concept of *integrated optics* in analogy to the *integrated electronics* was proposed [30]. By the monolithic or hybrid integration of active and passive components onto a common substrate the required functionalities can be realized on a small footprint.

Several material systems are used in the area of integrated optics, for instance silica-on-silicon, silicon on insulator, indium phosphide or polymers. The waveguiding structures are subsequently defined by photolithography and etching

processes. In this way, complex planar lightwave circuits of a high quality can be fabricated [31].

The most widely used material for the core of both planar optical waveguides and fibers is germanium-doped silica. A variety of passive components have been realized with this material system. By incorporating active elements like Erbium, active components, e. g. amplifiers or lasers, have been fabricated using germanium-doped silica as host material. In addition to this it exhibits refractive index changes upon irradiation with green/blue or UV light [32, 33]. This photosensitivity is widely used today.

The main application area for UV-induced refractive index changes is the fabrication of fiber Bragg gratings. They are used for a variety of different applications, ranging from channel dropping filters, gain equalization elements, dispersion compensators up to sensors. The task is first to design a spatial grating structure suited for the application under consideration and finally to fabricate it.

The UV-induced refractive index changes can be large enough to form the core of an optical waveguide. Based on this finding the direct writing technique (DWT) was developed by Svalgaard et al. in 1994 [34]. Since then waveguide structures and even complete devices have been realized with this technique. Also different material systems have been probed in order to test their potential as host material for the DWT. The challenge is to find materials in which the desired functionalities can be fabricated with low losses. Another application area of UV-induced refractive index changes is the post processing of optical devices, where either the characteristics or the fabrication yield is improved. Compared to other trimming procedures no cleanroom processes are required nor is there any permanent power consumption during the life time of the device.

The main objective of this work was to investigate the use of UV-induced refractive index changes in the area of optical communication technology. This includes the structuring of planar optical waveguides and fabrication of Bragg gratings. The thesis is structured as follows:

Chapter 2 describes the basic theories about waveguides and Bragg gratings, which are needed for the understanding of this thesis.

Chapter 3 gives a brief overview about the origins of the UV-photosensitivity, which is exploited for the refractive index changes obtained in this thesis. Also explained are techniques for the enhancement of the photosensitivity.

In chapter 4 the measurement techniques for the UV-written waveguide

## *1. Introduction*

structures and Bragg gratings are presented. The principles behind the methods used are explained and exemplary results are shown.

Chapter 5 forms the main part of this thesis. It is shown how UV-induced refractive index changes can be exploited for the patterning of waveguide structures. The direct writing technique is introduced and results obtained with different material systems are presented. In hydrogen-loaded germanium-doped silica layers straight waveguides, S-bends, directional couplers and multi-mode interference couplers were fabricated and characterized. In one of the tested material systems the UV-irradiation yielded a decrease of the refractive index. For this material system several experiments were performed in order to explain this behavior and the contribution of the different mechanisms involved will be discussed. The fabrication of waveguide structures by UV-induced refractive index changes is not limited to layered material systems. Results obtained with different multicomponent silicate glasses are reported and a specially developed writing technique for the realization of buried channel waveguides in bulk materials is presented. At the end of this chapter the use of UV-induced refractive index changes for the post processing of optical devices is shown.

Chapter 6 deals with the design and fabrication of Bragg gratings in optical waveguides. Three different approaches for the design of low-dispersion Bragg gratings are presented and the results obtained with them are compared. By using a holographic writing setup these designs are afterwards written in optical fibers and planar waveguides. The measured transmission and reflection properties are compared with the required specifications and possible origins for discrepancies are discussed.

The results obtained within the framework of this thesis are summarized in chapter 7. In addition an outlook regarding possible future work is given.

## 2. Waveguide and Bragg grating theory

In this chapter the necessary theoretical background for the understanding of the propagation of electromagnetic waves in single waveguides and coupled waveguide structures will be presented. From the refractive index distribution of waveguides it is possible to obtain the propagating mode fields. These mode fields make the calculation of coupling losses between different waveguides possible. The coupling of modes will be explained for the special cases of directional couplers and Bragg gratings. For the latter the transfer matrix method will be presented as a fast method used for the calculation of reflection and transmission spectra for Bragg gratings with arbitrary coupling coefficients.

### 2.1. Optical waveguide theory

In homogeneous media ( $\nabla \varepsilon = 0$ ) electromagnetic waves obey the wave equation

$$\left[ \nabla^2 - \mu \varepsilon \frac{\partial^2}{\partial t^2} \right] \tilde{\mathbf{E}}(x, y, z, t) = 0 \quad (2.1)$$

which follows directly from Maxwell's equations.  $\mu = \mu_r \mu_0$  and  $\varepsilon = \varepsilon_r \varepsilon_0$  represent the permeability and dielectric constant of the material. For all the materials inside this thesis they are assumed to be scalar values (isotropic material). Furthermore no sources ( $\nabla \cdot \tilde{\mathbf{E}} = 0$ ) are present.

For monochromatic waves the following ansatz  $\tilde{\mathbf{E}}(x, y, z, t) = \mathbf{E}(x, y, z) e^{j\omega t}$  can be made in order to transform the wave equation into the Helmholtz equation.

$$[\nabla^2 - \omega^2 \mu \varepsilon] \mathbf{E}(x, y, z) = 0 \quad (2.2)$$

Solutions of this equation which propagate along the longitudinal  $z$  direction as  $\exp(-j\beta z)$  are called modes and  $\beta$  is the corresponding propagation constant.

For weakly guiding waveguides such as fibers or UV-written waveguides, the field is linearly polarized as  $\mathbf{E} \simeq \hat{\mathbf{s}}\psi(x, y)$ , where  $\hat{\mathbf{s}}$  is a unit vector in the  $(x, y)$  plane transverse to the propagation direction of the waveguide. For a waveguide

## 2. Waveguide and Bragg grating theory

with a transverse refractive index profile  $n(x, y)$ , the scalar mode field  $\psi(x, y)$  obeys the wave equation,

$$\frac{\partial^2 \psi}{\partial x^2} + \frac{\partial^2 \psi}{\partial y^2} + [k^2 n^2(x, y) - \beta^2] \psi = 0, \quad (2.3)$$

where  $k = 2\pi/\lambda$ , and  $\lambda$  is the wavelength.

The solutions  $\psi(x, y)$  of eq. (2.3) depend on the transverse refractive index profile  $n(x, y)$ . For a circularly symmetric step-index fiber the solutions can be given in terms of Bessel functions  $J_m$  and  $K_m$ . In particular the fundamental mode is given by

$$\psi_{01}(x, y) = \begin{cases} \frac{J_0(U_{01}r/\rho)}{J_0(U_{01})} & 0 < r = \sqrt{x^2 + y^2} < \rho \\ \frac{K_0(W_{01}r/\rho)}{K_0(W_{01})} & \rho < r < \infty. \end{cases} \quad (2.4)$$

with  $U_{01} = \rho\sqrt{k^2 n_1^2 - \beta_{01}^2}$  and  $W_{01} = \rho\sqrt{\beta_{01}^2 - k^2 n_2^2}$ .

For non-circular waveguides such as UV-written channel waveguides, the field of the fundamental mode can be well approximated by a two-dimensional Gaussian function,

$$\psi_{01}(x, y) = \exp \left\{ - \left( \frac{x^2}{w_x^2} + \frac{y^2}{w_y^2} \right) \right\}. \quad (2.5)$$

A more detailed analysis of the modes of UV-written waveguides is given in [35]. For circular fibers the Gaussian approximation is also applicable and the mode spot sizes  $w_x$  and  $w_y$  are equal.

The knowledge of the mode fields  $\psi_1$  and  $\psi_2$  of two waveguides 1 and 2 allows for the estimation of the transition loss at the connection of the two waveguides. It follows from the field overlap integral

$$\eta = \frac{(\int \int \psi_1 \psi_2 dx dy)^2}{\int \int \psi_1^2 dx dy \int \int \psi_2^2 dx dy}. \quad (2.6)$$

The coupling efficiency  $\eta$  between a circular fiber with  $w_x = w_y = w_0$  and a waveguide with spot sizes  $w_x$  and  $w_y$  follows from eq. (2.5) and (2.6) as

$$\eta = \frac{4w_0^2 w_x w_y}{(w_0^2 + w_x^2)(w_0^2 + w_y^2)}. \quad (2.7)$$

## 2.2. Coupled mode theory

This formula will be used later for the calculation of coupling losses between a fiber and the UV-written waveguides. These losses are obviously smaller the closer  $w_x$  and  $w_y$  are to  $w_0$ . Differences of the field radii up to 20% (in both dimensions), however, only result in an insertion loss of 0.2 dB.

Knowledge of the fundamental mode field also enables the calculation of the form birefringence

$$B = \frac{\beta_x - \beta_y}{k} = n_{\text{eff},x} - n_{\text{eff},y}, \quad (2.8)$$

i. e. the difference of the propagation constants between the two orthogonally polarized states of the fundamental mode. Form birefringence occurs if the waveguide geometries along the  $x$  and  $y$  dimensions are different. In a circular fiber and all other waveguides with  $w_x = w_y$ , there is no form birefringence. Using a perturbation method and the Gaussian field approximation eq. (2.5), the form birefringence can be approximated by [36]

$$B = \frac{1}{2k^4 n_{\text{cl}}^3} \left( \frac{1}{w_y^4} - \frac{1}{w_x^4} \right). \quad (2.9)$$

with  $n_{\text{cl}}$  as the refractive index of the waveguide cladding [36].

It should be noted that the total birefringence is composed of an amount of form birefringence and an amount caused by material anisotropy such as stress birefringence in systems of materials with different thermal expansion coefficients.

## 2.2. Coupled mode theory

For the case of unperturbed waveguides as discussed above no interaction between different propagating modes takes place. This situation is different if there is a periodic dielectric perturbation. In such cases a power exchange between different modes is possible. The amount of coupling depends on the difference between the propagation constants of the participating modes as well as on the strength of the coupling effect [37].

### 2.2.1. Directional couplers

The layout of a directional coupler is shown in Fig. 5.10. If the distance between the two parallel waveguides is small enough, optical energy can be transferred

## 2. Waveguide and Bragg grating theory

from one to the other. This takes place by synchronous coherent coupling between the overlapping evanescent tails of the guided mode fields.

Let  $\psi_{a,b}$  be the modes of the individual waveguides, when they are far apart. The electric field of the coupled structure can be approximated by

$$E(x, y, z, t) = A(z)\psi_a(x, y)e^{j(\omega t - \beta_a z)} + B(z)\psi_b(x, y)e^{j(\omega t - \beta_b z)}, \quad (2.10)$$

if the two waveguides are not too close to each other. The terms  $A$  and  $B$  describe the complex amplitudes of the modes in the individual waveguides. The coupling between these modes can then be described by the following equations [37]:

$$\begin{aligned} \frac{d}{dz}A &= -j\kappa_C B e^{-j2\delta z} \\ \frac{d}{dz}B &= -j\kappa_C^* A e^{j2\delta z}, \end{aligned} \quad (2.11)$$

with  $2\delta$  as the phase match given by

$$2\delta = (\beta_a + \kappa_{aa}) - (\beta_b + \kappa_{bb}). \quad (2.12)$$

The terms  $\kappa_{aa}$  and  $\kappa_{bb}$  account for the correction of the original propagation constants  $\beta_a, \beta_b$  due to the presence of the other waveguide. The value of  $\kappa_C$  determines the strength of the coupling and is determined by the interaction of the fields in both waveguides, i. e. by the refractive index profile of the full structure [37].

For the boundary conditions  $P_a(0) = P_0$  and  $P_b(0) = 0$  the power evolution in each waveguide is given by

$$\begin{aligned} P_b(z) &= P_0 \frac{\kappa_C^2}{\kappa_C^2 + \delta^2} \sin^2\left(\sqrt{\kappa_C^2 + \delta^2} z\right) \\ P_a(z) &= P_0 - P_b(z) \end{aligned} \quad (2.13)$$

From these equations it follows that a total transfer of power from one waveguide to the other is only possible if  $\delta = 0$ , which means the propagation constants in both waveguides are the same. In order to get this full power transfer the interaction length has to be an odd multiple of  $L_\pi = \pi/2\kappa_C$ . For  $\delta \neq 0$  the maximum power transfer is

$$\frac{\kappa_C^2}{\kappa_C^2 + \delta^2}. \quad (2.14)$$

## 2.2. Coupled mode theory

Results obtained with UV-written directional couplers will be presented in section 5.4.3.

### 2.2.2. Bragg gratings

From a macroscopic model a Bragg grating can be seen as a periodic modulation (grating period  $\Lambda$ ) of the core refractive index. Each of these index steps act as a dielectric mirror to the incident wave and according to the Fresnel formulae reflect a small portion of it, see Fig. 2.1. If the wavelength  $\lambda$  of the incoming irradiation equals half the optical distance between two of such index steps, the Bragg condition

$$\lambda = \lambda_{\text{Bragg}} = 2n_{\text{eff}}\Lambda \quad (2.15)$$

is fulfilled. At this given wavelength a significant amount of the incident power is reflected by the grating structure through constructive interference of the individual reflected waves.

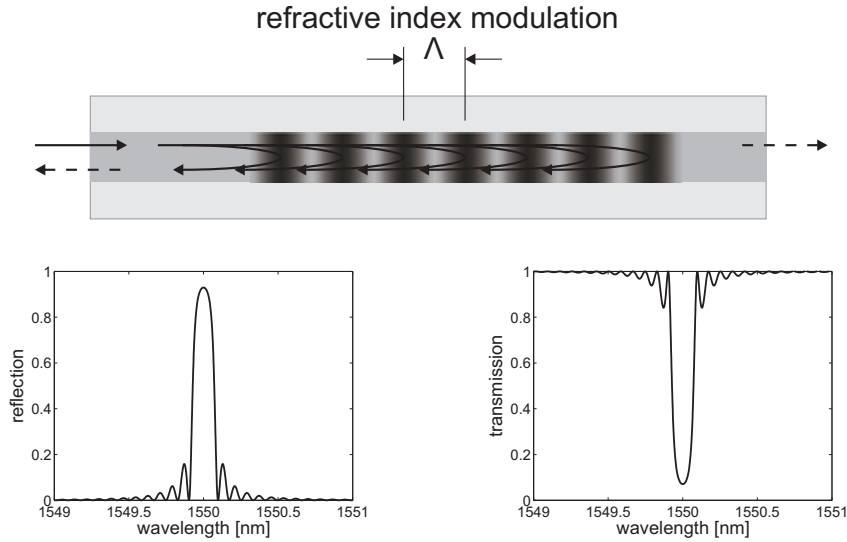


**Figure 2.1.:** Descriptive explanation of the spectral behavior of Bragg gratings.

The two modes involved in this coupling mechanism are propagating in opposite directions:

$$E(x, y, z, \tilde{\nu}) = \left[ E^+(z, \tilde{\nu})e^{-j\beta z} + E^-(z, \tilde{\nu})e^{j\beta z} \right] \psi_{01}(x, y). \quad (2.16)$$

## 2. Waveguide and Bragg grating theory

The term  $\tilde{\nu}$  is a normalized spatial frequency and describes the difference between the optical wavelength  $\lambda$  and the mean grating period  $\bar{\Lambda}$ .

$$\tilde{\nu} = \frac{1}{\lambda/2n_{\text{eff}}} - \frac{1}{\bar{\Lambda}} \quad (2.17)$$

The coupled mode equations for the amplitudes  $E^+(z, \tilde{\nu})$  and  $E^-(z, \tilde{\nu})$  for this case become

$$\begin{aligned} \frac{\partial E^-(z; \tilde{\nu})}{\partial z} &= \kappa(z) E^+(z; \tilde{\nu}) e^{-j2\pi\tilde{\nu}z} \\ \frac{\partial E^+(z; \tilde{\nu})}{\partial z} &= \kappa^*(z) E^-(z; \tilde{\nu}) e^{+j2\pi\tilde{\nu}z}. \end{aligned} \quad (2.18)$$

The complex coupling coefficient  $\kappa(z)$  determines the characteristics of the grating. Its modulus  $|\kappa|$  is given by the magnitude  $\delta n_G$  of the index modulation and its phase  $\phi_\kappa$  by the difference between the local grating period  $\Lambda(z)$  and the mean grating period  $\bar{\Lambda}$ .

$$\kappa(z) = |\kappa(z)| \cdot \exp[-j\phi_\kappa(z)] \quad (2.19)$$

$$|\kappa| = \eta_{UV} \cdot \frac{\pi\delta n_G}{\lambda} \quad (2.20)$$

$$\frac{1}{2\pi} \frac{d\phi_\kappa}{dz} = \frac{1}{\Lambda(z)} - \frac{1}{\bar{\Lambda}} \quad (2.21)$$

The factor  $\eta_{UV}$  describes the overlap of the transverse refractive index modulation with the fundamental mode field. For fibers a typical value is  $\eta_{UV} \sim 0.8$ .

For the special case of a uniform Bragg grating, i. e.  $|\kappa|$  and  $\Lambda$  are constant over the grating length  $L$ , it is possible to solve the differential equations (2.18) analytically. If  $E_0^+ = E^+(z=0; \tilde{\nu})$  and  $E^-(z=L; \tilde{\nu}) = 0$  the solutions for the complex reflection and transmission factors  $r(\tilde{\nu})$  and  $t(\tilde{\nu})$  are as follows:

$$\begin{aligned} r(\tilde{\nu}) &= E^-(z=0; \tilde{\nu})/E_0^+ = \frac{-j\kappa}{Q} \sinh(\gamma L) \\ t(\tilde{\nu}) &= E^+(z=L; \tilde{\nu})/E_0^+ = \frac{j\gamma}{Q} \end{aligned} \quad (2.22)$$

$$\text{with } \gamma = \sqrt{|\kappa|^2 - (\pi\tilde{\nu})^2}$$

$$\text{and } Q = -\pi\tilde{\nu} \sinh(\gamma L) + j\gamma \cosh(\gamma L).$$

## 2.2. Coupled mode theory

The two lower pictures in Fig. 2.1 show the reflection and transmission spectra of a uniform Bragg grating with approximately 90 % reflection.

As a Bragg grating can also be described as a 2-port device it is possible to describe the reflection and transmission properties by a scattering matrix  $\mathbf{S}$  and/or a transfer matrix  $\mathbf{T}$ . For a uniform Bragg grating of length  $L$  the elements of these two matrices are given by:

$$\mathbf{S} = \begin{pmatrix} S_{11} & S_{12} \\ S_{21} & S_{22} \end{pmatrix} = \frac{1}{Q} \begin{pmatrix} -j\kappa \sinh(\gamma L) & j\gamma \\ j\gamma & j\kappa^* \sinh(\gamma L) \end{pmatrix} \quad (2.23)$$

and

$$\mathbf{T} = \frac{1}{S_{12}} \begin{pmatrix} S_{21}S_{12} - S_{22}S_{11} & S_{22} \\ -S_{11} & 1 \end{pmatrix} = \begin{pmatrix} j\left(\frac{Q}{\gamma}\right)^* & \frac{\kappa^*}{\gamma} \sinh(\gamma L) \\ \frac{\kappa}{\gamma} \sinh(\gamma L) & -j\frac{Q}{\gamma} \end{pmatrix}. \quad (2.24)$$

This formalism is useful for the calculation of Bragg gratings with arbitrary values for the coupling coefficient  $\kappa(z)$ . The grating structure is divided into  $N$  small sections with a length  $\Delta L = L/N$ , in which  $\kappa(z)$  is kept constant [38]. The transfer matrix of the original structure is then obtained by the product of the transfer matrices of the individual sections:

$$\mathbf{T} = \mathbf{T}_N \mathbf{T}_{N-1} \dots \mathbf{T}_2 \mathbf{T}_1 \quad (2.25)$$

For weak gratings, i. e.  $\int_L |\kappa(z)| dz \ll 1$ , the complex reflection factor  $r(\tilde{\nu})$  is given by the Fourier transform of the complex coupling coefficient  $\kappa(z)$ .

$$r(\tilde{\nu}) = - \int_0^{L_g} \kappa(z) e^{-j2\pi\tilde{\nu}z} dz = -\mathcal{F}\{\kappa(z)\}. \quad (2.26)$$

The design and the fabrication of Bragg gratings in fibers and planar optical waveguides will be presented in Chapter 6.

### 3. Mechanisms of UV-induced refractive index changes

Although the photosensitivity of optical materials has been extensively studied over the last 20 years, there is still no unified theory about the chemical and physical mechanisms behind the refractive index changes. One explanation for the lack of a unified theory is that the photosensitive response may differ significantly depending on several factors such as the type of fiber, prior treatment of the fiber, UV writing wavelength and the UV laser writing power.

As the scope of this thesis is the use of UV-induced refractive index changes, only a brief overview about the origins of photosensitivity will be given. More detailed reviews about this topic can be found in the respective chapters of [39, 40] and their references within.

#### 3.1. Origins of photosensitivity

Due to the Kramers-Kronig causality principle, any change in refractive index is necessarily correlated to a change in the absorption spectrum of the material and vice versa. It is therefore possible to calculate refractive index changes from measured absorption coefficient changes [40]:

$$\Delta n(\lambda) = \frac{1}{2\pi^2} P_C \int_0^\infty \frac{\Delta\alpha(\lambda')}{1 - (\lambda'/\lambda)^2} d\lambda', \quad (3.1)$$

with  $P_C$  as the Cauchy principal value of the integral,  $\Delta\alpha(\lambda')$  as the absorption coefficient changes and  $\lambda$  as the wavelength at which the refractive index change is calculated.

The physical mechanisms responsible for these absorption changes include the creation and/or bleaching of color centers [41], mechanical effects like compaction of the material [42] or stress relief [43]. By determining the spectral positions of the absorption changes it is possible to identify the underlying

### 3.1. *Origins of photosensitivity*

physical processes and their corresponding contribution to the overall refractive index changes.

#### 3.1.1. **Color-center model**

There can only be light induced changes in the material properties, if there is an interaction between light and matter. For the case of the UV-photosensitivity this means that there has to be an absorption of the UV-light. Several absorption peaks in the UV-range have been detected and attributed to different defects of the glass matrix, the so called color-centers [44]. The most important color centers absorbing in the UV-range are the germanium oxygen deficient center (GODC) at  $5.1 \text{ eV} \approx 240 \text{ nm}$  and  $\text{GeE}'$  at  $6.4 \text{ eV} \approx 195 \text{ nm}$  [45].

The UV-irradiation yields a change of the absorption spectra; some absorption bands increase in strength, whereas others decrease. By measuring the absorption coefficient changes the resulting refractive index changes can be calculated using eq. (3.1). Refractive index changes as large as  $11 \times 10^{-3}$  in hydrogen-loaded fibers have been explained by this method [46]. In the same publication it was shown that the majority ( $\sim 50$  to  $95\%$ ) of the achieved refractive index changes comes from absorption changes in the  $165\text{--}195 \text{ nm}$  range.

However, not all measured refractive index changes can be explained by the color-center model. In section 5.7.3 refractive index changes down to  $-1.7 \times 10^{-3}$  will be explained by changes of the UV-absorption, whereas the measured refractive index changes have reached  $-10 \times 10^{-3}$ . At least one more effect must contribute to the photosensitivity phenomenon.

#### 3.1.2. **Compaction model**

The second model is based on structural changes of the glass matrix and was first proposed by Bernardin et al. [47]. These structural changes result in a compaction of the material and in an increase of the refractive index. The densification of thin silica films caused by UV-irradiation and resulting refractive index changes was already shown in [48]. In densified fused silica the UV-absorption edge as well IR-absorption peaks shifts towards longer wavelengths [49]. For germanosilicate glass a large absorption increase in the deep UV-range was reported after densification [50].

Based on these absorption changes the corresponding refractive index changes could be calculated using eq. (3.1). The absorption changes in the deep UV-

### 3. Mechanisms of UV-induced refractive index changes

range, however, are very difficult to measure and therefore a different approach is used for the calculation of refractive index changes caused by compaction.

Starting from the Lorentz-Lorenz relation it is possible to derive the refractive index changes caused by changes of the density ( $\rho$ ) / volume ( $V$ ) or polarizability ( $\alpha_P$ ) [51]:

$$\Delta n = \frac{(n^2 - 1)(n^2 + 2)}{6n} \cdot \left( \frac{\Delta \alpha_P}{\alpha_P} + \frac{\Delta \rho}{\rho} \right) \quad (3.2)$$

$$= \frac{(n^2 - 1)(n^2 + 2)}{6n} \cdot \left( \frac{\Delta \alpha_P}{\alpha_P} - \frac{\Delta V}{V} \right) \quad (3.3)$$

$$= \frac{(n^2 - 1)(n^2 + 2)}{6n} (\Omega - 1) \frac{\Delta V}{V} . \quad (3.4)$$

In this equation  $\Omega$  describes the change of polarizability caused by the volume change. The exact value for  $\Omega$  has to be found by fitting eq. (3.4) to measured refractive index changes. For fused silica a value of  $\Omega = 0.23$  was determined in [52].

A densification of a material is always accompanied by a change of stresses, which also leads to changes of the refractive index due to the photo-elastic effect. These index changes have a different sign and therefore yield a reduction of the index changes caused by the compaction or color-center changes [42]. The amount of the photo-elastic contribution can reduce the inelastic contribution by up to 50%. A detailed analysis of the contribution of UV-induced stress changes is given in [53].

## 3.2. Techniques for photosensitivity enhancement

A standard single-mode fiber (SSMF) only has a low photosensitivity. Several ways for enhancing the photosensitivity of optical waveguides have been presented in the past. One approach is to produce fibers with a higher photosensitivity, for instance by increasing the germanium concentration in the waveguide core. This, however, also increases the index step between core and cladding of an optical fiber, resulting in a smaller mode-field diameter and increasing splicing losses to SSMFs. This unwanted effect can be compensated for by a codoping with boron, because boron decreases the refractive index of the core. In addition, boron increases the photosensitivity [54]. A summary of the influ-

ence of other chemical elements on the photosensitivity is given in section 3.6 of [55].

In 1991 it was shown that an annealing of a fiber preform in a hydrogen atmosphere at 610 °C for 75 h increases the photosensitivity of the fibers drawn from this preform in comparison to fibers drawn from normal preforms [56]. A simple, low-cost and highly effective alternative to this method was reported by Lemaire et al. in 1993 [57, 58]. Fibers are put into an hydrogen atmosphere at room temperatures and pressures around 150 bar for approximately 10 days. This results in a diffusion of the hydrogen molecules into the fiber core and UV-induced refractive index changes of more than  $10^{-2}$  have been realized in such fibers. This method, the so called hydrogen-loading, is the most widely used photosensitivity enhancement method to date.

The hydrogen-loading technique, however, has the disadvantage that as soon as the fiber is taken out of the loading chamber, the outdiffusion of the hydrogen starts, resulting in a decrease of the photosensitivity over time. Several techniques have been developed in order to "freeze" the photosensitivity, even if the hydrogen is outdiffused. Examples are a low fluence fringeless UV pre-exposure [59, 60] or the OH-flooding, a rapid (1 s) heat treatment at 1000 °C [61].

### **3.3. Conclusion**

The origins of the UV-photosensitivity of optical materials are still not fully clarified and further work is needed to build a coherent theory. It is very likely that different mechanisms contribute to the measured UV-induced refractive index changes. Two of them, the color-center model and the compaction model, were briefly introduced in this chapter. In section 5.7.3 these two models will be applied in order to explain the unusual refractive index changes in UV-irradiated germanium-doped silica layers.

## **4. Measurement techniques**

### **4.1. Introduction**

In this chapter an overview of the measurement techniques which are used for the characterization of the components fabricated in the framework of this thesis will be given. For the UV-written waveguides this includes a visual inspection and the determination of losses, mode fields and refractive index profiles. The interesting properties for Bragg gratings are the transmission, reflection and the group delay spectra, which are obtained by wavelength scanning interferometry. By the combination of the Optical Frequency Domain Reflectometry and inverse scattering the spatial structure of fabricated Bragg gratings is obtained. A more detailed overview of the characterization methods for UV-written waveguides, Bragg gratings and grating based devices can be found in [1] and [2].

The characterization of the UV-written waveguides was performed on an optical bench. The samples under test were mounted on a two axis translation stage by means of a vacuum holder. On the input and output side two three-axis translation stages were used. The fiber-waveguide coupling was performed by a single-mode fiber positioned directly in front of the sample facet. Parasitic reflections at the fiber-air and air-waveguide interfaces were reduced by index matching oil. The outcoupling was either done with a second single-mode fiber or with a microscope objective.

### **4.2. Visual inspection of waveguide structures**

The majority of the UV-written structures presented within this thesis are clearly visible under an optical microscope. This enables a quick identification of imperfections or failures during the writing process. By launching HeNe laser light the existence of waveguides is checked. This procedure is also used as a coarse alignment for the next evaluation steps.

### **4.3. Transmission/Losses**

For measuring the transmission spectra of UV-written waveguides, fibers were used for the in- and outcoupling. By taking the transmission from the input to the output fiber as a reference, the insertion loss of the waveguide can be obtained. The insertion loss consists of two contributions: the fiber-waveguide coupling losses due to the mode mismatch (see the next section) and the propagation losses due to absorption, leakage or scattering.

Measurements between 1460 and 1640 nm were performed by using two different tuneable lasers. These laser sources offer a high spectral resolution (1 pm) and in connection with suitable power meters a dynamic range of better than 90 dB can be achieved. With the addition of an optical circulator this setup was also used for the measurement of the reflection spectra of Bragg gratings written in fibers or planar waveguides.

For the measurement of polarization dependent losses a polarization controller was inserted in front of the launching fiber. By probing all input polarizations and taking the difference between maximum and minimum transmission the PDL values were obtained.

Broadband transmission spectra between 1200 and 1650 nm were measured by using a fiber-coupled halogen lamp and an optical spectrum analyzer. As the spectral power density of this source is quite low, only measurements with resolution bandwidths of 10 to 1 nm could be performed.

### **4.4. Mode field**

The measurement of the mode field is done by imaging the near field onto a CCD camera by means of a microscope objective. Depending on the intended magnification a 20× or 40× microscope objective was used. The setup was calibrated by means of a known scale. The CCD camera has a dynamic range of 12 bits and contains 320 × 256 pixels. The camera is attached to a digital framegrabber, which is controlled by a LABVIEW program. Together with the tuneable laser sources mentioned earlier, measurements of the mode fields between 1460 and 1640 nm can be performed.

The captured images were saved as an array of integers, so that they can be evaluated using MATLAB programs. In order to calculate fiber-waveguide coupling losses and form birefringence, two-dimensional gaussian functions

#### 4. Measurement techniques

were fitted onto the measured data. For visualization, the mode fields were plotted as contour or surface plots.

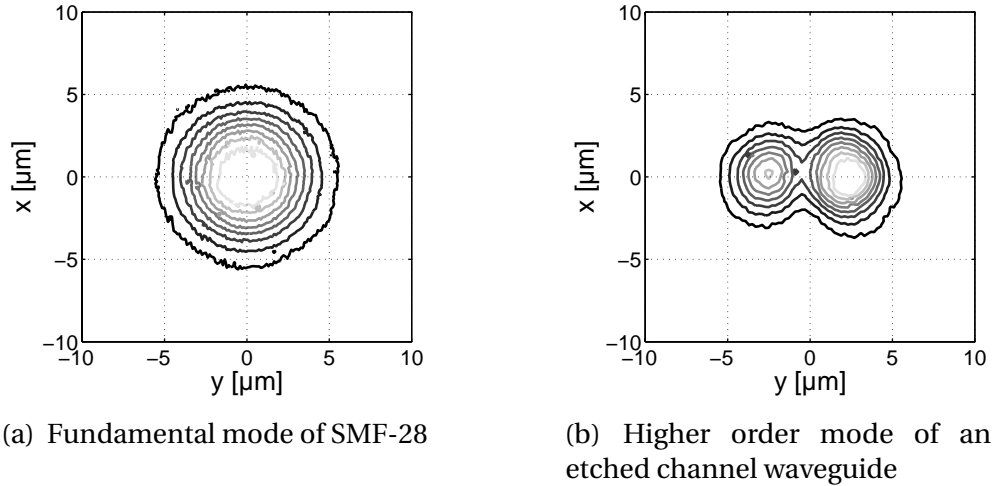


**Figure 4.1.:** Measured mode fields of a single-mode fiber and an etched channel waveguide at 1550 nm. The lines shown are equal power lines at 10...90 % of the maximum intensity.

Two measured mode fields are given in Fig. 4.1 as examples. Fig. 4.1(a) shows the measured mode field of a SMF-28 fiber, with a perfectly circular shape. The spot size obtained was  $5.1 \mu\text{m}$ . This value was later on used for the calculations of fiber-waveguide coupling losses using eq. (2.7). By an off-axis excitation of the waveguide the existence of guided higher order modes can be checked. In Fig. 4.1(b) such a higher order mode of an etched channel waveguide is shown. Such higher order modes are unwanted; they are for instance responsible for additional transmission dips, if Bragg gratings are written in such waveguides.

Calculations of the form birefringence based on the measured mode fields using eq. (2.9) yielded that the form birefringence can be neglected for the waveguides realized within this thesis. Even for the highly elliptical mode field shown in Fig. 5.7(a) the form birefringence is smaller than  $10^{-5}$ . This is well below the measured birefringence values.

## 4.5. UV-induced refractive index changes

For the measurement of UV-induced refractive index changes various methods exist, which differ in the amount of gathered information, applicability to different material compositions and costs. If there is already a waveguide present before UV-irradiation, as it is the case for optical fibers, two widely used methods are the measurement of the Bragg wavelength shift during Bragg grating inscription and the Fabry-Pérot method. A comparison of both methods is given in [62]. These two techniques can also be applied to planar waveguides. There are, however, some experimental issues which make their use for planar waveguides less practical than compared to fibers.

As this thesis deals with the waveguide structuring by UV-induced refractive index changes there are no waveguides (apart from a possible slab waveguide) present before UV-irradiation. Therefore other techniques have to be used in order to quantify the refractive index profiles of the UV-written waveguides.

### 4.5.1. Linnik interferometer

A very well suited measurement setup for the refractive index profile determination of planar waveguide structures is the Linnik interferometer. It is basically a Michelson interferometer inside an optical microscope, see Fig. 4.2. In addition to a simple Michelson interferometer there are two matched high NA microscope objectives in both interferometer arms. This offers a high spatial resolution for the refractive index determination. For evaluation the resulting image is taken with a digital camera and transferred to a computer.

The evaluation of the refractive index from the interference pattern is sketched in Fig. 4.3(a). Because of the tilted reference mirror, using a flat mirror as test object results in a series of interference lines. The number of lines visible on the screen can be controlled by the tilt angle  $\alpha$ . If the flat mirror is replaced with the sample under test, any change in the optical path difference between reference and test arm results in a shift of the local interference pattern. The amount of the shift is proportional to the optical path difference  $\varphi$ :

$$\varphi = \frac{2\pi \cdot 2d \cdot \Delta n}{\lambda} . \quad (4.1)$$

#### 4. Measurement techniques

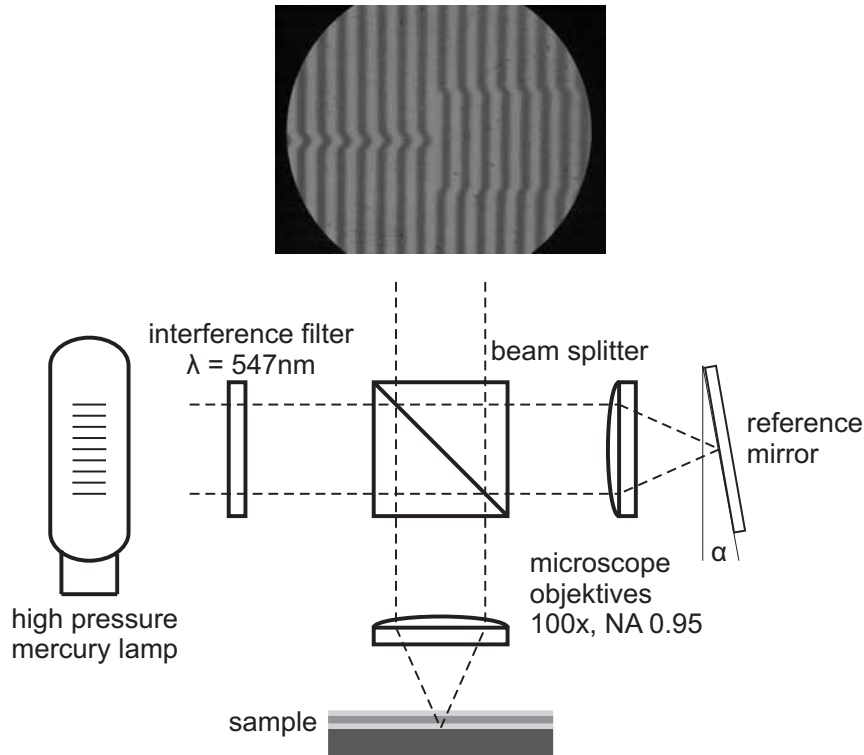


**Figure 4.2.:** Linnik interferometer for the measurement of UV-induced refractive index changes. The picture shown on top is the interference pattern of a center-fed UV-written multi-mode interference coupler.

From this path difference the refractive index change  $\Delta n$  can be calculated:

$$\Delta n = \frac{\varphi \cdot \lambda}{4\pi \cdot d}. \quad (4.2)$$

As an example the transverse refractive index profile of an UV-written multi-mode section is shown in Fig. 4.3(b).

With the setup used a spatial resolution of  $\sim 0.4\mu\text{m}$  and a refractive index resolution of  $\sim 10^{-4}$  were achieved. The great advantage of this method is that it enables the determination of waveguide width and transverse refractive index profiles anywhere on the wafer. In addition, it is a very fast method.

It should be noted that this setup cannot distinguish between changes of the optical path length due to changes of the thickness or due to index changes. This can be a problem when the surface of the materials under test is not flat over the area of inspection or if the UV-irradiation causes a densification/expansion

#### 4.5. UV-induced refractive index changes

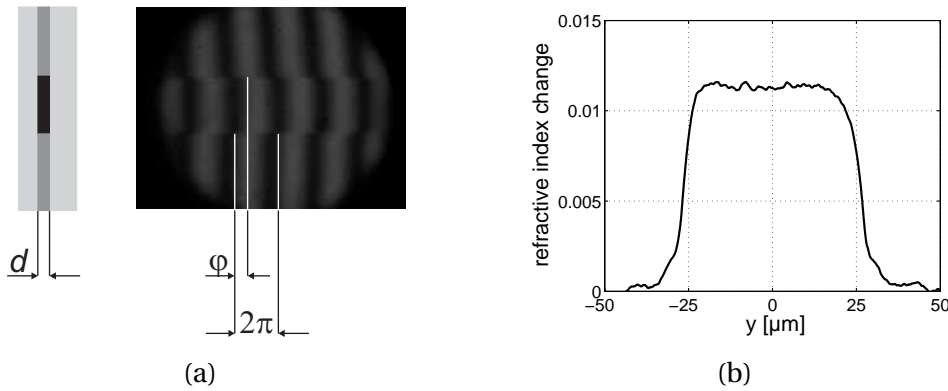


**Figure 4.3.:** Evaluation of the refractive index from the interference pattern and transverse refractive index profile of an UV-written MMI section.

of the material (see section 5.7.3). Another obvious requirement is the need of a reflecting layer as close as possible to the layer under test. All of the waveguides tested with this method had a silicon substrate which is located about  $15\ \mu\text{m}$  beneath the core layer.

#### 4.5.2. Refracted near-field method

The most advanced technique for high-resolution measurement of the refractive index profiles of optical fibers and integrated optical waveguides is the refracted near-field method (RNF) [63, 64]. As the two-dimensional refractive index distribution is obtained with this method, it is possible to see where the index changes occur and also if there is a mixture of positive and negative index changes. In addition it does not require wave guidance, but only a prismatic refractive index distribution along the  $z$ -direction. These points make this method perfectly suited for the characterization of UV-induced refractive index changes obtained within this thesis.

The basic principle of the RNF method is sketched in Fig. 4.4. The sample surface under test is illuminated with a focused beam whose vertex angle greatly exceeds the numerical aperture of any possible waveguide structure inside the sample. By scanning the beam focus over the sample area and also over two areas with known refractive indices  $n_3$  and  $n_6$  (yielding  $P_{\text{ref}, n_3}$  and  $P_{\text{ref}, n_6}$ ) the refractive index distribution  $n_4(x, y)$  can be calculated from the detected power

#### 4. Measurement techniques

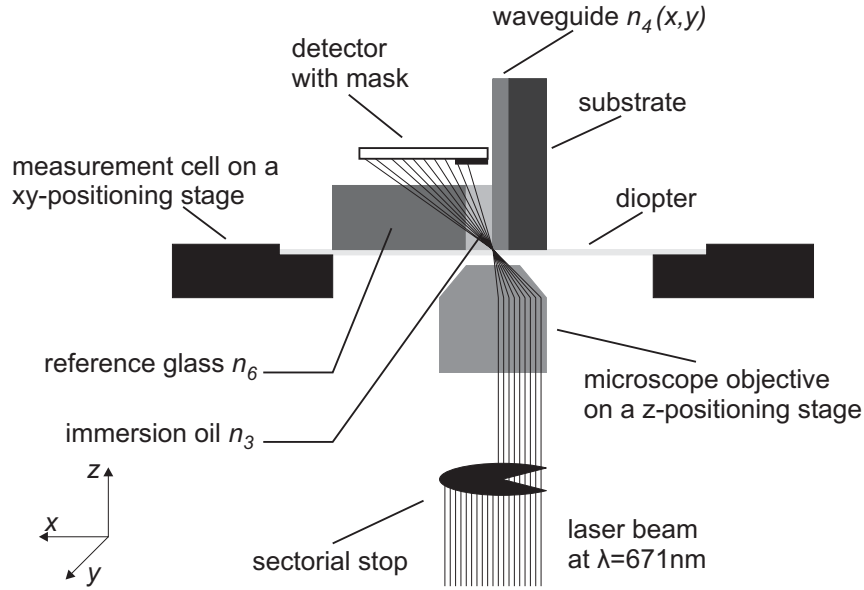


**Figure 4.4.:** Schematic representation of the RNF-setup used [65].

$P_{\text{det}}$  of the refracted light.

$$n_4^2(x, y) = \frac{n_6^2 (P_{\text{ref}, n_3} - P_{\text{det}}) + n_3^2 (P_{\text{det}} - P_{\text{ref}, n_6})}{P_{\text{ref}, n_3} - P_{\text{ref}, n_6}} \quad (4.3)$$

However, due to the opacity of silicon at the used wavelength of 671 nm, the standard refracted near-field technique cannot be directly used for silica-on-silicon integrated optical waveguides and therefore some modifications are needed. The main difference is the sectorial stop shown in Fig. 4.4, which blocks three quarters of the beam. This is done in order to prevent any light from being reflected off the silicon substrate [66].

Care must be taken in preventing air bubbles from being captured between the sample under test, the glass block and the sample holder. To ensure a constant thickness of the oil-layer between the sample under test and the reference glass block,  $25 \times 25 \mu\text{m}^2$  glass fibers were inserted. This is needed because the oil layer is also used as a reference. If the sample under test contains layers with known refractive index (for instance a buffer layer made of thermal oxidized silicon) these layers can be used as references, too. With this setup a spatial resolution of  $\sim 0.5 \mu\text{m}$  and a refractive index resolution of  $\sim 10^{-4}$  were achieved [65].

#### 4.5. UV-induced refractive index changes

In Fig. 4.5 two examples of measured refractive index profiles are shown. The first picture shows an etched channel waveguide in silica on silica. Whereas its profile could also have been obtained with the Linnik interferometer, this would not be the case for the second result shown. The second example shows a 3D representation of two UV-written waveguide structures in non hydrogen-loaded sample A1. Refractive index changes in the core and in the cladding layer can be recognized there.

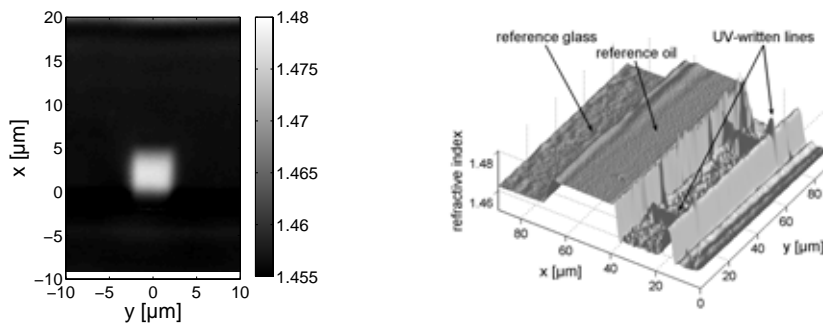


**Figure 4.5.:** Examples for typical RNF measurement: a 2D plot on the left and a 3D plot to the right. Whereas the left figure only shows the region of interest, the right picture also shows the reference glass and immersion oil regions.

One of the major practical problems with the refracted near-field method is the sample preparation. All optical components must undergo careful cleaning and polishing since surface contaminations (i. e. scratches, dirt) lead to intensity variations, which could be falsely interpreted as refractive index variations. This turned out to be a severe problem when dealing with the samples used in section 5.7.

#### 4.5.3. Other techniques

If the UV-induced refractive index change is positive and large enough to allow waveguiding, the following method is often used [67]. It is based on the assumption that the UV-irradiation results in a step index profile for the directly UV-written waveguides. First, waveguides are written with the writing conditions of interest (for instance different combinations of power density and writing velocity). Into these waveguides weak Bragg gratings ( $R \sim 1\%$ ) are inscribed afterwards. As the grating period is known, the effective index of the waveguides can be determined from the measured Bragg wavelength. The width

#### 4. Measurement techniques

of the waveguides can be measured using a high resolution optical microscope. With these information an equivalent step-index profile can be calculated. This method yields only a single value for the index increase and therefore no information about the profile. On the other hand, it is a very simple method and does not require any special equipment.

Further techniques used for the determination of two-dimensional UV-induced refractive index profiles are based on UV-induced blue luminescence [68], refractive index dependent etching rates [69] or measurement of near-field intensity distributions of guided modes [70].

### 4.6. Group delay and chromatic dispersion

In addition to the power transmission and reflection properties of optical devices the phase properties are also of importance for several applications. One example is the chromatic dispersion in transmission and reflection of Bragg gratings used in optical add/drop-multiplexers (see Fig. 6.3). These properties were obtained by wavelength scanning interferometry.

The setup for measuring the complex transmission factor  $t(\nu)$  of a device under test (DUT), i. e. its intensity transmission  $|t(\nu)|^2$  as well as its transmission phase as a function of the optical frequency  $\nu$ , is sketched in Fig. 4.6 [71]. The derivative of the phase with respect to  $\nu$  yields the group delay  $\tau(\nu)$ . For the measurement of the reflection properties of fiber Bragg gratings an optical circulator is added to the setup. In that way the absolute value and the phase of the complex reflection factor are determined and from that the group delay  $\tau_R(\nu)$  in reflection.

The measurement setup consist of two Mach-Zehnder interferometers which are fed by a common tuneable laser source (TLS). One interferometer contains the grating under test in one of its arms (DUT-interferometer) while the second one is an unbalanced auxiliary interferometer with nondispersive arms. Ideally, the instantaneous optical frequency of the TLS should change linearly with time:

$$\nu(t) = \nu_0 + \gamma t . \quad (4.4)$$

In that case, the auxiliary interferometer would not be needed and the desired information on the complex transmission factor  $t(\nu) = |t(\nu)| \cdot \exp\{j\Phi(\nu)\}$  or the complex reflection factor  $r(\nu) = |r(\nu)| \cdot \exp\{j\Phi(\nu)\}$  is contained in the output

#### 4.6. Group delay and chromatic dispersion

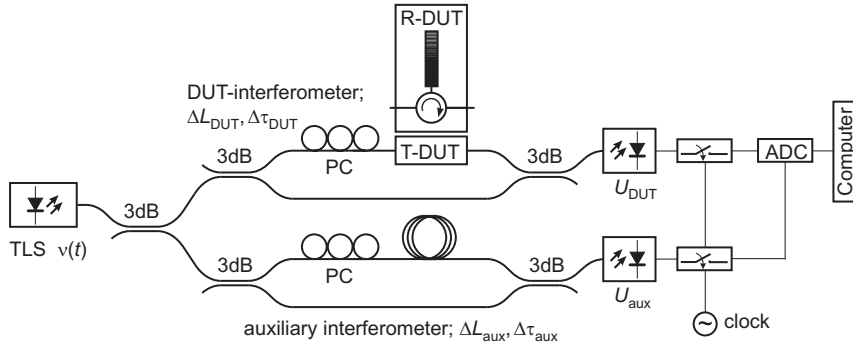


**Figure 4.6.:** Wavelength scanning interferometry for determining the complex transmission and reflection factor of optical components.

detector signal  $U_{DUT}(t)$  of the DUT-interferometer. In the case of a reflecting DUT, the superposition of signal and reference wave yields

$$U_{DUT}(t) \propto |1 + r(\nu)|^2 = 1 + |r(\nu)|^2 + |r(\nu)| \cdot \exp\{-j\Phi(\nu)\} + |r(\nu)| \cdot \exp\{+j\Phi(\nu)\}. \quad (4.5)$$

Fourier transforming  $U_{DUT}(t)$  yields a DC-component and three additional terms: a low frequency term due to the power spectrum  $|r(\nu)|^2$ , and two symmetrically located terms at positive and at negative (electrical) frequencies, respectively. The latter are separated from each other, provided a sufficient fiber delay  $\Delta L_{DUT}$  between measurement and reference arm is used. Eliminating the first and the second term in the Fourier spectrum and subsequently performing an inverse Fourier transform yields the last term of the above equation, namely

$$U_{analyt}(t) = C \cdot |r(\nu)| \exp\{j\Phi(\nu)\}, \quad (4.6)$$

which contains in particular the information on the group delay spectrum

$$\tau(\nu) = (1/2\pi) \cdot d\Phi(\nu) / d\nu. \quad (4.7)$$

Actually, unavoidable deviations from a linear laser sweep during the measurement will cause appreciable errors in the dispersion measurement. Therefore, a nondispersive unbalanced auxiliary interferometer is used in order to correct for the deviations from a linear sweep.

The measurements were performed with a scanning speed of 40 nm/s and a sampling rate of 5 MHz. For the evaluation of the Bragg gratings fabricated in this thesis the scanned wavelength range was mostly chosen in the range of 5 nm,

#### 4. Measurement techniques

resulting in a measurement time of less than 200 ms. After signal processing the group delay data are spectrally averaged. With a spectral resolution of 20 pm a relative error in group delay of about  $10^{-4}$  and an absolute accuracy of about  $\pm 0.25$  ps was achieved, see the measured group delay of a single-mode fiber patchcord in Fig. 4.7(a). The chromatic dispersion is calculated by differentiation of the group delay with respect to the wavelength.

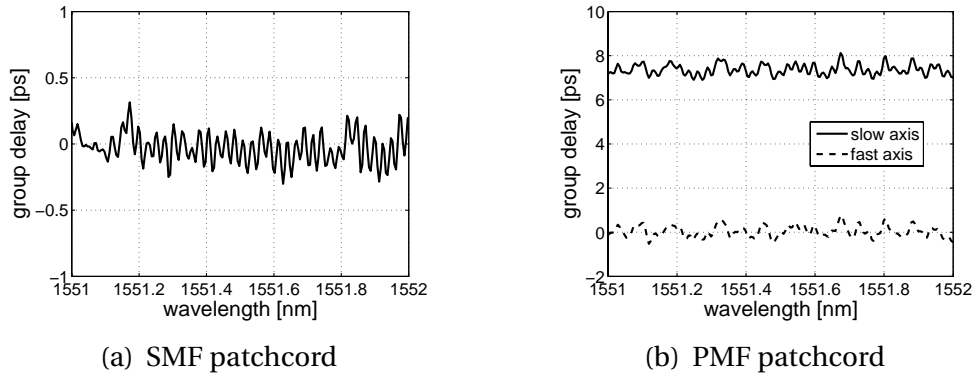


**Figure 4.7.:** Group delay curves of a single-mode fiber patchcord and a polarization maintaining fiber patchcord measured by wavelength scanning interferometry.

The method shown above can also be generalized for the determination of the polarization properties of a device under test. For this purpose a polarization controller is added after the TLS and a polarization diversity receiver is used at the output of the DUT-interferometer. By making two scans with different (preferably orthogonal) polarizations the four complex elements of the Jones matrix are obtained [2]. In Fig. 4.7(b) the group delay curves for the fast and slow axes of a short piece of polarization maintaining fiber are shown.

As the UV-induced birefringence during the Bragg grating inscription is very small, only results for one polarization are presented within this thesis. Examples for a full complex characterization of UV-written Bragg gratings are given in Fig. 6.15 and 6.16.

### 4.7. Spatial reconstruction of Bragg gratings

For the reconstruction of the spatial grating structure the Optical Frequency Domain Reflectometry (OFDR) and inverse scattering were used [72]. The experimental setup is principally the same as shown in Fig. 4.6. In order to

achieve a high spatial resolution a scanned wavelength range of 40 nm was used here.

After the determination of the complex reflection factor the complex impulse response is calculated by Fourier transformation of the complex  $r(\nu)$ -data. This impulse response is the starting point of an inverse scattering solver for the calculation of the complex coupling coefficient  $\kappa(z)$  which represents the spatial variation of grating strength and local grating period [73]. High confidence in these measurements can be derived from the fact that subsequent measurements from either side of a given grating – while yielding completely different raw data – yield amazingly coinciding spatial data along the grating [72]. It should be, however, noted that this reconstruction only works for moderate grating strengths (about 10 dB transmission dip). Examples for reconstructed grating profiles and a comparison with the design are given in Fig. 6.14.

With the knowledge of  $\kappa(z)$  discrepancies between design and fabricated devices can be resolved, see section 6.7 as an example. Also an iterative writing process was made feasible by the interaction of OFDR and inverse scattering [3].

A different approach for the spatial characterization of Bragg gratings is the Optical Space Domain Reflectometry (OSDR). A short introduction of the underlying measurement principle and some obtained results will be given in appendix C.

## 4.8. Conclusion

The transmission spectra of the UV-written waveguide structures were measured by using either tunable laser sources or optical spectrum analyzers. Whereas the first setup allows for measurements with a high dynamic range (90 dB) and wavelength resolution (1 pm), the latter one enables the measurement on a broad wavelength range ( $> 400$  nm).

The near fields of the fabricated waveguide structures were characterized with the help of an IR-CCD camera and a digital framegrabber. This procedure was especially important for the fabrication of directly UV-written multi-mode interference couplers.

UV-induced refractive index changes were measured by a Linnik interferometer and the refracted near-field method. Both methods offer a high spatial ( $\sim 0.5\mu\text{m}$ ) and high refractive index resolution ( $\sim 10^{-4}$ ). The Linnik interferometer enables the determination of waveguide width and transverse refractive

#### *4. Measurement techniques*

index profiles anywhere on the wafer, whereas the refracted near-field method yielded two-dimensional refractive index profiles.

The wavelength scanning interferometry setup used, enabled the determination of the complex reflection or transmission properties of optical devices. Measurements of wavelength dependent group delays were performed at the same time with high accuracy ( $\pm 0.25$  ps), high wavelength resolution (20 pm), in a wide wavelength range (several nm), and in a short measurement time ( $< 1$  s). Moreover these measurements were polarization resolved by extending the receiver to be a polarization diversity receiver and applying two subsequent measurements with different input states of polarization.

A coherent frequency domain reflectometer – closely related to the scanning interferometer – was used to determine the complex reflection factor of waveguide Bragg gratings as a function of wavelength. From this data the complex coupling coefficient along Bragg gratings was evaluated by applying an inverse scattering algorithm. This setup was an important tool in controlling the writing process of the Bragg gratings fabricated within this thesis.

Whenever the necessary experimental setups were not available in-house, facilities at the respective partners' sites were used. This mostly applies for the determination of chemical and physical properties of the material systems used.

## 5. Direct UV-writing of waveguide structures

In this chapter the use of UV-induced refractive index changes for the patterning of optical waveguide structures will be presented. After a short description of the mature photolithography/etching technology, the direct writing technique (DWT) is introduced. Following a description of the writing setup used, the fabrication of single-mode building blocks and multi-mode interference couplers in hydrogen loaded germanium-doped silica samples is presented. This is followed by sections about refractive index changes in germanium-free silica-based samples and waveguide structuring by means of UV-induced refractive index *decreases*. The chapter ends with sections about waveguide structuring in bulk glasses and the use of UV irradiation for the trimming of arrayed waveguide gratings.

### 5.1. Motivation

The two pioneering papers about the photosensitivity of germanium-doped silica by Hill et al. [32] and Meltz et al. [33] were the starting points of a new field in optical science. The refractive index changes achieved, however, were rather small and were only used for the creation of various types of Bragg gratings in optical waveguides. The invention of hydrogen-loading resulted in UV-induced refractive index changes in the order of several  $10^{-3}$  [57]. Such refractive index changes are large enough to form the core of an optical waveguide. In the first experiments, UV-written waveguide structures were fabricated by focussing a UV-laser beam with a cylindrical lens to a thin line [74] or by using an excimer laser and a metal mask [75]. In 1994 the first paper about the direct writing technique using a focused CW UV-laser was published by Svalgaard et al. [34]. This technique offers – when compared to mask and etching techniques – a simple and promising way to produce planar lightwave circuits (PLC).

## 5. Direct UV-writing of waveguide structures

In the following paragraphs the necessary fabrication steps for the realization of integrated optical waveguides by conventional deposition, photolithography and etching technologies will be briefly introduced. A detailed review can be found in [31].

The starting materials are simple silicon wafers, see Fig. 5.1(a). In order to get a sufficient structural support the thickness is mostly chosen between 500 and 1000  $\mu\text{m}$ . The first fabrication step is the creation of the buffer layer. As this layer mostly consists of pure silica, this is usually done by oxidization of the silicon surface (thermal oxidized silicon: TOS) instead of using deposition techniques, like flame hydrolysis deposition (FHD) or plasma-enhanced chemical vapor deposition (PECVD).

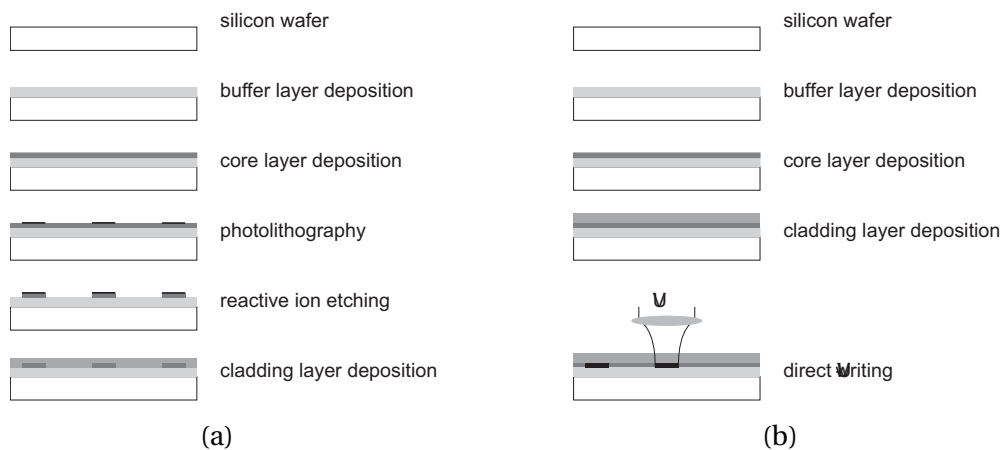


**Figure 5.1.:** Comparison of waveguide structuring by photolithography/etching and direct UV-writing.

The core layer with a raised refractive index is deposited on top of the buffer. The index increase is usually achieved by codoping the silica with germanium, but also other materials like silicon oxynitrides or aluminium oxide can be used as core layers. The waveguide patterning of the core layer is done by traditional photolithography and etching. The final fabrication step is the coverage of the etched waveguides by a cladding layer. Commonly boron phosphorus silica glass (BPSG) is used for this purpose.

The mastering of all single steps of this work flow is a precondition for a reproducible quality of the fabricated devices. Once this is achieved, this production technique is perfectly suited for mass production. It has, however, only limited flexibility. Changes of the waveguide geometries require the production of a new mask and also the following fabrication steps have to be adapted.

## 5.2. UV writing setup

These drawbacks are avoided by the fabrication of integrated optical waveguides by the direct writing technique using a focused UV beam [34]. This technique takes advantage of the fact that the UV-irradiation of germanium-doped silica permanently increases the refractive index. By moving the focused beam over the sample arbitrary waveguide structures can be realized. Changes of the waveguide geometries only require changes in the input file for the translation control program. Therefore, this technique is particularly suitable for the prototyping phase of optical devices, but also a small series production was already proven to be feasible with the DWT [76].

The material systems used for this technique are mostly samples with a photosensitive layer sandwiched between two non-photosensitive layers. Such a layered material system can easily be produced by the deposition techniques mentioned above. If the photolithography and etching steps are omitted the same material system used for the conventional waveguide production can be used. It is, however, advantageous to specially design material compositions for the DWT. Also bulk glasses have been used as material systems. In section 5.8.4 a special writing technique will be presented which enables the creation of buried channel waveguides in bulk glasses.

## 5.2. UV writing setup

A schematic drawing of the setup for fabrication of optical waveguide structures by the direct UV writing technique is shown in Fig. 5.2. The major components are:

1. a continuous wave UV laser
2. a system of optical elements for directing and focussing the laser beam
3. two axis translation system for the patterning of the waveguide structures.

The UV laser is an argon ion laser which produces continuous wave output in the deep UV range by intracavity second harmonic generation using an  $\beta$ -BBO crystal [77]. At the operating wavelength of 244 nm the laser has a maximum output power of 100 mW. The laser beam is linearly polarized in the horizontal plane and has a specified  $1/e^2$  diameter of 0.8 mm.

Using a series of dielectric mirrors the UV light is directed to the writing facility. The shutter positioned right after the laser output is computer controlled and enables the positioning of the translation stages without incident UV power. To

## 5. Direct UV-writing of waveguide structures

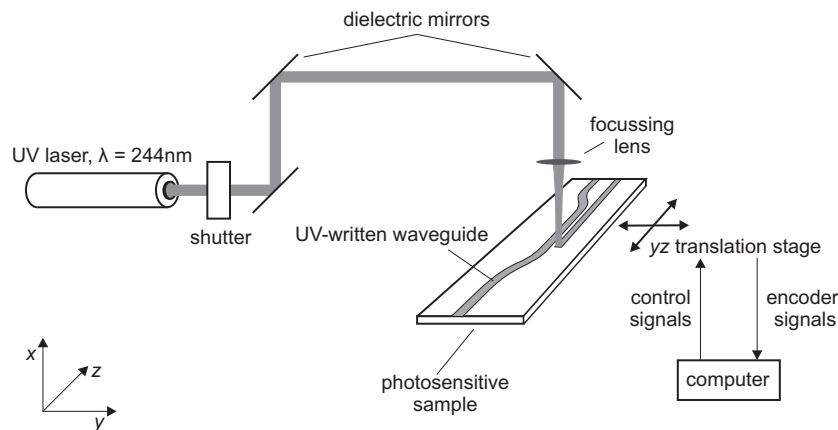


**Figure 5.2.:** Schematic representation of the setup used for direct UV writing of waveguide structures.

focus of the laser beam different lenses were used (10/20 mm best form lenses or  $20\times/40\times$  UV microscope objectives, all made out of fused silica). The position of the lens is controlled by focussing the back reflected light from the sample to infinity.

The two-dimensional translation equipment consists of two high precision translation stages mounted in a yz-setup. Both stages have a travel range of 105 mm and are equipped with internal glass encoders having a resolution of 50 nm [78]. The sample to be written is mounted on top of the two translation stages by means of a vacuum holder.

The two translation stages and the shutter are controlled by a FlexMotion card [79] inside a computer. For the programming of this card the contour mode was used. In this mode the movement of the axes are defined by their position at a given time sampling interval. All structures inside this thesis were written with a sampling interval of 10 ms. The points in between were interpolated by the FlexMotion card using cubic splines. Using the built-in encoders of the translation stages the deviation of the actual from the intended position is recorded with a sampling time of 10 to 20 ms<sup>1</sup>. For all critical parts of the written structures this deviation was below three encoder steps. The whole writing facility is controlled by a LABVIEW program.

<sup>1</sup>sampling interval is not equidistant in time

### 5.3. Material systems used

The structure definition files, which are the input for the LABVIEW program, were created by a collection of MATLAB programs. The definition of simple waveguide structures (straight waveguides, S-bends, etc.) are the basis for more complicated structures, like directional or multi-mode interference couplers. Using this approach new waveguide structures can easily implemented.

An important characteristics for UV-induced refractive index changes is the applied fluence, i. e. the applied power density times time. For the description of Bragg grating writing processes this unit is well suited because the power density is mostly homogeneous over the area of interest. This situation is different for the description of writing processes with a focussed UV-beam, where the power distribution has a gaussian shape. Whenever the term fluence  $F$  is used in this chapter it is defined as follows:

$$F = \frac{P_{UV}}{\pi w^2} \cdot \frac{2w}{v} . \quad (5.1)$$

For this calculation the power distribution is assumed to be equal over the circular area given by the  $1/e^2$ -radius  $w$  of the focus and the irradiation time by the time it takes to move a distance of  $2w$  with the velocity  $v$ .

The term fluence implies that only the product of power density and irradiation time determines the refractive index changes. Whereas this is very often fulfilled for the low power densities used for the fabrication of fiber Bragg gratings, this is no longer true for the high power densities used for the DWT. For several experiments performed within this thesis it was found out that a lower power density could not be compensated for by a longer irradiation time (corresponding to a slower writing velocity).

Most of the samples used were hydrogen-loaded before the UV-irradiation. The hydrogen-loading facility consists of two different chambers for loading fibers and planar waveguide samples separately [80]. Using a compressor the pressure from the hydrogen bottle is increased to 300 bar. The hydrogen-loading was performed at room temperature and the minimum loading time was 10 days.

### 5.3. Material systems used

Three different material samples were used for the experiments presented in the next section and are shown in Fig. 5.3. A detailed description can be found in appendix D. Sample A1 is normally used for the fabrication of integrated

## 5. Direct UV-writing of waveguide structures

optical waveguides as described in Fig. 5.1(a). As the photolithography and etching steps are omitted, it has a slab waveguide with a refractive index step of  $1.5 \times 10^{-2}$ .

cladding: BPSG	cladding: BPSG	cladding: BPSG
core: Ge-silica	core: Ge-B-silica	core: Ge-B-silica
buffer: TOS	buffer: TOS	buffer: TOS
substrate: silicon	substrate: silicon	substrate: silicon

(a) Sample A1                      (b) Sample A2                      (c) Sample I1

**Figure 5.3.:** Material systems used for the direct UV writing of waveguide structures. Samples A1 and A2 were produced by FHD, whereas sample I1 was fabricated by PECVD.

Sample A2 and I1 are specially designed materials systems for the direct writing technique. By means of a additional doping with boron the refractive index of the germanium-doped core layer is matched to the surrounding layers. This has the advantage that there is no slab waveguide present before UV irradiation.

Samples A1 and I1 have proven to be the most suitable for the production of waveguide structures. Due to the lower germanium concentration of the core layer in sample A2 its photosensitivity was lower. Therefore no results obtained with this material system will be shown.

## 5.4. Building blocks

In this section the results obtained for the fabrication of straight waveguides, S-bends and directional couplers will be reported. Through the combination of these building blocks more complicated devices can be realized. All samples were hydrogen-loaded at 300 bar for more than 14 days at room temperature.

### 5.4.1. Straight waveguides

The most important building block for integrated optical devices is the straight waveguide. During the writing of such structures the sample is moved under the

## 5.4. Building blocks

UV beam with a constant velocity. The results obtained for this simple structure are the basis for the design of the more complicated ones.

The waveguiding in these material systems is enabled by a refractive index change inside the core layer. In Fig 5.4 the two-dimensional refractive index distributions after UV-irradiation of samples A1 and I1 are shown. The measurements were performed with the refracted near-field method (RNF). In both material systems a refractive index increase is observed in the UV-irradiated areas. The bright horizontal stripe in Fig. 5.4(a) is the slab waveguide of sample A1, which is already present before UV-irradiation. The UV-induced refractive index increase is smaller than the core cladding difference. As the material system I1 is an index-matched system no waveguide is present before UV-irradiation. A well defined rectangular refractive index profile for the waveguides is achieved.

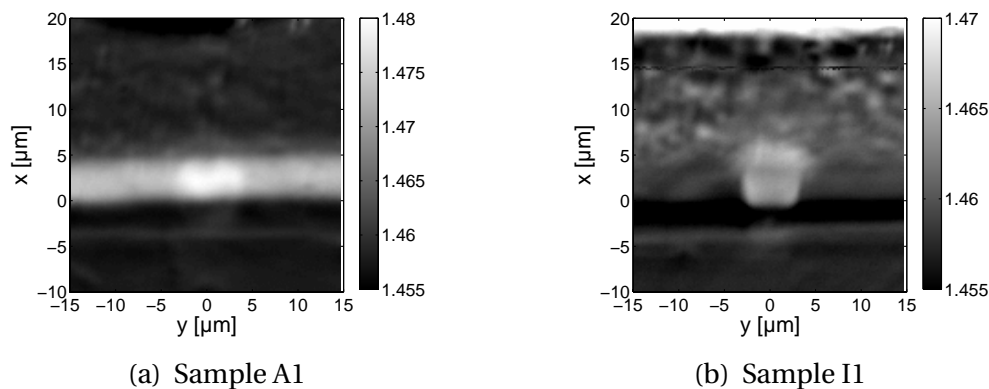


**Figure 5.4.:** Two-dimensional refractive index distributions after UV-irradiation of samples A1 and I1.

The knowledge of the dependence of the UV-induced refractive index changes from the writing conditions (UV-power and writing velocity) is an important pre-requisite for the design of integrated optical waveguide structures. For this purpose straight waveguides were fabricated with different UV-powers (18/35/50 mW) and writing velocities (25...3200  $\mu\text{m/s}$ ). The resulting waveguides were characterized regarding index step and width by means of the Linnik-interferometer. This characterization method was favored to the RNF method, because of the fast measurement time and the possibility of an automated evaluation of the data obtained. The index step was defined as the maximum refractive index increase, whereas the width was defined as full width at half maximum of the refractive index increase.

## 5. Direct UV-writing of waveguide structures

The results for sample A1 are shown in Fig. 5.5. Refractive index changes up to  $6 \times 10^{-3}$  have been achieved for the combination of high UV-power and slow writing velocity. The dependence of the refractive index increase from the writing velocity in a logarithmic scale resembles a straight line. For different writing powers these lines are vertically shifted. Whereas for a writing power of 18 mW refractive index changes could only be measured up to a writing velocity of  $400 \mu\text{m/s}$ , this was possible up to  $1600 \mu\text{m/s}$  for the 50 mW case. The reason that the 35 and 50 mW curves are not further separated can be explained by a reduction of the photosensitivity caused by an outdiffusion of the hydrogen.

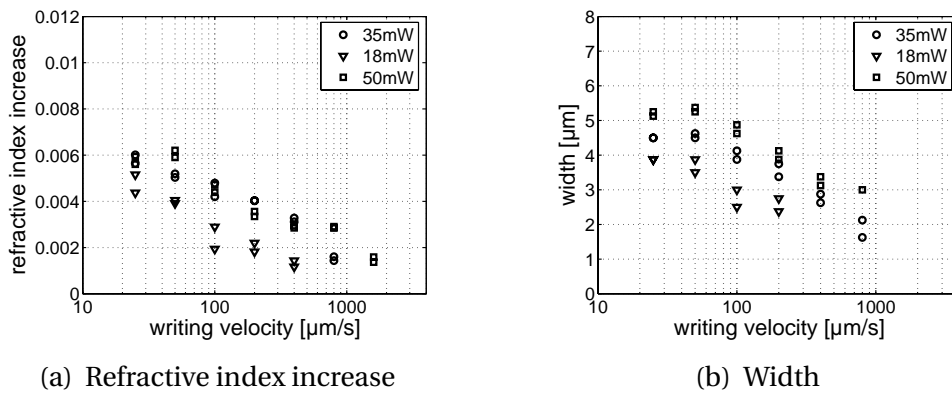


**Figure 5.5.:** Index step and width of UV-written waveguides in sample A1.

For the width of the UV-written waveguides a similar behavior was observed. The widest waveguides were obtained for slow writing velocities. In these fluence regimes the resulting waveguides are broader than the used UV-beam, whereas for the fast writing velocities the opposite is true. For the missing data points at fast writing velocities no meaningful widths could be determined.

In Fig. 5.6 the results for sample I1 are shown. From a qualitative point of view the results are quite similar. The UV-induced index changes however are significantly higher in this material system. Refractive index changes in excess of  $10 \times 10^{-3}$  have been achieved and even for writing velocities up to  $3200 \mu\text{m/s}$  waveguides could be fabricated. The width of the resulting waveguides is slightly higher compared to their counterparts in material system A1.

The main aim for the realization of straight waveguides is the achievement of low insertion losses. The insertion loss consists of two contributions: the fiber-waveguide coupling losses due to the mode mismatch and the propagation losses due to absorption, leakage or scattering.

## 5.4. Building blocks

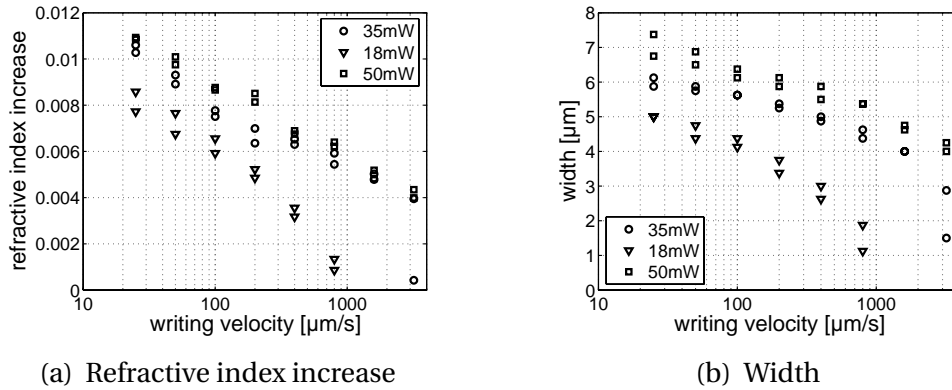


**Figure 5.6.:** Index step and width of UV-written waveguides in sample I1.

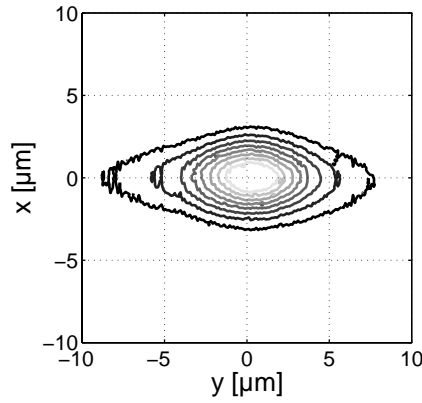
A comparison of measured mode fields of UV-written waveguides in samples A1 and I1 is shown in Fig. 5.7. The waveguides shown in the left column were fabricated with a low fluence, whereas a high fluence was applied for the waveguides in the right column. As it was shown above, a higher writing fluence results in higher refractive index changes and thus in a better confinement of the fundamental mode.

The ellipticity of the mode fields for sample A1 (upper row) is caused by the different refractive index differences in the vertical and horizontal directions, see Fig. 5.4(a). For large UV-induced refractive index changes (Fig. 5.7(b)) this ellipticity is reduced. This unwanted shape can be eliminated by using a material system where the refractive index of the core layer is matched to the values of the buffer and cladding layer, see Fig. 5.4(b). Mode fields of UV-written waveguides in such an index-matched material system I1 are shown in the lower row of Fig. 5.7.

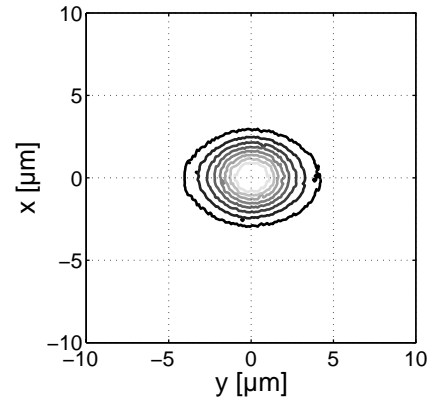
The mode field of a SMF-28 fiber with  $w_x = w_y = 5.1 \mu\text{m}$  is shown in Fig. 4.1(a). As the vertical extensions of the mode fields of UV-written waveguides in sample A1 are much smaller, this results in large fiber-waveguide coupling losses ( $\sim 1$  dB per transition). For sample I1 these losses are significantly lower ( $< 0.1$  dB per transition).

The measured insertion losses of 17 mm long UV-written waveguides in sample I1 are shown in Fig. 5.8(a). By subtracting the fiber-waveguide coupling losses from the values shown, the propagation losses are obtained. Values of 0.3 dB/cm and below have been achieved at 1550 nm. The broadband transmission spectra of waveguides written with three different writing velocities are

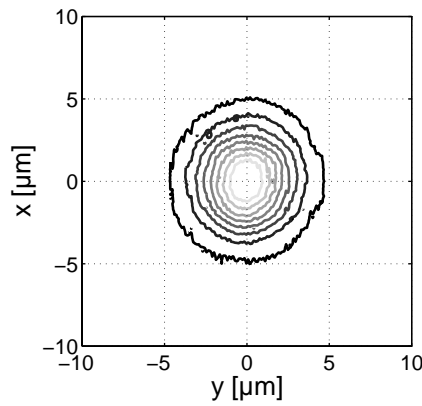
## 5. Direct UV-writing of waveguide structures



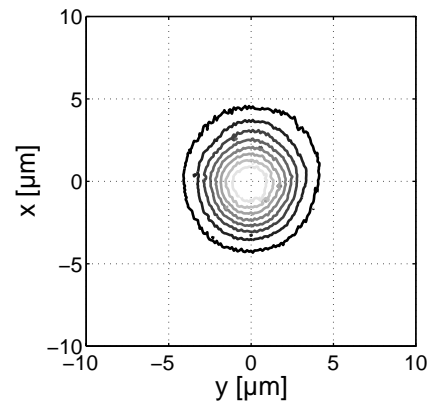
(a) Sample A1, low fluence regime  
( $w_y = 6.9\mu\text{m}$ ,  $w_x = 2.9\mu\text{m}$ )



(b) Sample A1, high fluence regime  
( $w_y = 3.8\mu\text{m}$ ,  $w_x = 2.8\mu\text{m}$ )



(c) Sample I1, low fluence regime  
( $w_y = 4.4\mu\text{m}$ ,  $w_x = 4.5\mu\text{m}$ )



(d) Sample I1, high fluence regime  
( $w_y = 3.8\mu\text{m}$ ,  $w_x = 3.9\mu\text{m}$ )

**Figure 5.7.:** Comparison of mode fields of UV-written waveguides with low and high-fluence in samples A1 and I1. The  $w_x$  and  $w_y$  values are fittings to a two-dimensional gaussian function and the lines shown are equal power lines at 10...90 % of the maximum intensity.

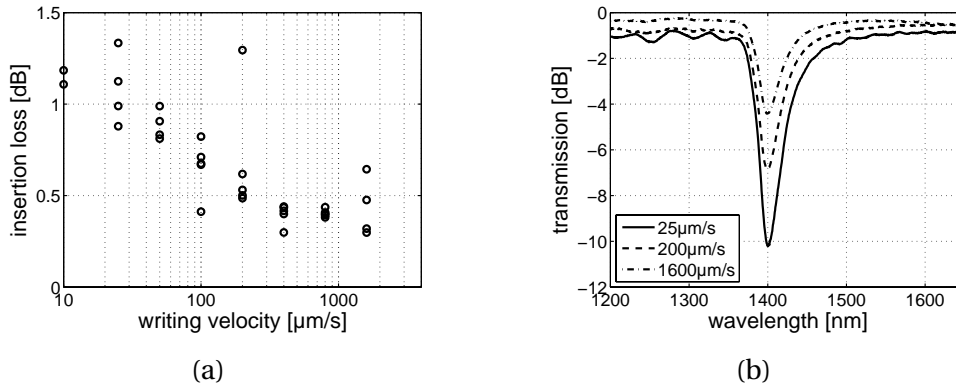


**Figure 5.8.:** Insertion loss values at 1550 nm and broadband transmission spectra of UV-written straight waveguides in hydrogen-loaded samples I1.

given in Fig. 5.8(b). The most prominent feature are the large losses around  $\lambda = 1400$  nm. These losses are caused by absorption due to OH-species, which are created by the UV-irradiation. By substituting the hydrogen with deuterium this absorption peak is shifted from 1.4 to 1.9  $\mu\text{m}$ . This enables the use of UV-written waveguides in the O-, E- and S-band, too. Unfortunately deuterium is more expensive by a factor of 100.

The comparison of the measured losses of waveguides written in samples A1 and I1 yielded higher insertion losses for sample A1. This is mostly due to the large fiber-waveguide coupling losses mentioned before, but also the propagation losses were higher ( $\sim 0.5$  dB/cm). In both material systems the absorption losses at 1400 nm were proportional to the UV-induced refractive index changes. For a refractive index change of  $4 \times 10^{-3}$  the absorption was  $\sim 3$  dB/cm for sample I1, but only  $\sim 0.5$  dB/cm for sample A1.

The polarization dependent losses (PDL) were obtained by varying the input polarization and taking the difference between maximum and minimum transmission. For all waveguides the PDL values were below 0.2 dB

It should be noted that the writing sessions sometimes lasted for more than 6 hours. As there was no cooling of the samples applied during the writing session, there was already a significant amount of hydrogen outdiffusion. This resulted in lower refractive index changes towards the end of the writing sessions, but not in severe degradations of the insertion or polarization dependent losses as observed in [81]. In that publication deuterium-loaded samples I1 were used and no satisfying results could be achieved already after 1 hour of outdiffusion.

## 5. Direct UV-writing of waveguide structures

This hydrogen outdiffusion is less detrimental for material system A1, as the cladding layer is thicker compared to I1, see appendix D.

### 5.4.2. S-bends

For a variety of integrated-optical waveguide structures curved waveguides are necessary. The most notable application are S-bends, which introduce a transversal displacement  $D$  over a length  $L_B$ , see the inset in Fig. 5.9(a). The technological aim for a given displacement is to minimize the necessary length while keeping the excess loss below a certain limit. The excess loss is defined as the increase of the insertion loss compared with a straight waveguide.

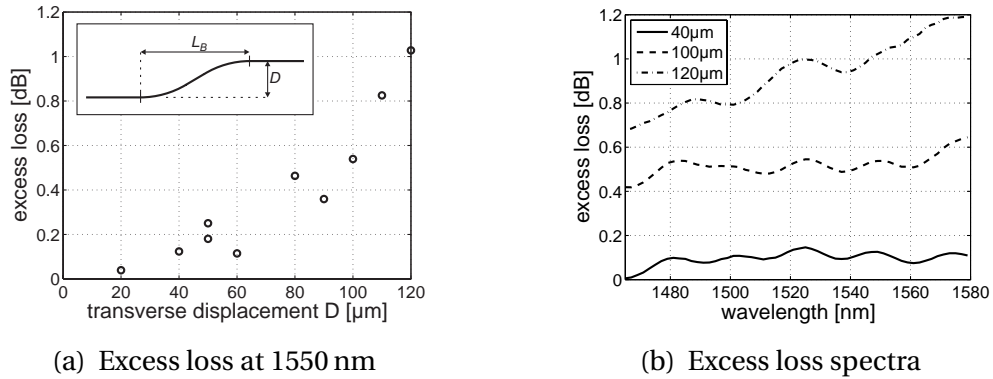


**Figure 5.9.:** Layout and excess losses of UV-written S-bends in material system I1.

The simplest realization of such an S-bend is based on the concatenation of two circular arcs with opposite curvatures  $1/R$ . This layout however has the disadvantage that there are three transitions where abrupt changes of the curvature take place. The largest contribution comes from the middle of the S-bend, where the sign of the curvature changes. This can be avoided by the use of S-bends with a cosine shape. Here the curvature changes continuously between  $\pm 1/R_{\min}$ , with  $R_{\min} = 2L_B^2/D\pi^2$ . All S-bends within this thesis were realized with this shape.

In order to keep the excess losses in comparison to straight waveguides small it was necessary to write the curved sections with a higher writing fluence, i. e. slower writing velocity. The straight waveguide sections were written with a velocity of  $200 \mu\text{m/s}$  whereas the velocity was reduced down to  $100 \mu\text{m/s}$  inside the curved sections. The length  $L_B$  of the S-bends was fixed to 2 mm and the

transverse displacement  $D$  was varied between 20 and 120  $\mu\text{m}$ . Six S-bends were cascaded in order to measure the excess loss with higher accuracy.

In Fig. 5.9(a) the excess losses of the six cascaded S-bends at the wavelength of 1550 nm are shown. For values of  $D$  lower than 100  $\mu\text{m}$  the excess losses per S-bend were smaller than 0.1 dB. As expected the excess losses are wavelength dependent, see Fig. 5.9(b). For the strongest S-bend the excess loss increased from 0.7 dB at 1460 nm to 1.2 dB at 1580 nm.

### 5.4.3. Directional couplers

For several optical applications it is necessary to split the incoming optical power into several output arms, see for instance the add/drop-multiplexer in Fig. 6.2(b). A possible realization for these power splitting components are directional couplers as shown in Fig. 5.10. Two straight waveguide sections are sufficiently closely spaced so that energy is transferred from one to the other. The theory behind this power exchange is explained in section 2.2.1.

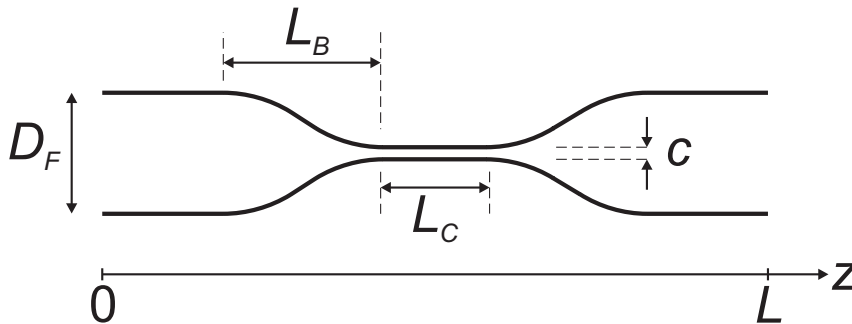


**Figure 5.10.:** Schematic layout of a four port directional coupler.

Through the combination of straight waveguides and S-bends it is possible to fabricate such a device by the direct writing technique. The starting and end components are straight waveguides with a distance  $D_F$  between them. By using S-bends of length  $L_B$  this distance is constantly decreased down to a center-center separation  $c$ . The central coupling region  $L_C$  consist of straight waveguides, too.

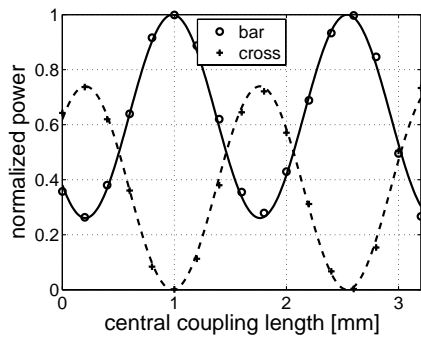
The power in the cross and bar arm at the end of the directional coupler can be calculated by using eq. (2.13), when  $z$  is replaced by  $L_C$ . As it can be seen in Fig. 5.11(a), there is already a significant amount of power in the cross arm, when no central coupling region is present. This is explained by coupling in the

## 5. Direct UV-writing of waveguide structures

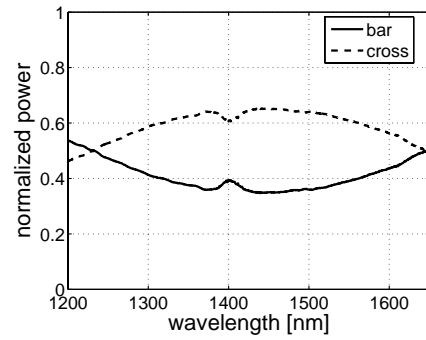
curved waveguides on both sides of the central coupling region. This effect is taken into account by adding a length  $L_{bb}$  to the central coupling length.

$$P_{\text{cross}}(L) = P_0 \frac{\kappa_C^2}{\kappa_C^2 + \delta^2} \sin^2 \left( \sqrt{\kappa_C^2 + \delta^2} (L_C + L_{bb}) \right) \quad (5.2)$$

$$P_{\text{bar}}(L) = P_0 - P_{\text{cross}}(L)$$



(a) Normalized power in bar and cross arm vs. length of the central coupling region



(b) Broadband spectra of normalized power in bar and cross arm for  $L_C = 400 \mu\text{m}$

**Figure 5.11.:** Measured characteristics of UV-written directional couplers in material system I1. The solid and dashed line in the left picture are fittings to eq. (5.2). The shape of both the bar and cross curve at 1400 nm in the right picture is caused by the large absorption at that wavelength region, which made the normalization difficult.

No full power transfer into the cross arm could be achieved, because of the asymmetry of the waveguides inside the coupling region. This asymmetry is caused by the effect that during the writing of the first waveguide there is already some consumption of hydrogen in the region later used for the second waveguide, thus resulting in a lower photosensitivity. This effect can be counteracted by writing the second waveguide with a lower writing velocity [82]. On the other hand it is also possible to intentionally use this asymmetry in order to realize broadband couplers, see Fig. 5.11(b). In contrast to the photolithography and etching technology, where only the waveguide width can be used for the creation of the asymmetry, both the width and the effective index can be varied by the DWT [83].

## 5.5. Multi-mode interference couplers

As shown in the previous section, several single-mode waveguide structures have been made by using the DWT. Up to now the DWT has never been used to realize planar multi-mode devices like, for instance, multi-mode interference (MMI) couplers. That might be due to the stringent requirements concerning properties like refractive-index uniformity. In this section it will be shown that such requirements can be satisfied for MMI devices and that the attractiveness of the DWT can be transferred to these devices [4].

### 5.5.1. Motivation

Multi-mode interference (MMI) couplers [84, 85] are promising devices for power splitting and routing in optical communication systems because of their flattened wavelength response, weak polarization sensitivity, and their moderate fabrication tolerance requirements [86]. Their basic layout consist of one or several input waveguides, two or more output waveguides and a multi-mode section in between. The dimensions for the multi-mode section depend on the material system used and typical values are a width  $W$  of 20 to 100  $\mu\text{m}$  and a length  $L$  of 0.5 to 3 mm. In Fig. 5.12 the layouts of a  $2 \times 2$  and a  $1 \times 3$  MMI coupler are sketched.

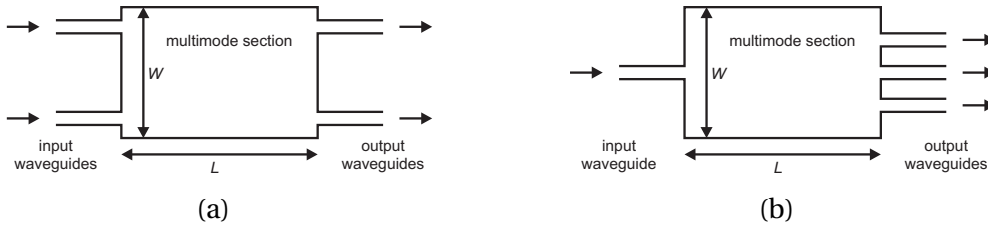


**Figure 5.12.:** Basic layouts of a  $2 \times 2$  and a  $1 \times 3$  MMI coupler.

The operation of a MMI coupler is based on a special progressive decrease of the propagation constants of the modes inside the multi-mode section with the mode number  $m = 0, \dots, m_{\max}$  according to [84–86]

$$\beta_m = kn_1 - \frac{(m+1)^2 \pi^2}{2kn_1 W^2}, \quad (5.3)$$

where  $n_1$  is the effective index of the MMI slab mode,  $W$  is the width of the core,

## 5. Direct UV-writing of waveguide structures

$k = 2\pi/\lambda$ , and  $\lambda$  is the operation wavelength. If the MMI coupler is center-fed at the input, i. e. it is excited by a single waveguide on the symmetry axis of the MMI coupler (see Fig. 5.12(b)), then the interference pattern of the many modes produce  $N$ -fold images of the input field at lengths

$$L_N = \frac{n_1 W^2}{\lambda N}. \quad (5.4)$$

Fig. 5.13 illustrates the 4-fold, 3-fold and 2-fold images of a MMI coupler obtained from simulations using a Beam Propagation Method (BPM) program [87].  $1 \times N$  splitters can be fabricated by choosing the length of the MMI section according to eq. (5.4) and arranging  $N$  output waveguides at the positions of the  $N$  images.

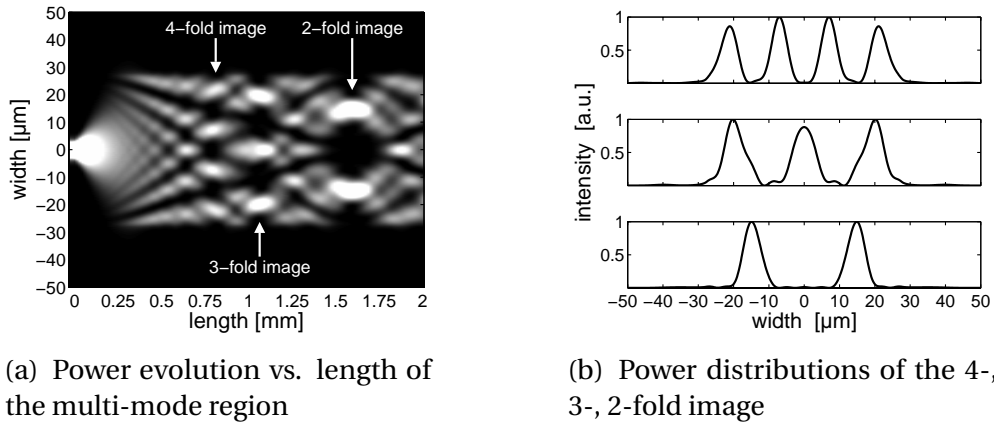


**Figure 5.13.:** BPM simulation of a center-fed MMI coupler with a width of  $55 \mu\text{m}$  and an index difference of  $10 \times 10^{-3}$  at the wavelength of  $1580 \text{ nm}$ .

Condition (5.3) is well fulfilled by well-confined modes of a MMI coupler with a rectangular index profile, when the second term is much smaller than the first term, as it is true for low-index-contrast MMI couplers or for the lowest-order modes of sufficiently wide high-index-contrast MMI couplers. Contrary to a wide-spread opinion [85, 88] it is easy to show that for equal numbers of modes the phase errors due to the non-zero cladding penetration depth of the modes is exactly the same for low- and high-index-contrast MMI couplers. The error introduced by the violation of the necessary paraxial approximation is even smaller for low-index-contrast MMI couplers due to the smaller index difference [89].

## 5.5. Multi-mode interference couplers

This insight encouraged us to try to fabricate MMI couplers by direct UV writing. Possible problems to be envisaged with the UV-writing technology were the realization of sharp index interfaces, profile inhomogeneity due to hydrogen out-diffusion, and refractive index ripples due to the scanning writing process. The results achieved confirm that these problems are not detrimental.

### 5.5.2. Experimental setup

The MMI couplers were fabricated using the DWT setup shown in Fig. 5.2. A UV power of 35 mW was used and the beam was focussed onto the photosensitive core layer by a 20 $\times$  UV-microscope objective to a  $1/e^2$ -diameter of about 4  $\mu\text{m}$ . During the writing process the translation stage was moved with a velocity of 200  $\mu\text{m/s}$ .

The wafer used was a three-layer slab waveguide system on top of a silicon substrate, see sample A1 in Fig. 5.3(a). The buffer layer is made of thermal oxidized silicon and the cladding layer consists of boron phosphorus doped silica. Due to the germanium-doping the refractive index of the core layer is higher by  $1.5 \times 10^{-2}$ . Prior to the UV writing the samples were hydrogen loaded at 300 bar for more than 14 days at room temperature.

The input waveguide of the MMI coupler (Fig. 5.12(b)) was written in a single scan along the  $z$ -direction. For the patterning of the wide multi-mode region a number of line scans were performed with adjacent lines being offset by 1  $\mu\text{m}$ , i. e. about 25 % of the width of the writing spot. Several schemes were tested and are shown in Fig. 5.14: transverse  $y$ -scans written in a narrow meander line, longitudinal  $z$ -scans written in a similar way and longitudinal  $z$ -scans written performed in a cyclic way from the outer to the inner region or vice versa.

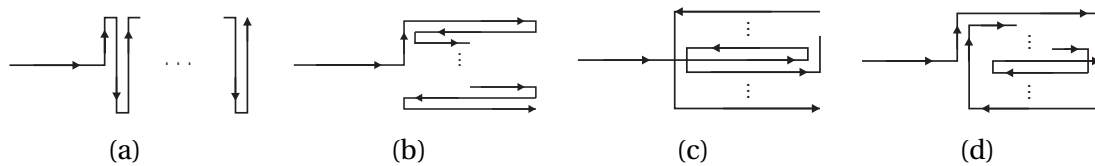


**Figure 5.14.:** Tested writing schemes for the patterning of the wide multi-mode section of a MMI coupler.

The scheme sketched in Fig. 5.14(c) turned out to be the most suitable one and all the results below refer to this technique. After the writing process the

## 5. Direct UV-writing of waveguide structures

samples were annealed for about 24 h at a temperature of 80 °C for out-diffusion of the remaining hydrogen and stabilizing of the UV-induced refractive index changes. The resulting lateral index distributions were measured afterwards by using an interference microscopic method specifically developed for the present purpose (section 4.5.1). The typical UV-induced refractive index increase in the MMI region was found to be  $10^{-2}$ .

### 5.5.3. Results

With the data given in the caption of Fig. 5.13 MMI couplers suitable for 2-, 3- and 4-fold imaging were designed by BPM calculations. The necessary lengths  $L_N$  were 1600, 1050, 800  $\mu\text{m}$  (Fig. 5.13). As an intentional deviation from the design, the length of the 1 $\times$ 3-MMI coupler was chosen to be 1000  $\mu\text{m}$ . The experimentally obtained intensity distributions at the rear end of the MMI section are shown in Fig. 5.15(a). High-quality multiple images were obtained and directly visualized by an IR-CCD camera. In Fig. 5.15(b) a horizontal cut through the images is shown in order to compare the measured power distributions with the BPM simulations (Fig. 5.15(c)).

The power imbalance of the output images (determined by the calculation of field-overlap integrals with the measured field distribution of a straight reference waveguide identical to the input waveguide) were found to be 0.29 dB, 0.08 dB, and 1.1 dB, respectively, for the 2-, 3-, 4-fold images at the design wavelength of 1580 nm. This imbalance remains low, namely below 0.76 dB, 0.55 dB, 1.4 dB within a tuning range of 120 nm according to the broadband response typical for MMI couplers [85, 86].

Another indication of well-controlled behavior is the fact that the useful wavelength range of the 1  $\times$  3 MMI coupler (with  $L = 1000\mu\text{m}$  instead of 1050  $\mu\text{m}$ ) is shifted towards longer wavelengths while an additional version with  $L = 1200\mu\text{m}$  shows the opposite behavior as predicted by eq. (5.4).

After these encouraging results it was also tried to realize complete 1  $\times$   $N$  splitters, which means MMI couplers with attached output waveguides as sketched in Fig. 5.12(b). The obtained results however were not as good as it could be expected from the presented results. A possible explanation is that even small changes in the width of the multi-mode section influence the absolute horizontal position of the images and the coupling to the output waveguide is disturbed.

## 5.6. UV-induced refractive index changes in germanium-free materials

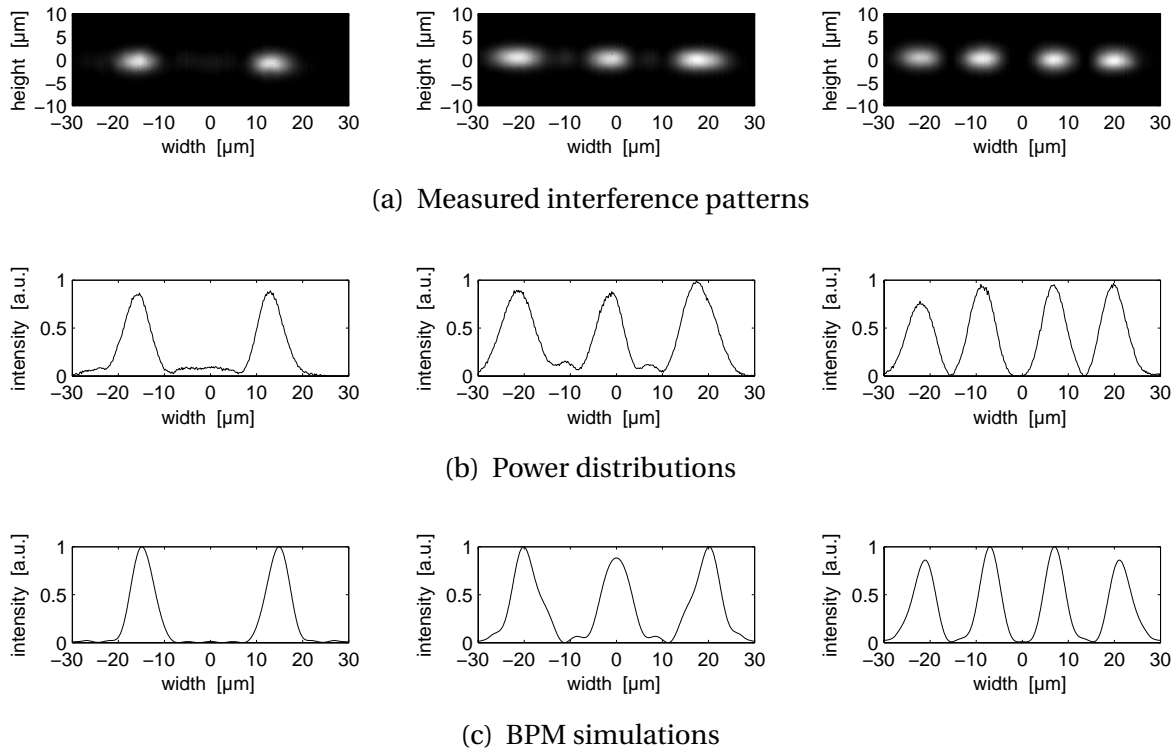


**Figure 5.15.:** Measured interference patterns, power distributions and BPM simulations at the endface of the 2-, 3-, 4-fold image at a wavelength of 1580 nm.

## 5.6. UV-induced refractive index changes in germanium-free materials

The work presented in this section was performed in cooperation with the Institute for Physical High Technology (IPHT) Jena within the framework of the PLATON project. The aim was to investigate the photosensitivity of different optical layers deposited by Flame Hydrolysis Deposition (FHD). During this investigation the main focus was shifted towards germanium-free boron-phosphorus-doped silica layers. Results of this cooperation are published in [5] and [6].

### 5.6.1. Material preparation and UV-writing

The samples used in the following experiments are shown in Fig. 5.16 and consist of a system of different layers. On top of a silicon wafer a 15 μm buffer

## 5. Direct UV-writing of waveguide structures

layer is produced by thermal wet oxidation (TOS) followed by the layers under investigation made by FHD [90]. FHD is a commonly used method to produce high purity SiO<sub>2</sub>-films for optical applications by hydrolysis of Si-halogenides and halogenides of the dopants germanium (Ge), boron (B) and phosphorus (P). Layers with a thickness between 3 and 40 μm can be made depending on the wanted purpose.

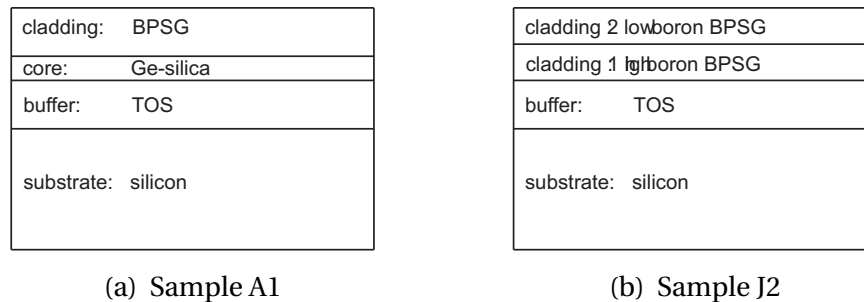


**Figure 5.16.:** Schematic layout of the samples used. All shown layers on top of the thermally oxidized silicon layer are deposited by FHD.

The first layer system is shown in Fig. 5.16(a) and consists of a germanium doped core layer and a cladding layer made of boron phosphorus silica glass (BPSG). This material system is normally used for the production of planar lightwave circuits by photolithography and etching technology (see Fig. 5.1(a)). The second, shown in Fig. 5.16(b), is a specially prepared Ge-free silica layer system consisting of two layers with a different B-doping level. High doping means a doping level of about 15 mol% , low doping of about 5 mol% boron analyzed by electron microprobe analysis.

Photosensitivity experiments were carried out with the setup shown in Fig. 5.2. The UV-laser was operated at power levels of 70/50/30 mW. By using a 10 mm lens the UV-laser beam was focussed onto the core layer with a  $1/e^2$  focal diameter of about 4 μm. Two computer controlled translation stages (operating in a yz-setup) enabled the writing of waveguides with different velocities. Depending on the sample used, writing velocities between 1 and 4000 μm/s were used.

### 5.6.2. Results

It was shown in the previous sections that hydrogen-loading increases the photosensitivity of germanium doped silica layers. Refractive index changes in the

## 5.6. UV-induced refractive index changes in germanium-free materials

range of  $10 \dots 15 \times 10^{-3}$  can easily be obtained in such materials with moderate writing fluences. Fig. 5.17(a) shows a microscope picture of the endface of such a sample. The formation of waveguide inside the core layer can be seen there. No changes inside the cladding layer were observed in such pictures or by refractive index measurements.

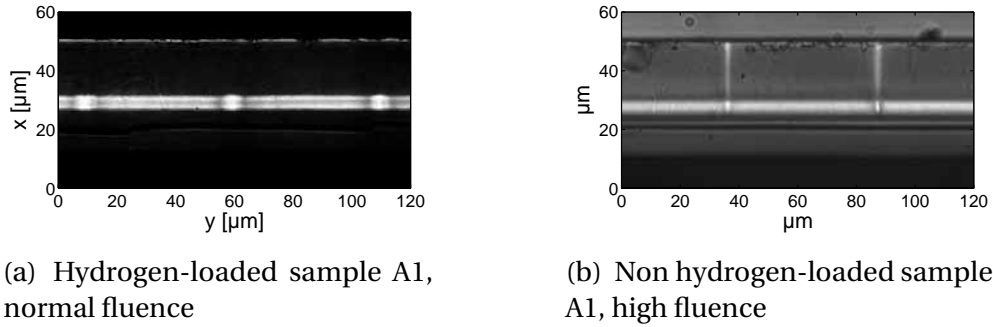


**Figure 5.17.:** Microscope pictures of UV-written waveguides in sample A1 with and without hydrogen loading.

If non hydrogen-loaded samples were used, the resulting behavior was different. As it can be seen in Fig. 5.17(b), changes inside the core and the cladding layer are caused by the UV-irradiation.

The two-dimensional refractive index distribution of two UV-written waveguides is shown in Fig. 5.18(a). First, it reveals a UV-induced refractive index increase in the germanium-doped core layer. Such an increase had been anticipated, though to a lower extent. Secondly, however, there also is an appreciable index increase in the cladding layer. Two vertical cuts are shown in Fig. 5.18(b) for comparison of the pristine and UV-irradiated sections. The index changes in core and cladding layer are of the same order and there is no decrease of the index change along the depth of the cladding layer.

In Fig. 5.19(a),(b) the measured refractive index changes inside the core and cladding layer are shown for varying writing powers and velocities. In both layers the refractive index changes are increasing with increasing writing power and decreasing writing velocity. The maximum obtained refractive index changes are about  $7 \times 10^{-3}$  in the core and  $9 \times 10^{-3}$  in the cladding, respectively.

Such high index changes in germanium-free materials have not been reported before. In [91] UV-written waveguides were fabricated in boron phosphorus doped silica layers deposited by PECVD. Refractive index changes up to  $6 \times 10^{-3}$  were deduced from measured near-field intensity distribution of the guided

## 5. Direct UV-writing of waveguide structures

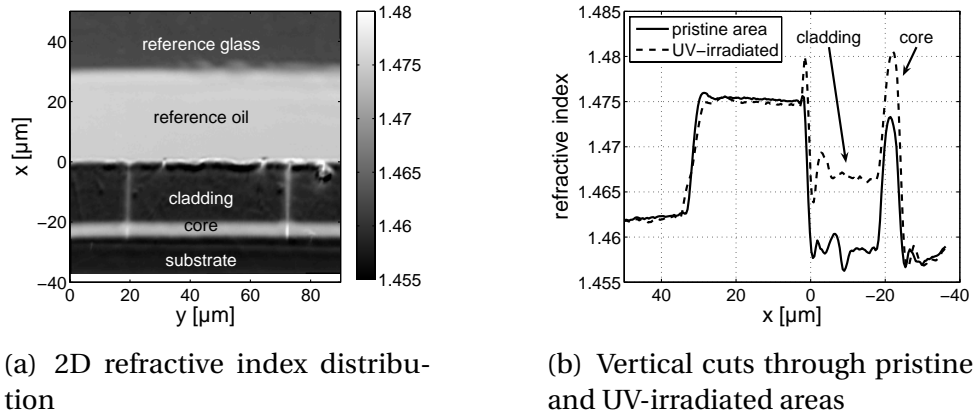


**Figure 5.18.:** Refracted near-field measurements of UV-written areas in non hydrogen-loaded samples A1.

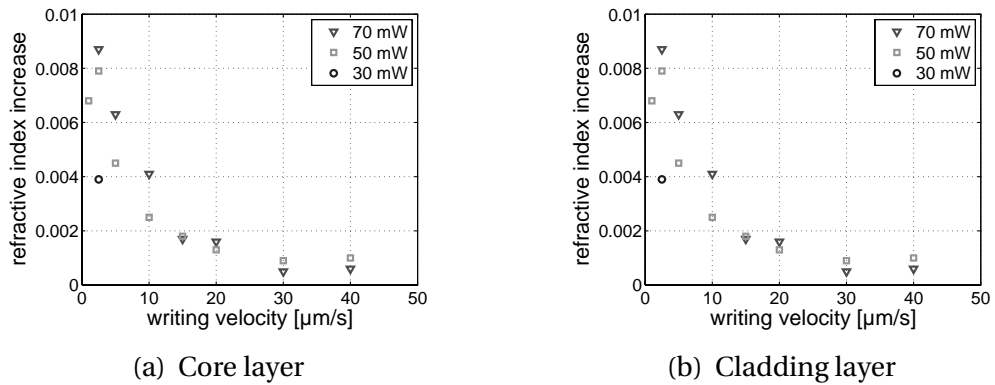


**Figure 5.19.:** Exposure characteristics of UV-induced refractive index changes in the core (germanium-doped) and cladding (BPSG) layer in non hydrogen-loaded A1 samples.

## 5.6. UV-induced refractive index changes in germanium-free materials

mode. However, hydrogen-loading was applied in order to enhance the photosensitivity. In addition an excimer laser at 193 nm was used and the accumulated fluence was not stated. Therefore the results can not be compared. Without hydrogen-loading UV-written waveguides were produced in Pyrex (a bulk borosilicate glass without germanium) [92]. A 244 nm CW laser was used there and refractive index changes in the order of  $10^{-3}$  were obtained by fitting refractive index profiles to measured effective indices of guided modes.

The observation of waveguides in the microscope pictures was reinforced by the measurement of the near-field intensity distributions at 1550 nm of the resulting waveguides. Depending on the vertical position of the input fiber and the tested wavelength, different intensity distributions were obtained, see Fig. 5.20. It seems that there are at least three modes, which can propagate in this structure. By using a simplified model for the refractive index distribution this assumption could be verified using a numerical mode solver<sup>2</sup>.

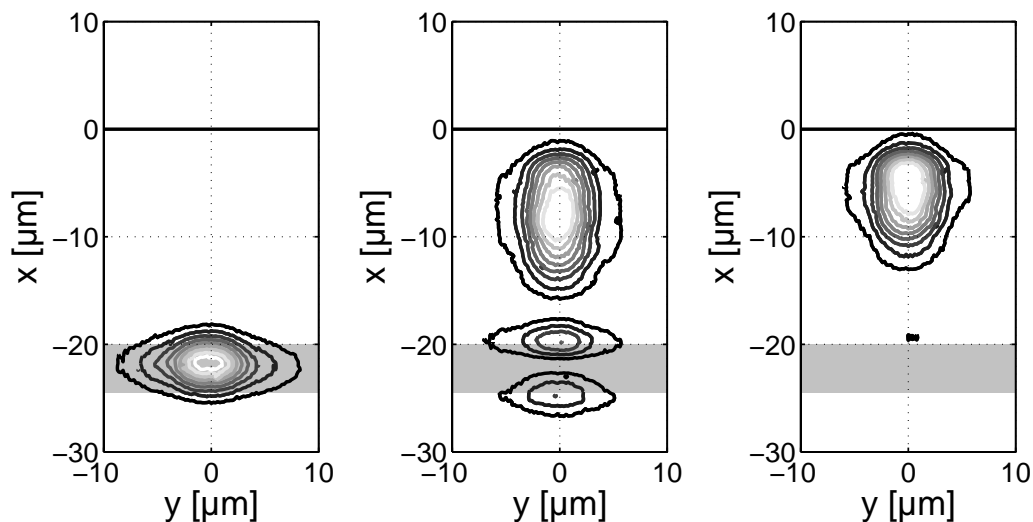


**Figure 5.20.:** Measured near-field intensity distributions at 1.55  $\mu\text{m}$  for different vertical positions of the input fiber. The thick black line at  $x = 0\mu\text{m}$  marks the cladding-air interface and the gray rectangle at  $x = -20\mu\text{m}$  the germanium-doped slab waveguide. The lines shown are equal power lines at 10...90 % of the maximum intensity.

Further experiments have shown that the photosensitivity of the BPSG layers depends on the boron concentration, see the description for sample J1 in

<sup>2</sup>Simulation results courtesy of Michael Krause

## 5. Direct UV-writing of waveguide structures

appendix D. Based on this finding IPHT produced a layer system without any germanium doped layer (see Fig. 5.16(b)). The thickness of the layers was not specially chosen for these experiments and not optimized in terms of inscription of waveguides.

In this layer system straight waveguides were written and the refractive index changes in both layers were measured by the refracted near-field method. As shown in Fig. 5.21(a) there exists a zone, where the difference in the photosensitivity enables a direct writing of waveguides in the lower cladding layer. The measured near-field intensity distribution at 1.55  $\mu\text{m}$  of a waveguide written into this material system is given in Fig. 5.21(b). In contrast to the results obtained for sample A1 no waveguiding inside the cladding layer was observed.

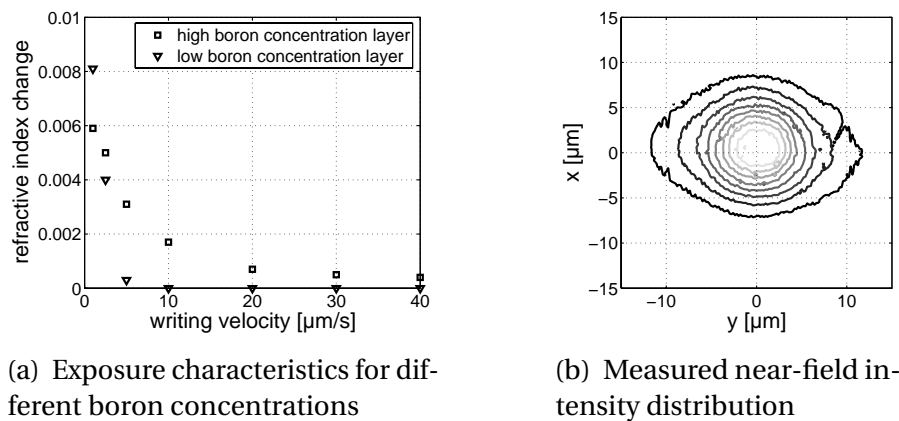


**Figure 5.21.:** Exposure characteristics and measured near-field intensity distribution at 1540 nm of a UV-written waveguide in sample J2. The lines shown in the near-field plot are equal power lines at 10...90 % of the maximum intensity.

By butt coupling of SMF-28 fibers to each side of the sample the insertion losses of the UV-written waveguides were measured. The broadband transmission spectra of a 2 cm long waveguide yields insertion losses of 2.8 dB at 1200 nm and 5 dB at 1600 nm with a linear increase in between. These values include the fiber–chip coupling losses due to the mode mismatch, which were calculated to be  $\sim 1.2$  dB. This yielded propagation losses of  $\sim 1.2$  dB/cm at 1550 nm. A part of this loss is due to the leakage of power into the silicon caused by the insufficient thickness of the buffer layer (see the description for sample J2 in appendix D).

By using an isochronal annealing the thermal stability of the UV-induced refractive index changes in the core and cladding layer of sample A1 were measured. Results of this investigation are given in appendix B.

## 5.7. Waveguide structuring by means of UV-induced refractive index decreases

The work presented in this section was performed in cooperation with the Laboratoire de Physique des Interfaces et des Couches Minces, Ecole Polytechnique (LPICM) and the Université Paris Sud (UPS) within the framework of the PLATON project. The aim was to investigate the applicability of using layers deposited by the matrix distributed electron cyclotron resonance plasma-enhanced chemical vapor deposition (MDECR-PECVD) technique at LPICM for optical applications and compare this technique with mature deposition techniques such as flame hydrolysis deposition (FHD) or radio frequency plasma-enhanced chemical vapor deposition (RF-PECVD). An important part of this investigation was the characterization of the photosensitivity of these layers. Results of this cooperation are published in [7–10].

### 5.7.1. MDECR reactor and performance

The plasma-enhanced chemical vapor deposition (PECVD) is one of the mature deposition techniques for optical waveguide layers. Here, radio frequencies are normally used for the excitation of the plasma. The research in the area of high-density plasmas over the last 20 years has resulted in the development of electron cyclotron resonance (ECR) plasma sources [93]. They are based on the efficient absorption of microwave energy in ECR conditions. Such discharges are remarkably stable and provide a high degree of dissociation, independent control of both plasma density and ion energy, and the possibility of integrating different processes, such as plasma cleaning and thin-film deposition and etching, in one vacuum chamber. Moreover, ECR discharges generate large fluxes of low energy ions, which help to densify the growing film without damaging the substrate, so that no high temperature post-deposition annealing is necessary. Their energy can be controlled independently by applying additional bias to the substrate [94]. The low temperatures during the deposition process allows a wide range of materials to be used as substrates.

Matrix distributed ECR (MDECR) is the latest development stage in the line of distributed ECR plasma sources based on the combination of permanent magnets and multiple microwave antennas [95]. A detailed description of the reactor and its performance is given in [96] and only a brief overview will be given here.

## 5. Direct UV-writing of waveguide structures

The linear alignment geometry of the antennas used in the previous versions of distributed ECR systems has been replaced by a matrix alignment. In the latest configuration 24 antennas were used for the excitation of the plasma. This enables a deposition on large areas (up to  $40 \times 40 \text{ cm}^2$ ) with a high homogeneity and also offers the possibility of deposition on 3D-surfaces [97].

The working pressure range of the MDECR system is between 0.025 and 2.5 Pa and the power levels used per antenna are between 10 and 300 W. Precursors, as in any PECVD process, are supplied as gases, which are dissociated by the plasma in the gas phase and on the surface and thus form growing films. Oxygen, nitrogen and  $\text{C}_2\text{F}_6$  are supplied through a grid located in the most intense plasma region. Silane is provided through 4 tubes which are arranged in a  $8 \times 8 \text{ cm}^2$  square at a distance of 10 cm from the substrate. Germane (2 % dilution in  $\text{H}_2$ ) is injected together with silane. Due to the low pressure operation mode, the number of gas phase chemical reactions is largely reduced and for silica deposition, for example, pure silane and oxygen can be used. For the deposition of germanium-doped silica films silane, oxygen and germane are used. Typical growth rates for silica of 10 to 70 nm/min with a thickness uniformity better than 3 % were achieved. The deposited silica layers are also practically stress-free ( $< 0.1 \text{ GPa}$  for a  $5 \mu\text{m}$  silica film on silicon) [96].

Measurements of the refractive index homogeneity have shown that the homogeneity of the deposited germanium-doped layers is rather poor. For an intended refractive index step of  $10 \times 10^{-3}$  variations in the order of  $7 \times 10^{-3}$  and propagation losses in the order of 1 dB/cm were measured at 1310 nm [98]. Also possible air bubbles inside the deposited layers were visible under an optical microscope. Even if these structures only exist in the cladding layer they can affect the waveguiding properties of the produced waveguide structures. In addition they made the polishing of the end faces, which is necessary for the RNF measurements, quite difficult.

One of the aims for the deposition of optical layers is a low hydrogen concentration inside the deposited layers in order to prevent losses caused by the formation of O-H or other bonds. For a germanium concentration of 3 at%, as used in this experiments, relatively high hydrogen concentration of about 5 at% were obtained [96]. Normally a high temperature post-deposition annealing is applied in order to reduce the hydrogen concentration [99]. On the other hand it is known that a hydrogen-loading of certain materials increases the photosensitivity [57, 58]. A short high-temperature heating (1–2 s,  $1000 \text{ }^\circ\text{C}$ ) of such samples, which creates a large amount of OH-species, locks this photosensitivity [61].

## 5.7. Waveguide structuring by means of UV-induced refractive index decreases

This led to the idea to use the inclusion of hydrogen during the deposition process as a photosensitivity enhancement and, as there is no outdiffusion, also as a locking technique.

Shortly after the deposition of the layers used in these experiments the MDECR reactor at LPICM was dismantled and a new reactor was constructed. Unfortunately LPICM also shifted its attention to the production of silicon oxynitride layers. Therefore, only a limited number of sample materials were available for the following experiments.

### 5.7.2. Photosensitivity experiments

The samples used for these experiments were a two-layer slab waveguide system on top of a silica substrate. The 4.5  $\mu\text{m}$  thick core layer is doped with 3 at% germanium and is covered by a 15  $\mu\text{m}$  cladding of pure silica (see Fig. 5.24(a)). The UV-irradiations were carried out with the setup shown in Fig. 5.2. The laser beam was focused onto the photosensitive core layer by a 10 mm lens to a  $1/e^2$ -diameter of about 4  $\mu\text{m}$ . Hydrogen loaded and non-loaded samples were used and have shown the same qualitative behavior. All results presented in this section were obtained with non-loaded samples. For the photosensitivity tests a series of waveguides with UV-powers of 10 and 35 mW and writing velocities in the range of 5...1600  $\mu\text{m}/\text{s}$  were written.

As described in section 4.2 the first characterization performed on any waveguide structures is a visual inspection. All UV-written lines appeared as light brown lines and were clearly visible under an optical microscope. The checking of the waveguiding properties of the UV-written lines however yielded an unexpected result (see Fig. 5.22).

For the position of the input fiber as shown in Fig. 5.22(a) the light from a fiber-coupled HeNe laser is vertically guided inside the slab waveguide. In the horizontal direction the light is only guided between two UV-written lines. If the input fiber is moved to the position shown in Fig. 5.22(b) the light remains trapped between the UV-written stripes. When the input fiber is aligned with a UV-written line (Fig. 5.22(c)) no horizontal guiding could be observed. If the input fiber is now moved between the next pair of UV-written lines (Fig. 5.22(d)) the light is then guided there.

Such a behavior can only be explained if the UV-irradiation did not yield a positive refractive index change as presented in all the previous sections but a negative refractive index change. In order to check this assumption refracted

## 5. Direct UV-writing of waveguide structures

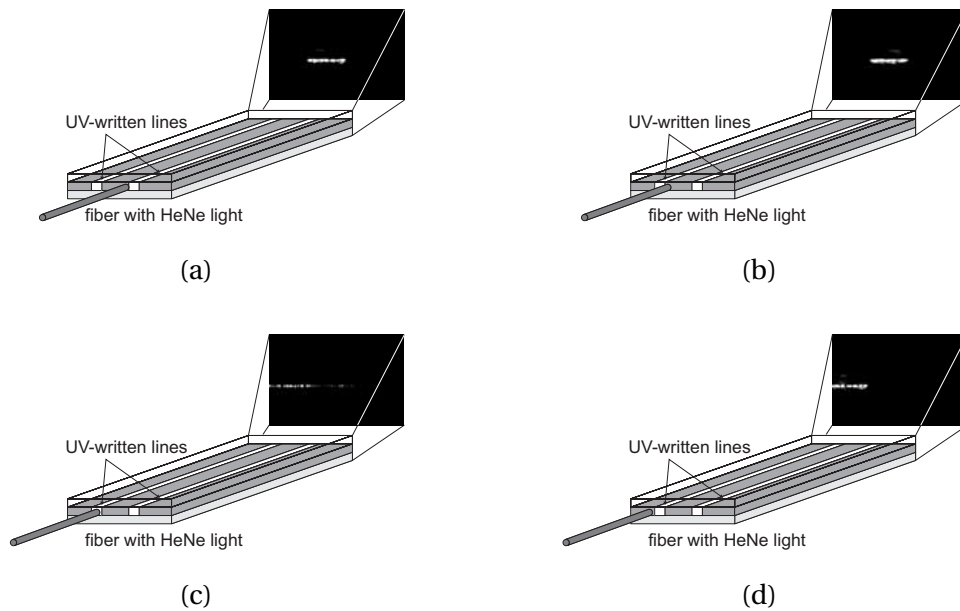


**Figure 5.22.:** Simple experiment for checking the waveguiding properties of the UV-written lines. The observed behavior can only be explained if the UV-irradiation yields in a refractive index decrease of the UV-written lines.

near-field measurements were performed. An example showing an UV-illuminated section with a refractive index decrease of  $10^{-2}$  is shown in Fig.5.23(a) and 5.23(b). The top down order of the different materials in the two-dimensional refractive index distribution shown is: pure silica layer, Ge-doped silica (both deposited by MDECR-PECVD) and the Suprasil<sup>®</sup> substrate.

The relation between index change and writing velocity in a logarithmic scale is shown in Fig. 5.23(c). For all writing conditions tested a decrease of the refractive index inside the germanium-doped core layer was observed. Each point is the mean value of two sections, which are irradiated under the same conditions. For the 35 mW irradiation, measurements could be performed on both end faces of the sample. For several writing conditions the corresponding values differ strongly from each other. The reason for this is not known yet. A possible explanation can be the refractive index inhomogeneity of the deposited layers which can both affect the photosensitivity and the RNF measurements (see section 4.5.2). Some UV-irradiated sections could not be characterized at all because the facets at their position were damaged. Even repeated polishing steps could not solve this problem.

## 5.7. Waveguide structuring by means of UV-induced refractive index decreases

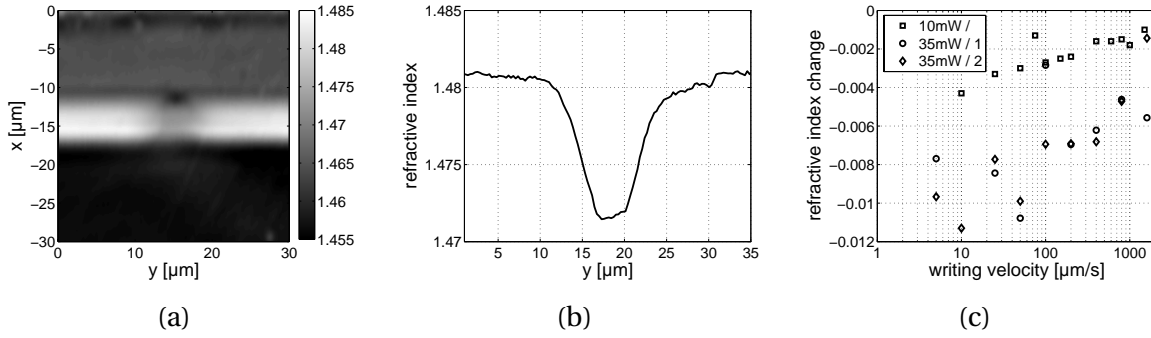


**Figure 5.23.:** Two-dimensional refracted near-field measurement of an UV-illuminated section, horizontal cut through the photosensitive core layer and exposure characteristic. The maximum refractive index changes were about  $-10^{-2}$ .

The amount of UV-induced refractive index change depends on both the UV-power and the writing velocity. For a constant UV-power the amount of index change increases with decreasing writing velocity. Such a behavior is observed for all material systems used in this thesis. The UV-power (or more precisely the power density), however, has a greater influence. Whereas for an irradiation with 10 mW the refractive index changes are lower than  $-4 \times 10^{-3}$ , even for the slowest writing velocities, such index changes are still obtained for the fastest writing velocity, when a UV-power of 35 mW was applied. The maximum measured refractive index changes were in the order of  $-10 \times 10^{-3}$ . Due to the limited number of samples no experiments could be performed with higher UV-powers.

UV-induced negative refractive index changes of planar waveguides have already been reported. Refractive index changes down to  $-6 \times 10^{-3}$  caused by 193 nm excimer irradiation have been presented in [100]. The material used was germanium-doped silica deposited by the HARE device [101]. The estimated germanium concentration was  $\sim 15$  mol% and no detectable levels of hydrogen were present, which make this material different to the one used here. Deuterium-loaded SiON samples and a 248 nm KrF excimer laser were used for the experiments in [102]. A low-fluence pre-exposure after the deuterium-loading was necessary to enhance the photosensitivity. Using UV-written Bragg gratings decreases of the average refractive index as large as  $-1.7 \times 10^{-3}$  have been measured. These Bragg gratings were stable during a isochronal annealing up to  $500^\circ\text{C}$ . Refractive index changes down to  $-6 \times 10^{-3}$  were measured in germanium-doped silica samples with a  $\text{GeO}_2$  concentration of  $\sim 3.3$  at% [103].

## 5. Direct UV-writing of waveguide structures

For these experiments the hollow-cathode plasma-enhanced chemical vapor deposition (HC-PECVD) was used and the irradiations were carried out with a 193 nm ArF excimer laser. In contrast to the presented results in this thesis refractive index increases were observed at the beginning of the exposure curve.

The mechanisms behind these large negative refractive index changes are still not fully understood. In the next section the results of several experiments which were aimed at a better understanding of the mechanisms involved are presented.

### 5.7.3. Photosensitivity mechanisms

In cooperation with the Université Paris Sud a collection of experiments were performed in order to explain the measured UV-induced refractive index changes in the MDECR-PECVD samples. For the measurement of surface changes, IR-absorption and Raman spectroscopy squares of  $400 \times 400 \mu\text{m}^2$  dimensions were UV-irradiated. The used UV-power ranged from 3...57 mW and the writing velocities from 30...1000  $\mu\text{m}/\text{s}$ . Three different sample types were used, see Fig. 5.24. Sample U1 has the same structure as the samples used for the photosensitivity experiments, whereas for sample U2 the cladding layer is missing. Sample U3 is just a pure silica layer deposited on the substrate.

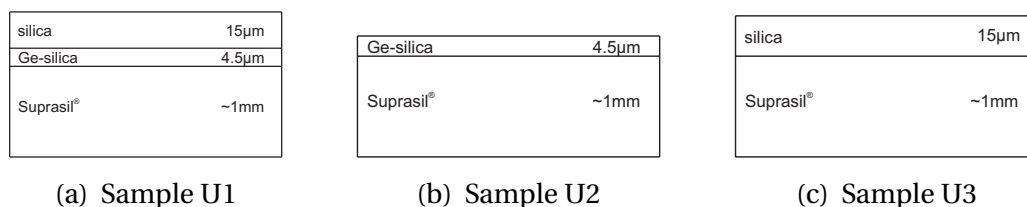


**Figure 5.24.:** Samples used for the determination of the photosensitivity mechanisms.

All shown layers on top of the Suprasil<sup>®</sup> substrate are deposited by MDECR-PECVD.

Due to restrictions imposed by the measurement setup for the UV-absorption another piece of sample U1 was prepared where the size of the squares was increased to  $1000 \times 1000 \mu\text{m}^2$ . This resulted in fewer combinations of UV-power and writing velocity ( $P_{UV} = 4/12/32 \text{ mW}$  and  $v = 100/300/1000 \mu\text{m}/\text{s}$ ).

As the the irradiated areas are much larger than the focussed UV-laser beam the areas were filled by parallel UV-written lines with a spacing of  $2 \mu\text{m}$  (similar to Fig. 5.14(b)). No hydrogen loading was applied for these samples.

## 5.7. Waveguide structuring by means of UV-induced refractive index decreases

The term absorbance as used in the next paragraphs is defined by

$$A(\lambda) = -\lg\left(\frac{I(\lambda)}{I_0(\lambda)}\right), \quad (5.5)$$

with  $I_0(\lambda)$  as the incident and  $I(\lambda)$  as the transmitted intensity. From the differences between the absorbance of a pristine sample and an UV-irradiated area the UV-induced absorption coefficient changes can be calculated by

$$\Delta\alpha(\lambda) = \frac{\Delta A(\lambda) \cdot \ln(10)}{d}, \quad (5.6)$$

with  $d$  as the thickness of the UV-absorbing layer. Additional losses due to UV-induced scattering are neglected. All the measurements shown in the next parts were conducted at the Université Paris Sud.

### UV-absorption changes

As shown in section 3.1.1 UV-induced changes in the absorption in the UV wavelength range can yield a significant change of the refractive index in the 1550 nm region. UV-absorption spectra were measured between 190...300 nm. Fig. 5.25(a) shows the absorbance spectra of a pristine sample and three different UV-irradiated areas ( $P_{UV} = 32 \text{ mW}$ ). All spectra were offset corrected for no UV-induced absorption changes at 300 nm [104]. The UV-absorption in the cladding has been measured and found to be negligible. The measured UV-absorption of the germanium-doped core layer has a maximum at 196 nm with a value of  $1 \mu\text{m}^{-1} = 4.5 \text{ dB}/\mu\text{m}$ . At the irradiation wavelength of 244 nm the absorption decreases to  $0.2 \mu\text{m}^{-1} = 0.8 \text{ dB}/\mu\text{m}$ . This value is in the same range as the measured UV-absorption for the sample I1 from section 5.4 ( $0.13 \mu\text{m}^{-1}$  at 257 nm) [105].

A general decrease of the UV-absorbance for all irradiation conditions is observed. The calculated UV-absorption coefficient changes are displayed in Fig. 5.25(b). As for each irradiation condition two areas were produced, the curves shown are the mean value of the two corresponding areas. In contrast to the results presented in [106] for a germanosilicate preform, the absorption coefficient decreases for all wavelengths and there is no proportionality between the absorption coefficient changes at 195 and 242 nm.

From the Kramers-Kronig relation eq. (3.1) it can be seen that a decrease of the UV-absorption yields a decrease of the refractive index in the NIR-region. A full

## 5. Direct UV-writing of waveguide structures

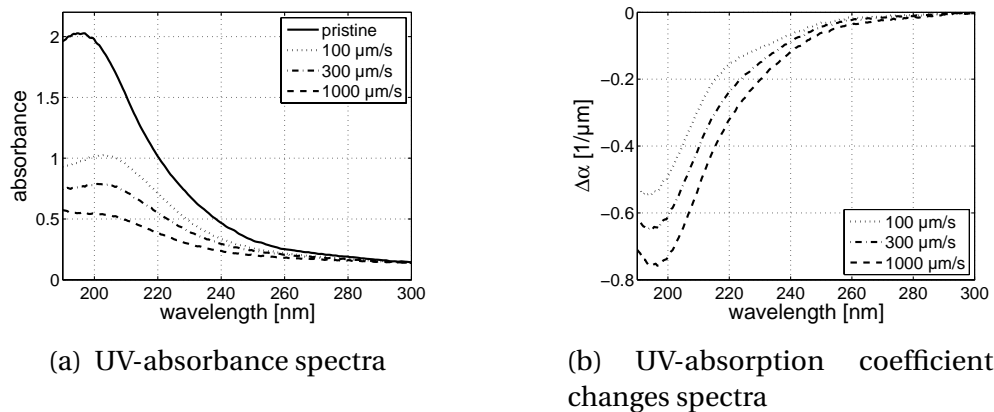


**Figure 5.25.:** Measured UV-absorbance and UV-absorption change spectra for a UV-power of 32 mW.

evaluation of the refractive index changes at 1550 nm due to the UV-absorption changes is given in Fig. 5.26.

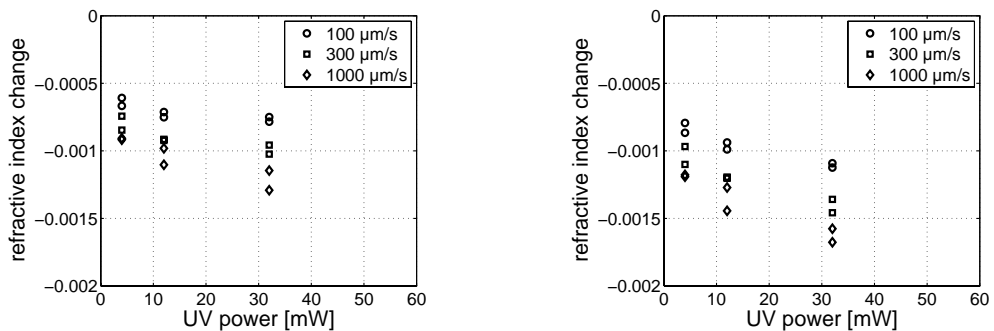


**Figure 5.26.:** Calculated refractive index changes from UV-absorption changes using Kramers-Kronig relation. The left picture shows a direct evaluation of the absorption changes curves, whereas for the right picture the absorption changes were extended down to 150 nm using a gaussian fit centered at the position of the maximum absorption coefficient change.

The values in the left graph were obtained by a direct numerical evaluation of the Kramers-Kronig relation. In [46] it was shown that the main contribution to the refractive index changes comes from UV-absorption changes below 200 nm. Therefore the UV-absorption changes were further extended down to shorter wavelength by fitting a gaussian function into the absorption change maximum and using its short wavelength tail. This procedure is only justified if there

### 5.7. Waveguide structuring by means of UV-induced refractive index decreases

are no absorption peaks below 190 nm, which changes their strength by UV-irradiation. For a germanosilicate preform it was shown in [45] that there were no major bands down to 165 nm. The extension of the wavelength range taken into account resulted in an additional decrease of the index changes by about 25 %. The two markers for each irradiation condition correspond to the two irradiated areas. The maximum refractive index changes calculated from the UV-absorption changes are  $-1.7 \times 10^{-3}$ .

In contrast to the measured UV-induced refractive index changes shown in Fig. 5.23(c) the maximum UV-absorption changes and corresponding calculated refractive index changes are obtained for fast writing velocities instead of slow writing velocities. Furthermore the amount of refractive index changes which can be explained by UV-absorption changes are smaller than the measured refractive index changes. Therefore, an additional effect has to be present.

#### **IR-absorption changes**

UV-induced changes in the IR-absorption can also yield refractive index changes in the 1550 nm region. Therefore IR-absorption spectra were measured in the range  $2400 \dots 4000 \text{ cm}^{-1}$  using a Fourier transform IR spectrometer. The spectral resolution was  $4 \text{ cm}^{-1}$  and an averaging over 64 scans was applied. The IR-absorbance of a pristine sample (U1) is shown in Fig. 5.27(a). In contrast to the UV-induced absorption coefficient changes in the UV-range the absorption coefficient changes in the IR-range are more than one order of magnitude smaller (see Fig. 5.27(b)). In addition both absorption increases and decreases can be observed in the measured wavelength range.

With the exception of the  $15 \text{ mW}/1000 \mu\text{m/s}$  case all measured IR-absorption coefficient changes yield positive refractive index changes via the Kramers-Kronig relation. The changes however remain small (less than  $+5 \times 10^{-4}$ ). The measured large negative refractive index changes can therefore not be explained by changes in the IR-absorption of the core layer.

#### **Raman spectroscopy**

With the help of the Raman spectroscopy UV-induced changes in the density of the oscillation vibrational states of the irradiated material can be detected. Based on this information correlations between structural changes of the glass structure and refractive index changes caused by UV-irradiation can be investi-

## 5. Direct UV-writing of waveguide structures

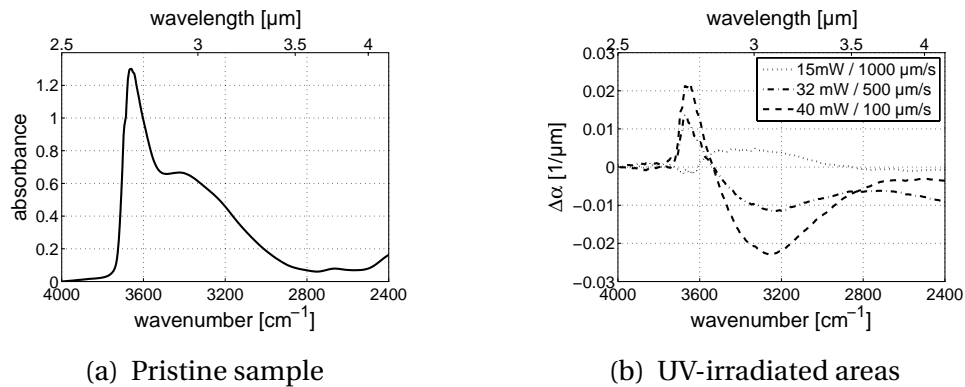


**Figure 5.27.:** Measured IR-absorbance spectra of a pristine sample and UV-induced IR-absorption changes.

gated [107]. Raman spectra were measured using a Raman spectrometer with an Argon laser at 514 nm acting as an excitation source. The spectra were measured from 200...4000  $\text{cm}^{-1}$  and were calibrated against a pure silica sample. After an offset correction all spectra were normalized to their value measured at 440  $\text{cm}^{-1}$ . The Raman spectra of a pristine sample and three different UV-irradiated areas are shown in Fig. 5.28(a). The pristine sample only has a raman signal in the region around 500  $\text{cm}^{-1}$ .

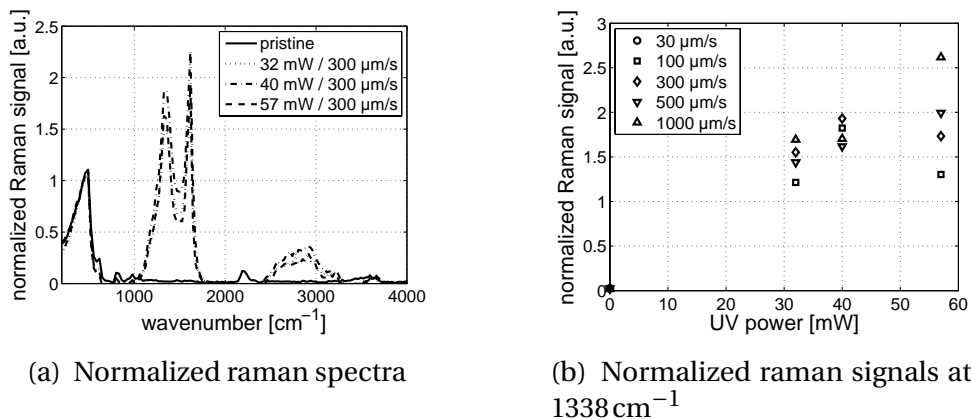


**Figure 5.28.:** Raman spectra of a pristine sample and three different UV-irradiated areas. The right picture shows the evolution of the 1338  $\text{cm}^{-1}$  peak as a function of the irradiation conditions.

The most notable changes in the Raman spectra due to the UV-irradiation are the appearance of new peaks located around 1500  $\text{cm}^{-1}$  and 2800  $\text{cm}^{-1}$ . The

### 5.7. Waveguide structuring by means of UV-induced refractive index decreases

evolution of the  $1338\text{ cm}^{-1}$  peak as a function of the irradiation conditions is given in Fig. 5.28(b). The largest changes are obtained for the highest UV power and fastest writing velocity. A more detailed investigation of this topic including a classification of the involved chemical bonds is given in [10].

#### Volume changes

As pointed out in section 3.1.2 large UV-induced refractive index changes can also be explained by a densification or expansion of the material. Therefore the surface topography of UV-irradiated areas was determined. The measurements were performed with a phase shift interferometer working at 534 nm.

Instead of a densification, normally observed for germanium-doped silica materials, an expansion of the surface was observed for all irradiation conditions on sample U1 and U2 [8,9]. An example of such a surface expansion for sample U1 is given in Fig. 5.29. No surface changes were observed on sample U3, which was expected from the UV-absorption measurements.

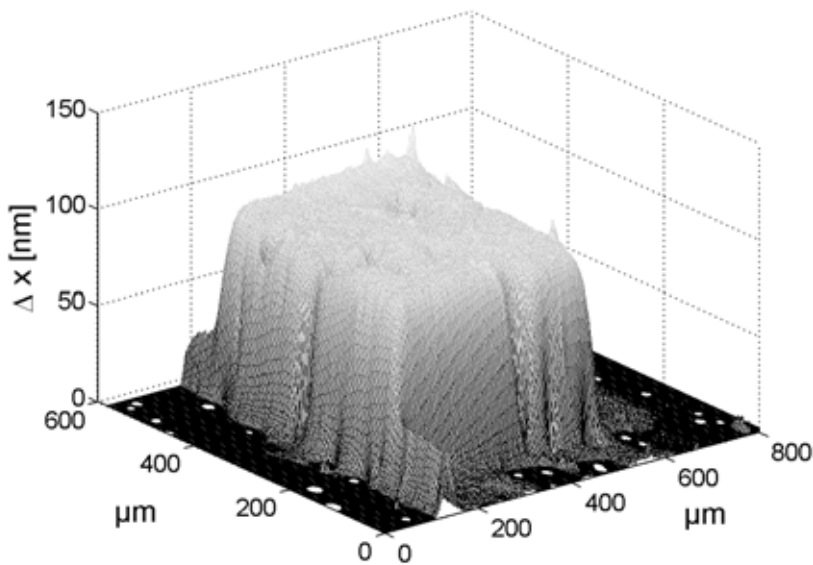


**Figure 5.29.:** Measured surface of a UV-irradiated area (sample U1,  $P = 32\text{ mW}$  and  $v = 500\mu\text{m/s}$ ).

The dependence of the step height  $\Delta x$  of the irradiated areas as a function of the irradiation conditions is given in Fig. 5.30(a). For UV-powers up to 15 mW

## 5. Direct UV-writing of waveguide structures

the surface changes are increasing with decreasing writing velocity. For UV-powers larger than 15 mW this ordering is reversed, which means that the highest surface changes are obtained by the fastest writing velocities. In Fig. 5.30(b) the same data is presented as a function of the writing fluence. From this graph it can be seen that the term fluence is not well suited for the description of this phenomenon. Depending on the combination of UV-power and writing velocity the same fluence value can induce different surface changes. For a fluence of  $1.9 \text{ kJ/cm}^2$  a surface change of 30 nm was obtained for the irradiation with 6 mW and  $100 \mu\text{m/s}$ , whereas the same fluence realized with the combination of 57 mW and  $1000 \mu\text{m/s}$  yielded a  $\Delta x$  of 200 nm.

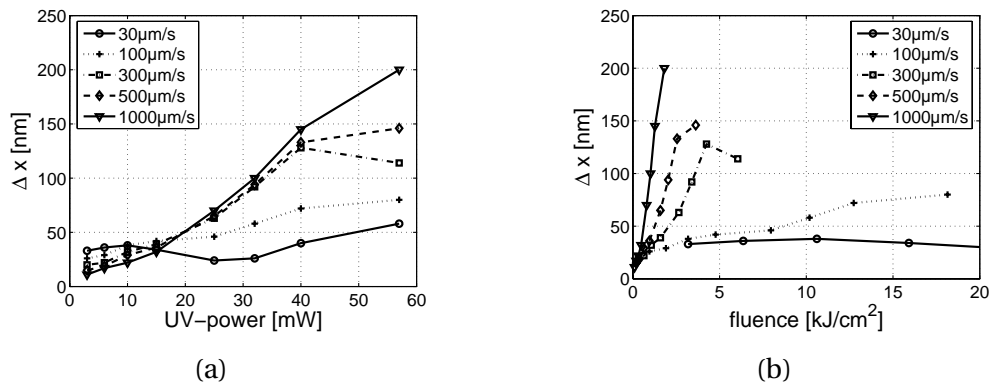


**Figure 5.30.:** Measured surface upshifts of UV-irradiated areas on sample U1.

For constant writing velocities the surface expansions are increasing with increasing writing fluence (see the lines in Fig. 5.30(b)). However, for equal writing fluences the curves are always ordered in the way that higher writing velocities yield larger surface expansions. This implies that the used UV-power (or power density) is the main parameter responsible for this phenomenon.

The fact that the observed surface changes are highest for fastest writing velocities may be explained by a heating effect, which counteracts the expansion process. Calculations have yielded a temperature increase of about 750 K inside the core layer region under focus due to the absorbed UV-power [108]. However, the temperature increase caused by stationary UV-irradiation is not much higher than for fast scanned irradiation. This discrepancy can possibly be solved by the mechanism presented in [105]. The heating of the material in connection with a thermal activation of the included hydrogen can result in a positive feedback loop, so that the UV-induced temperature increase can be even higher and a melting of the material is possible.

### 5.7. Waveguide structuring by means of UV-induced refractive index decreases

From the measured surface upshifts it is possible to calculate the volume changes inside the core layer. Based on them the refractive index changes can be obtained by the Lorentz-Lorenz relation (eq. (3.4)). As the mechanical stresses inside the material are not fully known the following part should only act as a rough estimation in order to show the order of magnitude of the refractive index changes related to densification/expansion of the material.

The step height  $\Delta x$  is related to the dilation free of stress  $\epsilon_0^{\text{vol}}$  inside the core layer. Two effects are responsible for the surface deformations: first the change of thickness of the core layer  $\Delta d$  and second a bulging effect  $\Delta b$  caused by the Flamant forces [109]. The sum of them yields the measured step height  $\Delta x$

$$\Delta d = \frac{1}{3} \frac{1 + \mu_p}{1 - \mu_p} \epsilon_0^{\text{vol}} d \quad (5.7)$$

$$\Delta b = \frac{1}{3} \frac{(1 + \mu_p)(1 - 2\mu_p)}{(1 - \mu_p)} \epsilon_0^{\text{vol}} d \quad (5.8)$$

$$\Delta x = \frac{2}{3} (1 + \mu_p) \epsilon_0^{\text{vol}} d, \quad (5.9)$$

where  $\mu_p$  is the Poisson ratio (0.2 for silica).

For the following considerations a surface hump of 100 nm is taken as an example. This value results in an  $\epsilon_0^{\text{vol}}$  value of 0.028, corresponding to an increase of the core layer thickness by 63 nm. The thickness of the core layer is therefore increased by 1.4 %. For an isolated spot the UV-irradiation would cause an expansion in all three directions. With the exception of the outermost lines of the UV-irradiated areas the expansions in the plane of the core layer are cancelled. Therefore the change in volume is given by the change in thickness alone. With a total volume change of 1.4 % the Lorentz-Lorenz relation eq. (3.4) yields a refractive index change of  $-6 \times 10^{-3}$ . Compared with the measured results this is a little bit too low. What is not taken into account so far is the change of the refractive index induced by the stress field [42], which yields an increase of the refractive index and therefore a reduction of the negative refractive index changes. As no stress measurements were performed with these samples no quantitative statements about the contribution of this effect can be made.

From these observations the best working region for achieving large negative UV-induced refractive index changes would be the combination of high UV-powers and fast writing velocities. This is in contradiction to the measured refractive index changes (see Fig. 5.23(c)), where the highest refractive index

## 5. Direct UV-writing of waveguide structures

changes were obtained with slow writing velocities. Additional experiments are therefore necessary in order to solve this discrepancy. Unfortunately no new samples were available to do so.

The results obtained for sample U2 are shown in Fig. 5.31. In the representation of the surface expansions as a function of the writing power (Fig. 5.31(a)) two different regions are present here, too. The inflexion point of the curves is slightly moved towards 10 mW in comparison to Fig. 5.30(a). In the fluence representation (Fig. 5.31(b)) the curves are always ordered in the way that higher writing velocities yield larger surface expansions. The surface upshifts in this sample are comparable or slightly larger than in sample U1 for the same writing fluences.

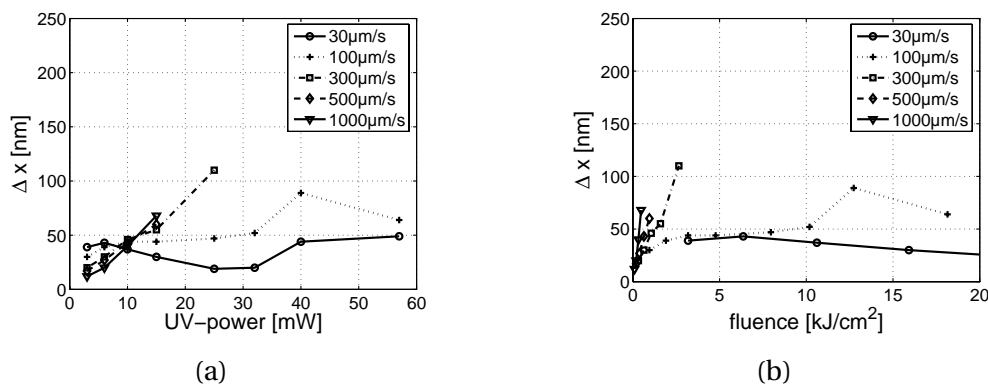


**Figure 5.31.:** Measured surface upshifts of UV-irradiated areas on sample U2.

For the irradiation conditions not shown the surface topography was so irregular and highly damaged that no step heights could be determined. Two microscope pictures of such a surface are shown in Fig. 5.32(a) and 5.32(b). A two-dimensional quasi-periodic arrangement of dark spots can be seen there. The period is decreased when the writing velocity is increased. Atomic Force Microscope (AFM) measurements (see Fig. 5.32(c)) and Raman spectroscopic investigations revealed that these dark spots are germanium microcrystals. A detailed investigation of this phenomenon is still underway.

The following paragraph is a tentative explanation of what may lie behind this observation [108]. Heating due to the UV-irradiation causes germanium to cluster. At high speeds this affects only a narrow region; at slow speeds there is time for germanium to diffuse from a wider region around the UV-beam focus. This means that the next few micrometers in the direction of the laser beam

## 5.7. Waveguide structuring by means of UV-induced refractive index decreases

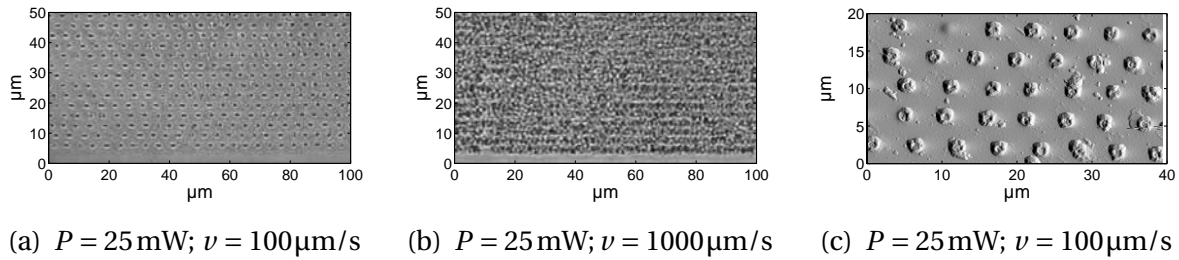


**Figure 5.32.:** Optical microscope (a,b) and atomic force microscope (c) pictures of UV-irradiated areas on sample U2.

movement and the next few scans of the raster have no effect at slow speeds because this region has been depleted. Nothing changes until a fresh region of the material is reached. This speculation is reinforced by a measurement of the height of the microcrystals.

### 5.7.4. Waveguide structuring

In all of the experiments described in the previous sections the waveguide structures were defined by writing the waveguide core using positive refractive index changes (see Fig. 5.33(b)). Waveguide structures can also be patterned by using the aforementioned UV-induced negative refractive index changes. In this case the cladding region of an optical waveguide is directly written by UV-irradiation (see Fig. 5.33(c)). This technique is similar to the matured waveguide patterning using photolithography and reactive ion etching, as shown in Fig. 5.33(a).

As can be seen in Fig. 5.33(c) at least two UV-written lines are necessary for the waveguide patterning. Whereas this seems to be a disadvantage in terms of writing effort there are some advantages associated with this technique. By using the positive DWT the waveguide width is determined by the spot size of the laser used and the interaction of the UV-light with the material. This especially sets a lower limit for the waveguide width. Broad waveguide sections, which are for instance necessary for multi-mode interference couplers can only be realized with multiple writing scans, see Fig. 5.34(a) and section 5.5. This requires long writing times and also the refractive index homogeneity of such waveguides can be a problem. In order to realize a tight confinement of the fundamental mode inside the waveguide core, a high UV-induced refractive index is necessary. The photosensitivity of the core layer material is therefore

## 5. Direct UV-writing of waveguide structures

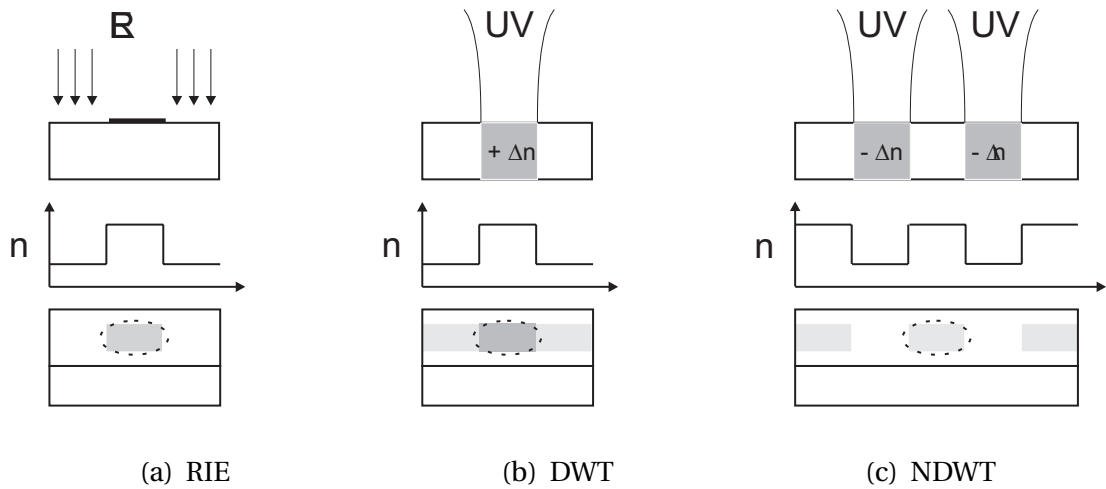
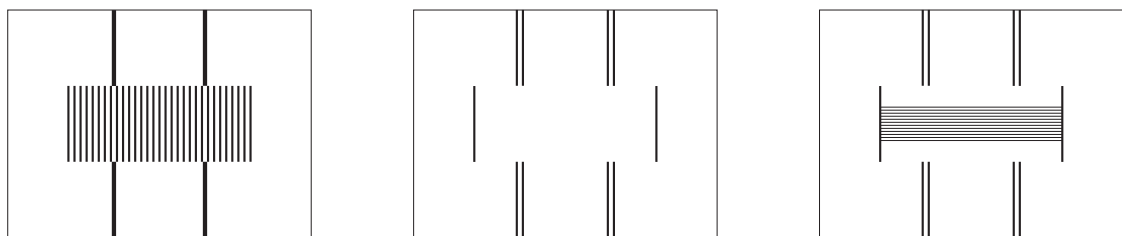


**Figure 5.33.:** Comparison between etching, positive DWT and negative DWT (NDWT). The dashed curves sketch the location and form of the guided fundamental mode.

mainly utilized for the waveguide formation. This leaves only a little amount left for UV-trimming or Bragg grating writing.



(a) MMI coupler realized by DWT      (b) MMI coupler realized by NDWT      (c) MMI coupler with Bragg grating realized by NDWT

**Figure 5.34.:** Comparison of different writing techniques for the structuring of multi-mode interference couplers.

The negative DWT, however, can realize any waveguide width with just two writing scans. This might be advantageous regarding waveguide loss, it exploits the homogeneity of non-UV-irradiated waveguiding regions and substantially decreases the writing times for large area components, see Fig. 5.34(b). In addition, the full photosensitivity of the material remains unused inside the

### 5.7. Waveguide structuring by means of UV-induced refractive index decreases

waveguide core and can be exploited for post processing steps, like Bragg grating writing or phase tuning. Using this technique a fully UV-written realization of the structure sketched in Fig. 5.34(c) [110] seems to be more feasible than with positive refractive index changes.

Using the UV-induced negative index changes multi- and single-mode waveguides were realized by writing the cladding region. The measured near-field intensity distribution of a waveguide defined by two directly UV-written trenches separated by  $10\ \mu\text{m}$  is given in Fig. 5.35(a). The fundamental-mode power is well confined inside the unprocessed region of the slab waveguide.

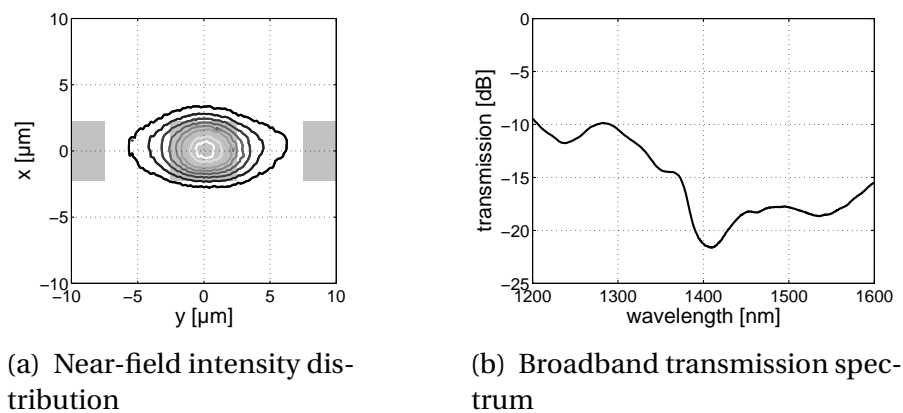


**Figure 5.35.:** Measured near-field intensity distribution at  $1.55\ \mu\text{m}$  and broadband transmission spectrum of a waveguide defined by two directly UV-written trenches separated by  $10\ \mu\text{m}$ . The gray areas represent the unprocessed parts of the slab waveguide and the lines shown are equal power lines at 10...90% of the maximum intensity. The transmission spectrum includes the fiber-chip coupling losses.

The broadband transmission spectrum of a 2 cm long waveguide is shown in Fig. 5.35(b). The large losses at 1400 nm are caused by the absorption of various OH-species. This is typical for layers deposited by PECVD and normally a high temperature annealing is applied in order to remove these species and the associated losses. On the other hand if these species are responsible for the negative photosensitivity observed, a tradeoff between photosensitivity and losses has to be found.

The transmission loss at 1300 nm is about 10 dB. If the fiber-waveguide coupling losses due to the mode mismatch ( $2 \times \sim 1\ \text{dB}$ ) and the measured propagation losses ( $\sim 1\ \text{dB/cm}$  [98]) are subtracted from this value, additional losses

## 5. Direct UV-writing of waveguide structures

of 3 dB/cm remain. These losses can be explained by leakage of power from the defined waveguide structure into the surrounding slab waveguide. Calculations performed on the basis of a simplified measured refractive index profile have shown that the leakage losses can be in the order of several dB/cm<sup>3</sup>. In order to prevent these losses a thicker cladding has to be patterned. This can be achieved by multiple writing scans. As the requirements on the refractive index homogeneity of the cladding are quite low, the spacing between adjacent scans can be chosen to be of the order of the UV-beam spot size or even higher.

Fiber Bragg gratings realized with negative refractive index changes have a better thermal stability compared to their positive index changes counterparts [111]. A good thermal stability of waveguides defined by negative refractive index changes has been reported in [112]. Due to the low number of available samples no high temperature annealing experiments could be performed with the samples used in this section.

According to the writing scheme shown in Fig. 5.34(b) the realization of MMI couplers using the NDWT was also tried. In contrast to the results obtained for positive refractive index changes (see Fig. 5.15) no formation of  $N$ -fold images could be observed. One possible reason for this is the aforementioned insufficient width of the UV-written trenches.

For the case of germanium-doped silica layers, which are mostly used for integrated optical waveguide structures, large UV-induced refractive index decreases have already been reported in [103]. Waveguide structuring experiments with this material are presented in [112]. A 10 mol% germanium-doped silica layer deposited by the hollow cathode plasma-enhanced chemical vapor deposition (HC-PECVD) was used as core layer and a 193 nm ArF laser was used as UV-source. For low fluences an index increase up to  $\sim 1 \times 10^{-3}$  was observed, which was followed by a decrease down to about  $-9 \times 10^{-3}$ . For testing the thermal stability of the waveguides the sample was annealed at 500 °C for 6 hours. No visible degradation of the waveguiding properties were observed. As these experiments were carried out using an excimer laser an amplitude mask was needed for the illumination. The big advantages of the DWT, high speed and flexibility, are therefore missing.

The waveguide structuring by UV-written trenches has also been used for the production of waveguide lasers in a neodymium-doped fluoride glass [113]. The adding of cerium into the waveguide layers provided a strong absorption for

---

<sup>3</sup>Simulation results courtesy of Michael Krause

## 5.8. UV-written waveguides in bulk materials

the used UV-laser ( $\lambda = 244$  nm). Through the UV-irradiation the material in the focus of the UV-beam is heated above its melting point. As the laser beam is scanned across the sample, the photothermally expanded region rapidly cools down, resulting in a lower density and lower refractive index.

The technique presented in [114], where the trenches are created by ablation of the material, is a rather intricate method. Even if the ablated surface is smooth there will be an unwanted interaction of the guided wave with the surrounding media. However, this method has the advantage that it works with a variety of different materials (for instance silica thin films on silicon and  $\text{LiNbO}_3$ ), enables high writing velocities ( $\sim 10$  mm/s) and the lasers used ( $\text{CO}_2$  or Q-switched frequency doubled/quadrupled Nd:YAG) are rather cheap.

## 5.8. UV-written waveguides in bulk materials

In all of the previous sections the materials used had a layered structure (either in terms of refractive index and/or photosensitivity), whereas the samples investigated in this section are bulk materials with a homogeneous refractive index and photosensitivity. The work presented in this section was done in cooperation with Yvonne Menke from the Politecnico di Torino, Italy within the framework of the ODUPE project. The aim was to investigate the influence of Group IV elements (germanium (Ge), tin (Sn), lead (Pb)) on the photosensitivity of the glasses. Some results of this cooperation are published in [11].

### 5.8.1. Motivation

The majority of integrated-optical devices are based on channel waveguides, made out of germanium-doped silica. This material can be produced with high purity resulting in a high uniformity of the refractive index and low losses in the 1550 nm range. However, the active, electro-optical and nonlinear properties are rather small. In addition silica can not be used as a waveguide material for IR applications due to its high losses in this wavelength range.

Therefore, there is a constant research going on for new optical materials. In contrast to the highly sophisticated deposition methods for optical glasses like the chemical vapor deposition, the melt-quenching method offers a simple technique to test new glass compositions. This is possible because no contamination of a reactor or complicated gas phase reactions have to be taken into

## 5. Direct UV-writing of waveguide structures

account. Due to the customizable chemical composition with the capability of incorporating large numbers of glass components, specially designed bulk materials can be produced.

Once an interesting material system is found the first task is to create waveguides out of it. This can be either done by drawing fibers or even nanowires from these materials [115] or by fabricating integrated optical waveguides. For some materials, for instance sulfide chalcogenides, it is possible to fabricate thin films by using conventional thermal evaporation [116]. After this fabrication step integrated optical waveguides can be realized by the mature photolithography and etching process (Fig. 5.1(a)). If such techniques cannot be applied for the glass of interest the waveguide structuring has to take place inside the bulk material. One technique to achieve this is an ion exchange [117]. By using a field assisted annealing even buried waveguides can be realized [118]. This technique however requires that a suitable cation pair can be found.

Another way to achieve waveguide structures inside bulk materials is the use of the direct UV-writing technique [34]. In contrast to experiments with photosensitive Ge-doped silica layers between undoped, non-photosensitive layers (Fig. 5.36(a)), the resulting vertical index distribution in bulk samples is essentially determined by the absorption coefficient for the UV-light (Fig. 5.36(b) and 5.36(c)) [119]. Some details and results regarding the research for glasses with a high photosensitivity can be found in [120, 121].

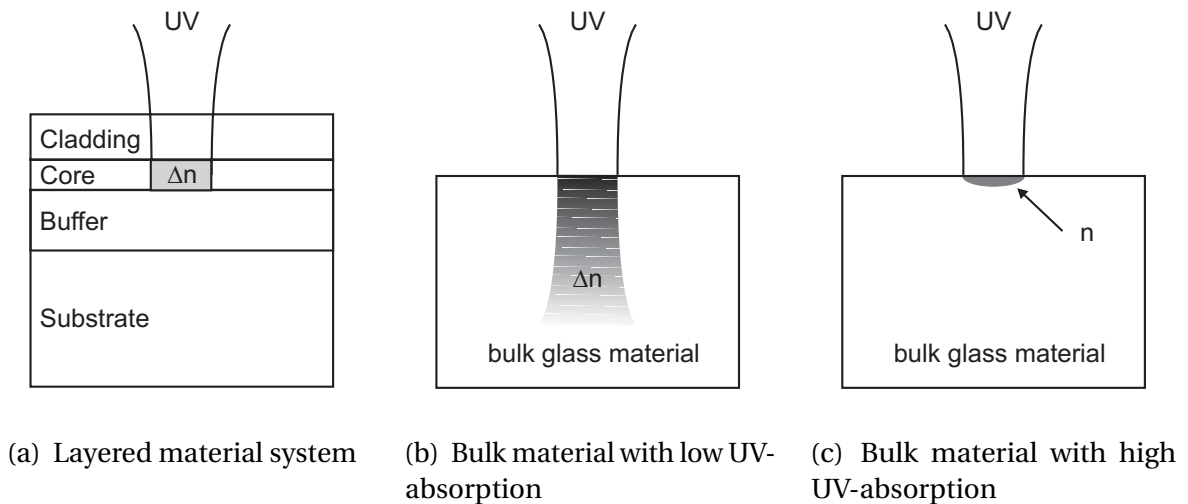


**Figure 5.36.:** Comparison of UV-induced refractive index changes in a layered material system and in bulk glasses with low and high UV-absorption.

## 5.8. UV-written waveguides in bulk materials

In glasses with a low UV-absorption the resulting refractive index changes will look as sketched in Fig. 5.36(b). This usually results in multi-mode slab waveguides (see the vertical lines in Fig. 5.38(b) and the resulting near-field intensity distributions in Fig. 5.40 as an example), which are not wanted for most of the desired purposes. Such a behavior has been shown in silicate glasses with low germanium concentration [122], borosilicate glasses [92] and in rare-earth doped phosphate/fluorophosphate glasses [120]. In order to achieve channel waveguides in such materials several approaches have been successfully demonstrated. In [92] a horizontal slab waveguide was added at the top of the material through ion exchange and the UV-illumination yielded a channel waveguide inside the ion-exchanged layer. By using direct bonding and an intersubstrate ion exchange even buried waveguides were produced by UV-irradiation [123]. This however required additional steps for the fabrication of the material system, so that one advantage of waveguide structures in bulk materials was lost.

A second domain exists for glasses with a high UV-absorption which leads to a small penetration depth of the laser beam. This results in refractive index changes only directly under the surface and the possible formation of channel waveguides as shown in Fig. 5.36(c). Examples for such materials are silicate glasses with high germanium concentration [122], bismuth-oxide based glasses [124], lead silicate glasses [125], chalcogenide glasses [126] and tellurite glasses [70]. All of these fabricated waveguides have the disadvantage that they are located directly under the surface of the material and therefore suffer from interaction with the surface (scattering losses) or the surrounding media (absorption or change of the effective index of the guided modes). In addition large UV-induced refractive index changes are needed in order to overcome the fundamental-mode cutoff. These disadvantages can be avoided by fabricating buried channel waveguides.

The glass used in the following experiments was a multicomponent silicate glass (SGBN – labelled after its components silicon, germanium, boron and sodium). The photosensitivity of SGBN glasses with different germanium concentrations has already been investigated in [122]. The low UV-absorption of 6 mol% GeO<sub>2</sub> glass resulted in slab waveguides written through the full thickness of the samples (~ 1 mm), whereas in the glass with 20 mol% GeO<sub>2</sub> channel waveguides at the surface were produced, see Fig. 5.37. The refractive index changes obtained in both cases were smaller than 10<sup>-3</sup> and the waveguides fabricated were only characterized at 633 nm. The reason that no waveguiding

## 5. Direct UV-writing of waveguide structures

at 1550 nm was shown could be the aforementioned cutoff for the fundamental mode. For the experiments presented here the aim was to have a glass with a UV-absorption as small as possible and a photosensitivity as large as possible and therefore an intermediate germanium concentration of 10 mol% was chosen.

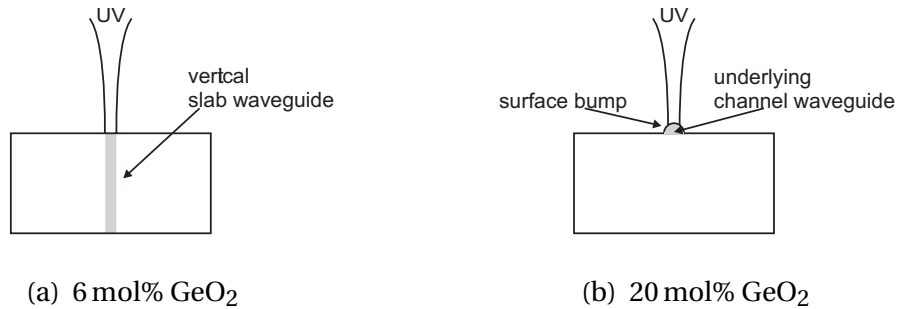


**Figure 5.37.:** Schematic representation of results obtained with different SGBN material systems in earlier UV-writing experiments [122]. In the 6 mol% GeO<sub>2</sub> glass slab waveguides were written through the full thickness of the samples. The UV-irradiation of the 20 mol% GeO<sub>2</sub> glass yielded a surface expansion with an underlying channel waveguide.

### 5.8.2. Preparation/Description of the material

The glass samples were fabricated at the Politecnico di Torino by the standard melt-quenching method. Reagent grade powders of SiO<sub>2</sub>, GeO<sub>2</sub>, H<sub>3</sub>BO<sub>3</sub> and Na<sub>2</sub>CO<sub>3</sub> were mixed in stoichiometric proportions (60 mol% SiO<sub>2</sub>, 10 mol% GeO<sub>2</sub>, 10 mol% B<sub>2</sub>O<sub>3</sub> and 20 mol% Na<sub>2</sub>O) and melted at 1400 °C for 1 h and 1700 °C for 1 h in Al<sub>2</sub>O<sub>3</sub> crucibles. The crucibles were quickly withdrawn from the furnace and the glasses were left inside the crucibles while cooling to room temperature. Annealing of the glasses was carried out at a heating rate of 5 °C/min up to  $T_g$  followed by slow furnace cooling (~ 30 °C/h). The samples were then cut, polished and characterized in terms of physical and optical properties at the Politecnico di Torino, see table 5.1. The glass obtained was X-ray amorphous and transparent. Differential Scanning Calorimetry (DSC) was carried out on a PerkinElmer analyzer in order to determine the glass transition temperature ( $T_g$ ) and a value of 577 °C was measured in this way.

## 5.8. UV-written waveguides in bulk materials

**Table 5.1.:** Physical properties of the SG10B10N20 glass.

property	value	unit
transformation temperature $T_g$	577	°C
density $\rho$	2.6	g/cm <sup>3</sup>
Vickers hardness	5.4	GPa
refractive index at 546 nm	1.5168	
refractive index at 589 nm	1.5131	

### 5.8.3. Vertical slab waveguide inscription

Photosensitivity experiments were carried out with the setup shown in Fig. 5.2. The UV-power of the 244 nm laser was 35 mW and was focused by a 20× UV-microscope objective to a  $1/e^2$ -diameter of about 4 μm onto the sample surface. The bulk sample was mounted on a high-precision two-dimensional translation stage and was scanned under the UV-beam, so that straight lines were written. Different writing velocities ranging from 5 to 1800 μm/s (yielding fluences from 0.6 to 220 kJ/cm<sup>2</sup>) were tested. Neither hydrogen loading nor other pre-treatments to enhance the photosensitivity have been applied. During the UV-irradiation of the material a bright blue luminescence was observed.

The visual inspection of the UV-irradiated sections revealed that all UV-written lines were visible under an optical microscope and no ablation caused by the UV-irradiation was measured. By looking at the end faces, changes in the material were visible up to depths of more than 300 μm, while the structure width corresponded to the width of the writing beam (Fig. 5.38(a)).

In several previous publications about UV-induced refractive index changes in bulk materials, the measurement of the numerical aperture of the fabricated waveguides was used for the determination of the amount of index changes. This method, however, is only valid for multi-mode waveguides. Especially it cannot be applied to single-mode waveguides, where the angular width of the far-field pattern depends on the spot size [127, 128]. Because of the fact, that the reported index changes in the aforementioned publications were rather small, the prerequisite of a multi-mode waveguide was not fulfilled. Also the fitting of index profiles to measured near-field intensities is only an indirect method and requires some assumptions regarding the resulting index structure [129].

## 5. Direct UV-writing of waveguide structures

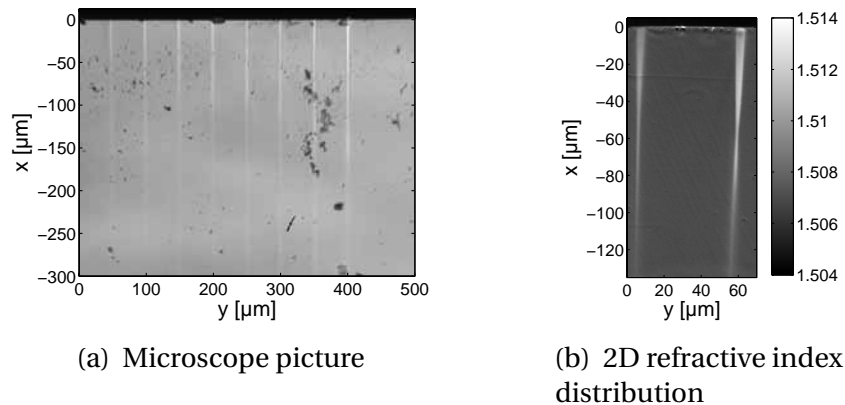


**Figure 5.38.:** Microscope picture and two-dimensional refractive index distribution of the endface of a UV-irradiated SG10B10N20 sample. In the microscope picture the writing velocity is decreased from 65 to 5  $\mu\text{m}/\text{s}$  (left to right). The refractive index measurement shows the two rightmost waveguides.

As it was explained in section 4.5.2 no such assumptions have to be made if the refractive index changes are determined by the refracted near-field method (RNF). The two-dimensional refractive index distribution of the two waveguides written with the highest fluence is given in Fig. 5.38(b). Due to the limited scanning range of the RNF setup it was not possible to measure deeper into the material. The area of refractive index increase has a width similar to the width of the writing beam and a depth of more than 100  $\mu\text{m}$ . As expected, the amount of index increase is highest close to the surface and then decreases slowly with increasing depth (Fig. 5.39(a)).

The relation between refractive index increase and writing fluence is shown in Fig. 5.39(b). For writing velocities higher than 100  $\mu\text{m}/\text{s}$ , i. e. fluences lower than 11  $\text{kJ}/\text{cm}^2$ , no index changes could be determined. The maximum refractive index change achieved was nearly  $5 \times 10^{-3}$ . The solid line shows a power law fit onto the measured data. More experiments are needed in order to check the validity of this model.

The refractive index changes achieved are high enough in order to overcome the fundamental-mode cutoff even for a wavelength of 1.55  $\mu\text{m}$ . Images of measured near-field intensity distributions of the UV-written waveguides at this wavelength are shown in Fig. 5.40. This is the first time that guiding at 1.55  $\mu\text{m}$  was accomplished for directly UV-written waveguides in a bulk multicomponent silicate glass. The four different pictures show the output intensity distribution

## 5.8. UV-written waveguides in bulk materials

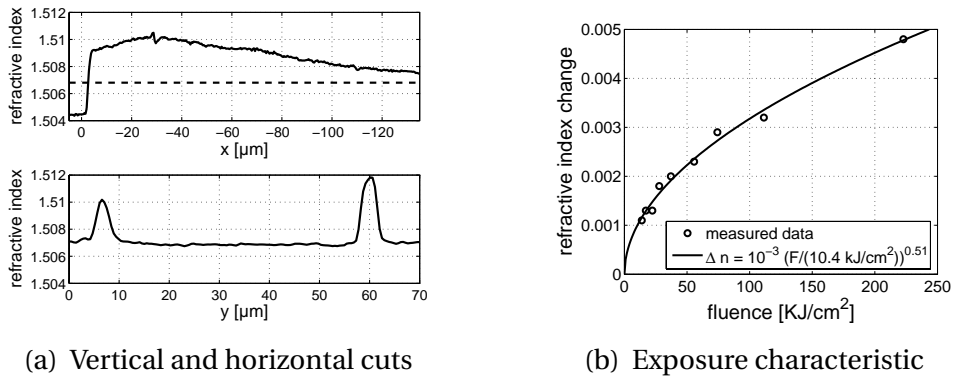


**Figure 5.39.:** Vertical and horizontal cuts of the RNF measurement shown in Fig. 5.38(b) and exposure characteristics of the SG10B10N20 glass. The dashed line in the vertical cut represents the refractive index of the bulk material.

for different vertical positions of the input fiber. The waveguides appear to be single-mode in the horizontal ( $y$ ) direction and multi-mode in the vertical ( $x$ ) direction in accordance with the measured index profiles.

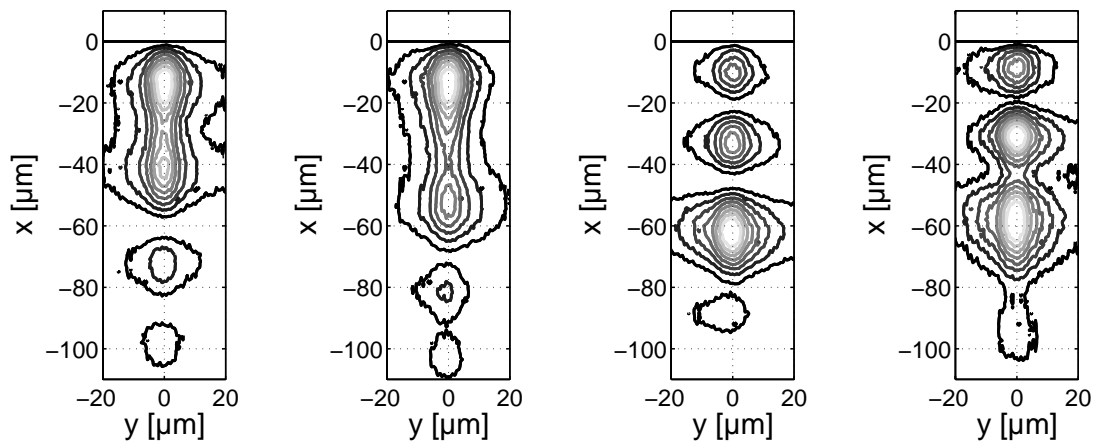


**Figure 5.40.:** Measured near-field intensity distributions at  $1.55 \mu\text{m}$  of a UV-written vertical slab waveguide in a SG10B10N20 bulk glass sample ( $F = 220 \text{ kJ}/\text{cm}^2$ ). The thick black line at  $x = 0$  marks the glass air interface. From left to right, the vertical position of the input fiber is moved  $20 \mu\text{m}$  into the negative  $x$  direction between adjacent pictures. The lines shown are equal power lines at 10...90 % of the maximum intensity.

As mentioned at the beginning of this section, glasses with lead and tin were also investigated within this cooperation but the results obtained were not as

## 5. Direct UV-writing of waveguide structures

good as the presented results. Usually the UV-irradiation resulted in surface trenches, see Fig. 5.41 as an example for tin and lead glasses. These surface trenches possibly resulted in a compaction of the underlying material and a waveguiding at 633 nm was observed there.

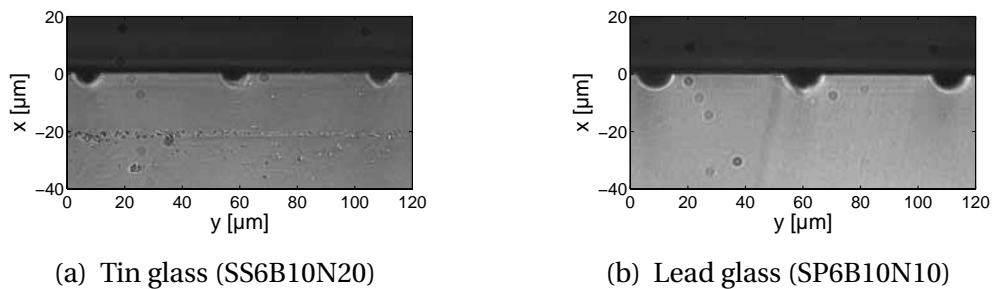


**Figure 5.41.:** UV-induced surface trenches obtained in tin and lead glass samples.

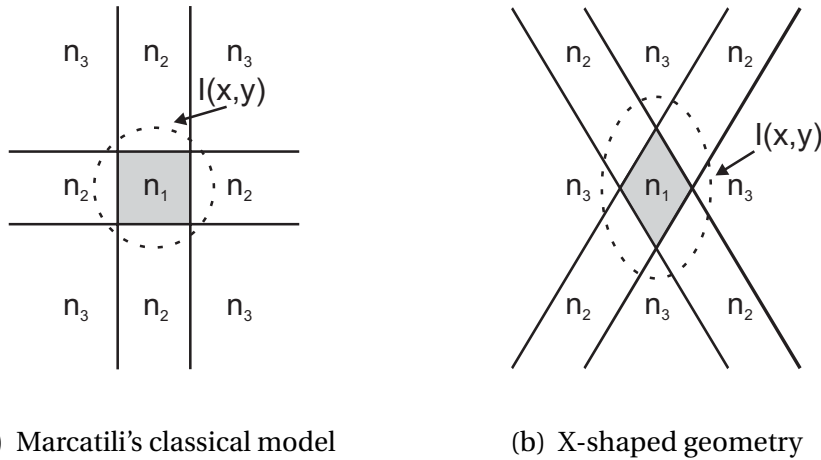
### 5.8.4. Channel waveguide inscription

Whereas the realization of directly UV-written waveguides at  $1.55\ \mu\text{m}$  is already a big improvement in comparison with earlier experiments, these waveguides are still located directly under the surface of the material. In addition the waveguides are multi-moded which is not desired for the majority of optical applications, too. The next step was therefore the development of a writing technique in order to realize buried channel waveguides.

For a dielectric structure to be a waveguide it needs an index core with the surroundings having a smaller index, regardless of what the surrounding structure is. It can be homogeneous as in fibers, or a more complicated structure like the perpendicular superposition of two slab waveguides as in Marcatili's classical model (Fig. 5.42(a)) [130], no matter what the angle between the two slab waveguides is. This idea lead us to superimpose two UV-written slabs as an X-shaped channel waveguide with the channel exactly in the crossing section, see Fig. 5.42(b). This structure is not as strange as it appears, since a channel waveguide fabricated by UV-inscription into a traditional photosensitive slab waveguide is very similar to it. In particular, guided slab modes do exist but are scarcely harmful in either case.

In order to realize such a structure by direct UV-writing a bulk photosensitive material is needed, which has a sufficiently small UV-absorption in order to let

## 5.8. UV-written waveguides in bulk materials



(a) Marcatili's classical model

(b) X-shaped geometry

**Figure 5.42.:** Description of a channel waveguide as a superposition of two slab waveguides ( $n_1 > n_2 > n_3$ ). The dashed curves sketch the location and form of the guided fundamental mode.

the UV-beam penetrate deeply into the material and, at the same time, produces a sufficiently large index increase at UV-illumination. A low attenuation is also required to ensure that the highest index is reached at the crossing and not just below the surface in order to avoid trapping of light there. As shown in the previous subsection the material used fulfills these requirements.

The basic scheme for writing buried X-shaped waveguides into a bulk material is sketched in Fig. 5.43: With a fixed UV-microscope objective ( $40\times$ ,  $NA = 0.8$ ) two skew waveguides were inscribed by using an off-axis focussing arrangement (Fig. 5.43(a) and 5.43(b)). At the intersection of these two slabs a channel waveguide is formed (see Fig. 5.43(c) and 5.44(a)).

The image of the measured near-field intensity distribution of such a buried UV-written waveguide at 1550 nm is shown in Fig. 5.44(b). The fundamental-mode power is well confined to the crossing region. Thus, a buried channel waveguide has successfully been fabricated in a photosensitive bulk material. With an increased angle of the crossed slabs the field ellipticity should decrease even further. The maximum angle is limited by the NA of the lens used and is  $\sim 76^\circ$  with the equipment available. Higher crossing angles could be achieved by using an immersion glycerine lens, which offers a NA of 1.25.

As the attenuation of the UV-laser beam is still not small enough there are also index maxima just below the surface, and a small amount of power is trapped

## 5. Direct UV-writing of waveguide structures

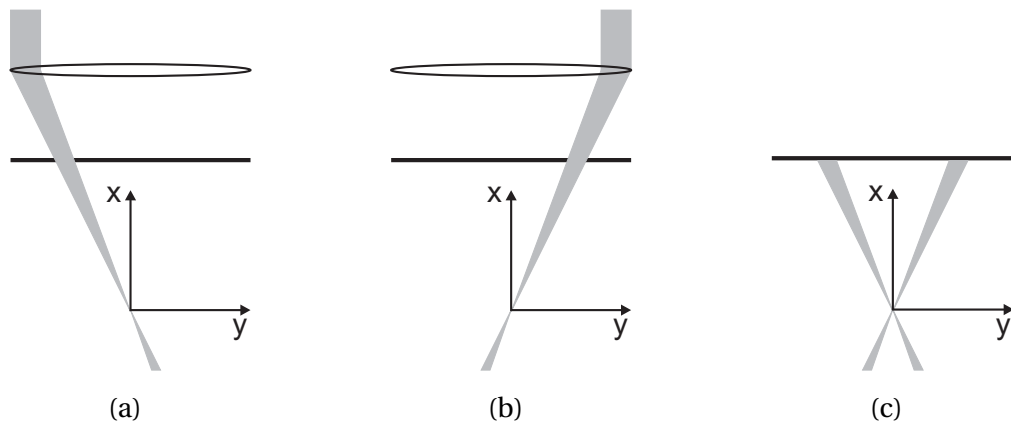


**Figure 5.43.:** Schematic writing setup for buried X-shaped channel waveguides.

there, indicated by the two small lobes in the upper region of Fig. 5.44(b). Further work on the material composition is necessary to avoid such field components.

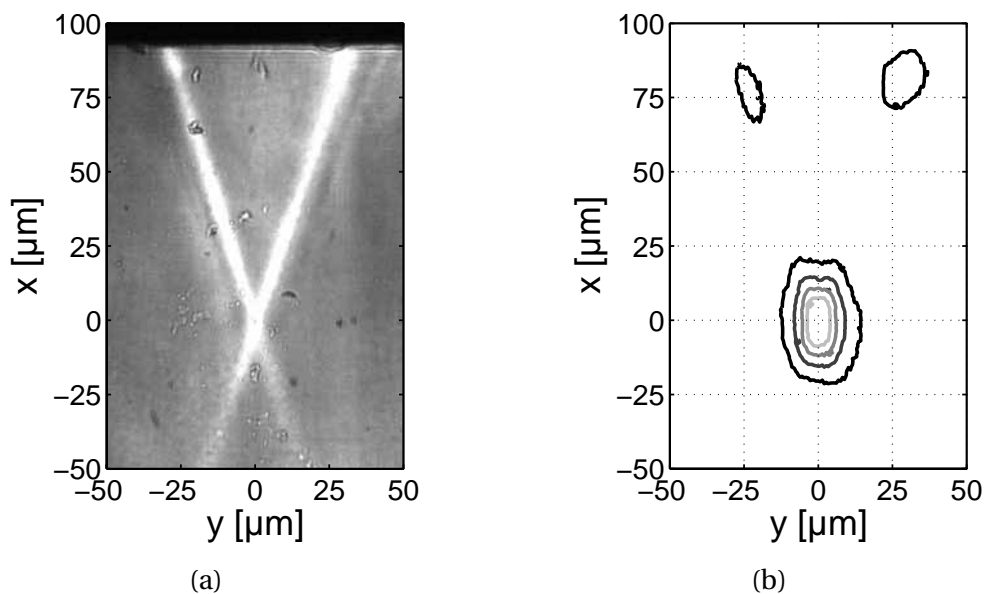


**Figure 5.44.:** Microscope picture of a buried X-shaped channel waveguide and measured near-field intensity distribution at 1.55 μm. The lines shown are equal power lines at 20...80 % of the maximum intensity.

The fiber to fiber insertion loss of a 2 cm long waveguide was measured to be 15 dB with nearly no wavelength dependence from 1200 to 1600 nm. This value includes the fiber-waveguide coupling losses due to the mode-field mis-

### 5.9. UV-Trimming of arrayed waveguide gratings

match, which were calculated to be  $\sim 5.5$  dB per transition. Higher refractive index changes inside the crossing region are necessary in order to get a better confinement and as a result lower coupling losses. The propagation losses were of the order of 2 dB/cm. This is an improvement compared to previous results obtained for UV-written waveguides in bulk glasses (8.2 dB/cm [122] and 3.3 dB/cm [129], both measured at 633 nm).

With this writing technique it is also possible to realize three-dimensional waveguide structures. This can be achieved by varying the  $y$ -position during the writing of the second skew waveguide, which yields a change of the  $x$ -position of the crossing region.

## 5.9. UV-Trimming of arrayed waveguide gratings

In the previous sections the UV-induced refractive index changes were used for waveguide structuring. In this area the direct UV-writing technique has to compete with the mature waveguide production techniques using photolithography and etching. As the core layer material of such waveguides is mostly germanium-doped silica it is also possible to induce refractive index changes by UV-irradiation in such waveguides. The most important applications for this are UV-written Bragg gratings in integrated optical waveguides [131].

With a homogeneous UV-irradiation of the waveguides it is possible to change the effective index even after the etching and the cladding layer deposition. This effect makes the UV-irradiation an ideal choice for a variety of post production trimming processes. The aim of such a trimming is to improve the characteristics and as a result the yield of the produced devices. A simple example is an add/drop-multiplexer based on a Mach-Zehnder interferometer structure. Even with the high precision production steps involved in the production of such a device a trimming is necessary [132]. Another examples are the trimming of the coupling ratio of directional couplers [133, 134], the imbalance reduction of  $2 \times 2$  multi-mode interference couplers [135], the bend-radius reduction of planar waveguides [136] or the spectral improvement of higher order series coupled microring resonators [137].

In this section the crosstalk reduction of arrayed waveguide gratings (AWGs) by means of a post processing UV-irradiation is presented. This work was performed in cooperation with Jörg Gehler from Alcatel, who was responsible for the fabrication and the phase error measurements. Results are published in [12].

## 5. Direct UV-writing of waveguide structures

### 5.9.1. Motivation

In Fig. 5.45(a) the schematic waveguide layout of an AWG and the calculated transmission spectra from one input arm to the 8 output arms are shown. The basic subcomponents are the two focussing slab regions and the waveguide grating in between [138, 139].

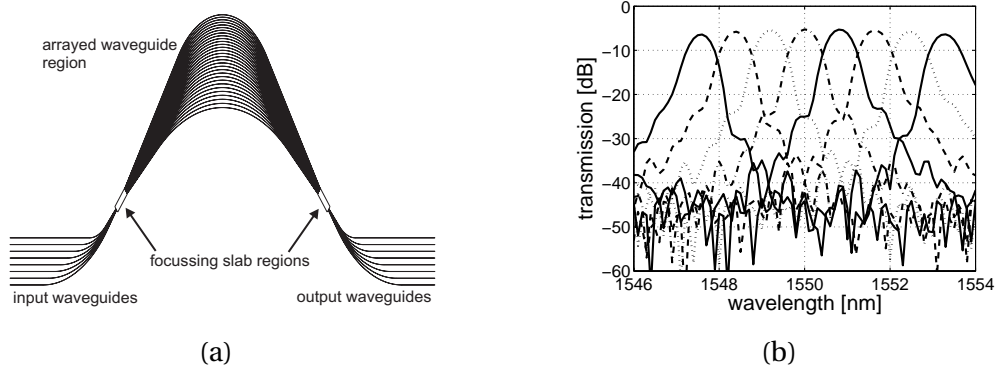


**Figure 5.45.:** Schematic waveguide layout of an AWG and simulated demultiplexing spectra of a 100 GHz AWG.

Its operation is based on the wavelength dispersion introduced by a constant length difference  $\Delta L$  between adjacent waveguides, so that

$$\varphi_n(\lambda) = \frac{2\pi}{\lambda} L_0 + m \cdot n \cdot 2\pi \quad (5.10)$$

with  $\varphi_n(\lambda)$  as the phase of the  $n$ -th waveguide at the wavelength  $\lambda$ ,  $L_0$  as the length of the first waveguide and  $m$  as an integer. This yields a wavelength-dependent phase shift and a wavelength-dependent wavefront tilt in the second focussing slab region. Different wavelengths are now focussed to different points at the back side of the second focussing slab region, causing the demultiplexing of a multichannel signal to different output ports, see Fig. 5.45(b).

Over the last few years, AWGs based on planar silica-on-silicon technology have been developed as optical demultiplexers with channel spacings down to 1 GHz [140]. Especially for high channel counts AWG demultiplexers are a competitive solution in comparison with micro-optic bulk gratings, cascaded interference filters or fiber Bragg gratings. By cascading of two AWG stages a demultiplexing of over 4000 channels has been reported [141].

Important characteristics of such a device are the insertion loss and the cross-talk from the neighboring wavelength channels. Whereas insertion losses can

## 5.9. UV-Trimming of arrayed waveguide gratings

be compensated by optical amplifiers the crosstalk problem is more difficult to tackle. Additional filters after the AWG outputs solve this problem but increase the losses and, more important, the costs. Typical specifications for the crosstalk are values below -30 dB. Fig. 5.45(b) shows that this is not the case for this example. The main origin of crosstalk degradation of AWGs are phase errors of the waveguide grating due to fluctuations of the effective refractive index [142]. The phase fluctuations can be separated into a fast varying part, which is responsible for the crosstalk and a slowly varying part, which determines the chromatic dispersion [143].

Instead of forming a straight line (the linear phase term is removed) the phases of the waves after the waveguide grating resemble a curve like the solid line in Fig. 5.47(a). Several phase compensating techniques including thin-film heaters [144], a-Si strip loaded grating waveguides [145] or phase compensating plates [146] have been proposed. However, all these approaches require additional cleanroom processing steps. Furthermore, thin film heaters require permanent power consumption and also change the phases of the neighboring waveguides. Moreover, this compensation technique is polarization dependent just as the static phase error correction by a-Si strip-loading of grating waveguides. Crosstalk reduction by inserting a phase compensating plate is a rather intricate method and increases the insertion loss.

These disadvantages are avoided if the phase correction is done by using UV-induced refractive index changes. In [147] the arrayed waveguide region of an AWG was UV-irradiated by a 248 nm KrF excimer laser through a triangular mask. As the amount of phase change is proportional to the trimmed length this added a constant optical path length difference to the grating waveguides and resulted in a shift of the transmission peak.

For a typical phase correction of 0.5 rad and a trimming length of 250  $\mu\text{m}$  a refractive index change of  $5 \times 10^{-4}$  is necessary. As such refractive index changes are also possible without hydrogen loading no photosensitivity enhancement was necessary. This enables very precise trimming and does not shift the center wavelength of the device as it would be the case for hydrogen loaded AWGs after annealing.

### 5.9.2. Trimming procedure

The initial state of the phase distribution was determined by using Fourier transform spectroscopy with a low-coherence interferometer [148]. The light of

## 5. Direct UV-writing of waveguide structures

a broadband LED in the  $1.55\ \mu\text{m}$  range and of a  $1.3\ \mu\text{m}$  laser diode is coupled into a Mach-Zehnder interferometer (see Fig. 5.46(a)). One arm contains the device under test whereas in the other arm the optical path length can be changed by means of a cube-corner mirror mounted on a translation stage. A WDM coupler after the interferometer separates the two wavelength signals. The interference of the  $1.3\ \mu\text{m}$  laser is used for a equidistant triggering of the  $1.55\ \mu\text{m}$  signal. By taking the inverse Fourier transform of the individual interferograms the transfer function of the individual grating waveguides can be obtained. The measurement and evaluation time was of the order of several minutes. An online control of the induced phase changes was therefore not possible.

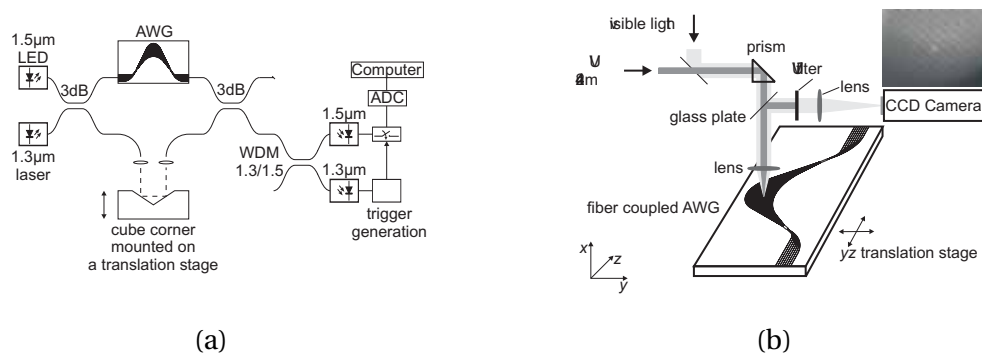


**Figure 5.46.:** Experimental setups for measuring the phase distributions and for the UV-trimming of arrayed waveguide gratings. The inset shows a picture of the arrayed waveguide section with the UV-spot incident on one waveguide.

The experimental setup used for the UV-trimming of AWGs is similar to the setup for directly UV-written waveguide structures. In addition to the setup shown in Fig. 5.2 a mirror with a center hole is used to provide light for a dark field illumination of the sample surface under focus (see Fig. 5.46(b)). The glass plate in front of the focussing lens directs a small part of the reflected light from the sample surface onto a CCD camera. Together with the blue luminescence caused by the UV-irradiation when focused on a waveguide [68], this enables an observation of the UV-spot on the sample surface.

The laser beam with a power of 35 mW was focused down to a spot-size diameter of approximately  $10\ \mu\text{m}$ . During the trimming process the UV spot was moved along the waveguides at a speed of  $0.5\ \mu\text{m}/\text{s}$ . The UV-induced refractive index changes were in the order of  $10^{-3}$  and therefore the trimming sections were usually shorter than  $150\ \mu\text{m}$ . Different sections of grating waveguides

### 5.9. UV-Trimming of arrayed waveguide gratings

corresponding to the measured phase errors were gradually trimmed afterwards and checked by phase measurements. This procedure was repeated until the desired crosstalk reduction was achieved.

#### 5.9.3. Trimming results

The trimmed AWG was designed for a 200 GHz channel spacing and contained 61 waveguides inside the waveguide grating section. The phase distributions before and after trimming are shown in Fig. 5.47(a). The fast phase fluctuations which are responsible for the crosstalk are eliminated. This is also manifested in the comparison of the transmission characteristics of the AWG before and after UV trimming given in Fig. 5.47(b). The crosstalk level has been reduced by about 8 dB to below -35 dB. The residual crosstalk is mainly caused by errors of the amplitude distribution which is not affected by the trimming process.

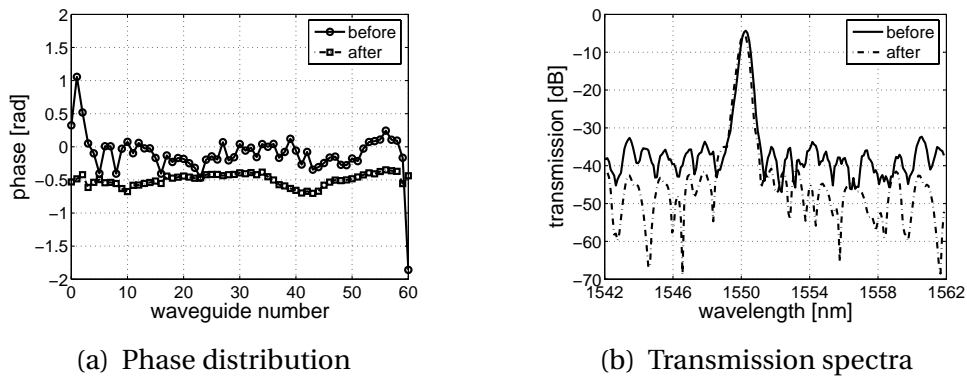


**Figure 5.47.:** Phase distribution and transmission spectra of the 200 GHz AWG before and after UV-trimming.

As the UV-induced refractive index change is positive the phase changes are positive, too. This means that the trimming process is only possible in one direction. In order to realize a constant phase distribution all waveguide phases therefore would have to be trimmed to their lowest value. In our case this would have been waveguide #60 with a value of  $-1.8$  rad. As this is the outermost waveguide with only a small amount of power in it, its influence on the transmission characteristics is rather small. Therefore the value of waveguide #23 was taken as the target for all the other waveguides.

Waveguide #60 was also brought to this value (modulo  $2\pi$ ) by performing a maximum phase correction of 5 rad. This shows that large phase changes can be

## 5. *Direct UV-writing of waveguide structures*

realized with this technique. Even for this large value, changes of the amplitude distribution remained within the error of measurement of about 5 %. Thus, no perceptible additional losses have been introduced. This is in agreement with the very low losses expected [13, 14] for these small index changes and short irradiation lengths (about 250  $\mu\text{m}$ ).

Another important parameter of optical filters for dense wavelength demultiplexing applications is the chromatic dispersion. The Fourier spectrum of the measured interferogram of the phase measurement procedure contains the chromatic dispersion as well [149]. Its value had been improved by the trimming process from a value of -0.7 ps/nm to 0.1 ps/nm within the 1 dB window of the transmission spectrum. This shows that the full complex transmission characteristic of the AWG had been improved by reducing phase fluctuations of the grating waveguides.

At the time of this experiment the writing setup did not contain the high-precision translation stages as presented in section 5.2. A motorized  $yz$ -microscope translation stage with a resolution of 0.5  $\mu\text{m}$  was used. The positioning of the UV-spot onto the waveguides was done manually and the trimming could only be applied on the straight sections of the waveguides. With the translation setup available now, it would be possible to use the layout file of the AWG, so that a fully automatic UV-trimming of all waveguides can be achieved. In combination with wavelength scanning interferometry (section 4.6), which offers a much shorter measurement time, the implementation of a control loop would be possible.

Whereas these experiments were only intended as a feasibility check of an UV-trimming of AWGs, later experiments performed by NTT have shown that this technique can be applied in a commercial environment. Based on the measured phase errors a metal amplitude mask was produced where the length of the exposed waveguides were proportional to the phase compensation values. The irradiations were performed with an unfocussed ArF excimer laser at 193 nm. In [150] the results of this approach are presented for a 25 GHz-spaced 60-channel and a 10 GHz-spaced 160-channel AWG. The same authors have shown that the irradiation can also be applied on the the slab waveguide region [151] and the required amplitude mask can be realized by inexpensive tools like a simple inkjet printer and a copy machine [152]. All these results show that from a technological point of view a UV-trimming of arrayed waveguide gratings is feasible. The decision if such a trimming will be applied in a commercial production line therefore depends on economic issues only.

## 5.10. Conclusion

In this chapter the use of UV-induced refractive index changes for the patterning of waveguide structures was shown. The direct writing technique uses a focussed UV-laser which is scanned over the waveguide sample. By means of a two axis translation stage arbitrary waveguide structures can be produced.

Different material systems were tested for their photosensitivity response. In hydrogen-loaded germanium-doped silica layers UV-induced refractive index changes up to  $10 \times 10^{-3}$  were achieved. In such materials low loss straight waveguides, S-bends and directional couplers were produced. The direct writing technique is also suitable for the fabrication of components containing multi-mode waveguides. As an example  $1 \times 2$ ,  $1 \times 3$  and  $1 \times 4$  splitters based on multi-mode interference couplers were produced.

UV-induced refractive index changes were also obtained in germanium-free material systems. The refractive index changes achieved in non-hydrogen-loaded, boron-phosphorus-doped cladding layers (up to  $9 \times 10^{-3}$ ) were even higher than in the subjacent germanium-doped core layer. The photosensitivity was found to be dependent on the boron concentration. Based on this finding, waveguides were realized in an all germanium free layered material system without any pretreatment.

Large negative refractive index changes (down by  $-10 \times 10^{-3}$ ) were observed in germanium-doped silica layers deposited by MDECR-PECVD. No presensitization was necessary. Several experiments were performed in order to explain these large refractive index changes and waveguides were patterned by writing of the cladding regions.

The direct writing technique was further used for the fabrication of waveguides in bulk glasses. By using a special X-shaped writing geometry buried channel waveguides were realized.

The UV-induced refractive index changes offer a great potential for post processing or trimming of integrated optical components. As an example the fabrication-induced phase errors of an arrayed waveguide grating have been reduced using UV-trimming of the individual grating waveguides.

## 6. Design and realization of Bragg gratings

The work presented in this chapter was performed within the framework of the PLATON project funded by the European Commission. The aim of this project was the realization of integrated optical add/drop-multiplexers (OADM). Low-dispersion Bragg gratings are key components for such devices.

After an introduction to the required specifications for the Bragg gratings some design methods and results obtained with them will be presented. The best results were achieved by using an optimization algorithm. Different Bragg grating designs for a 100 GHz channel spacing will be shown. Based on the designs obtained, Bragg gratings were fabricated using a holographic Bragg grating writing setup which enables full control over the local grating period and strength. Bragg gratings with and without  $\pi$ -phase shifts were written in fibers and integrated optical waveguides.

### 6.1. Introduction

The discovery of the photosensitivity of germanium-doped silica by Hill et al. in 1978 [32] was the starting point for the research on fiber Bragg gratings (FBGs). These first gratings only had a limited area of applications at that time, because the grating period was determined by the writing wavelength. In addition the refractive index modulation was constant over the grating length. These drawbacks were avoided by the external writing method proposed by Meltz et al. in 1989 [33]. With this technique the Bragg wavelength is nearly independent from the writing wavelength and the local grating period and strength can be customized along the grating length.

Based on this full freedom for the realization of the spatial grating structure, fiber Bragg gratings are now used for variety of different applications [153]. Their wavelength-selective transmission and/or reflection properties are used for instance in wavelength division multiplexers/demultiplexers [132], in fiber lasers and amplifiers [154], in photonic signal processors [155], as sensor elements [156] and as compensation elements for chromatic [157] and polarization mode dispersion [15].

In all of these applications the Bragg gratings have to fulfill certain spectral requirements. For the use in lasers the power reflection/transmission spectra are the most interesting properties. For Bragg gratings in add/drop-multiplexers, however, the phase characteristics are also of importance, as they determine the dispersion properties of the final device. The task is to find a spatial grating structure which fulfills these given requirements. The relations between the spatial grating structure and the grating response (time and frequency) are sketched in Fig. 6.1.

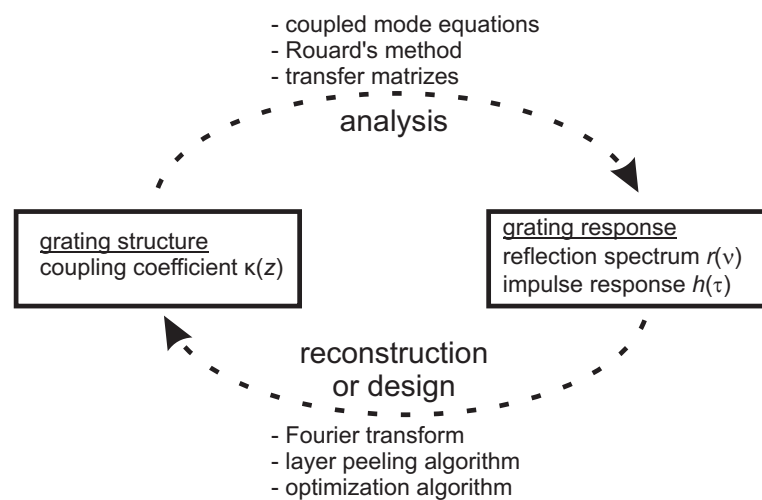


**Figure 6.1.:** Relations between spatial grating structure and grating response.

The coupled mode equations governing the properties of waveguide Bragg gratings have been known for many years [158]. In these equations the properties of the quasi-periodic grating structure are specified by a spatially varying complex coupling coefficient  $\kappa(z)$ , the absolute value of which describes the local grating strength while its phase is associated with the local grating period. Solving these equations yields the transmission and reflection properties for the grating under consideration. The spectra of Bragg gratings with arbitrary local grating strength and period can be determined by dividing the grating into sections with constant grating strength and period. Each of these sections is described by a transfer matrix of a uniform grating and the transfer matrix of the full structure is the product of all individual matrices, see eq. (2.25). From this matrix the transmission, reflection, group delay and chromatic dispersion in transmission and from both reflection sides can be calculated.

## 6. Design and realization of Bragg gratings

It is also well-known how to tackle the inverse problem of finding the necessary  $\kappa(z)$  for a prescribed complex reflection factor  $r(\nu)$ : it is solved by using inverse scattering algorithms. A review of existing methods is given in [159]. The layer-peeling algorithm is one of the best suited methods and a brief introduction will be presented in section 6.3.

### 6.2. Bragg gratings for add/drop-multiplexer

One important application area for Bragg gratings are add/drop-multiplexers. In contrast to demultiplexers, like, for instance, arrayed waveguide gratings (see section 5.9), one or several wavelength channels are dropped from the transmission link. In addition the same wavelength channels can also be added to the data stream, see Fig. 6.2(a). This functionality makes an add/drop-multiplexer perfectly suited for its use in modern telecommunication networks. Such a device was already proposed in the introductory paper of integrated optics in 1969 [30].

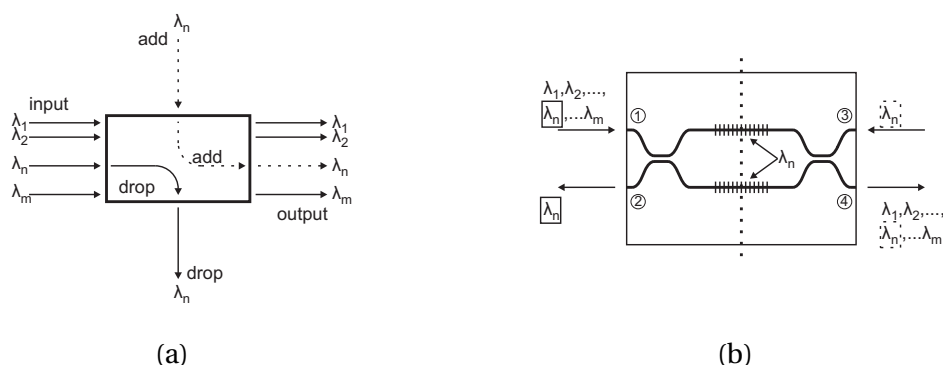


**Figure 6.2.:** Network function of an add/drop-multiplexer and schematic realization based on a Mach-Zehnder interferometer. The device is symmetric with respect to the dashed line.

One realization of an add/drop-multiplexer is shown in Fig. 6.2(b) [132]. It consists of a Mach-Zehnder interferometer with two identical Bragg gratings written into the two interferometer arms. The four ports are usually labeled as follows; port ①: input, port ②: drop, port ③: add, port ④: output. For all wavelengths outside the reflection bandwidth of the gratings this device acts as a Mach-Zehnder interferometer. If the interferometer arms are properly balanced

## 6.2. Bragg gratings for add/drop-multiplexer

all the power of these wavelengths is transmitted to the output port and no light will emerge from the add port. For the wavelengths inside the reflection bandwidth of the gratings this device resembles a Michelson interferometer. If the phase difference between the reflected waves at the first coupler is properly adjusted, all the reflected power from the gratings emerges at the drop port. The device is symmetric to the dashed line, so the same functionality is provided from the add to the output port and enables an adding of wavelength channels to an existing data stream.

The systems specifications for a Mach-Zehnder interferometer-based add/drop-multiplexer, suitable for a 10 Gbit/s WDM system with a 100 GHz channel spacing, were given by ALCATEL [160]. The parts related to the Bragg gratings required are shown in Fig. 6.3.

Three different spectral regions with respect to the Bragg wavelength are defined in the specifications. In the range of  $\pm 10 \text{ GHz} = \pm 0.16 \text{ nm}$  centered around the Bragg wavelength the following specifications are valid:

- transmission below -40 dB
- reflection higher than -0.5 dB
- chromatic dispersion in reflection lower than  $\pm 15 \text{ ps/nm}$ .

In the ranges more than  $\pm 75 \text{ GHz} = \pm 0.6 \text{ nm}$  away from the Bragg wavelength the following specifications are valid:

- transmission higher than -0.5 dB
- reflection below -25 dB
- chromatic dispersion in transmission lower than  $\pm 15 \text{ ps/nm}$ .

In the wavelength ranges in between no specifications are given. The design algorithms are therefore free to distribute the corresponding spectra in these wavelength ranges. It should also be noted that the specifications are only given in terms of *better than* relations, so that every value below is allowed. As it will be shown later, this freedom of design is the main advantage for the optimization based Bragg grating design.

## 6. Design and realization of Bragg gratings

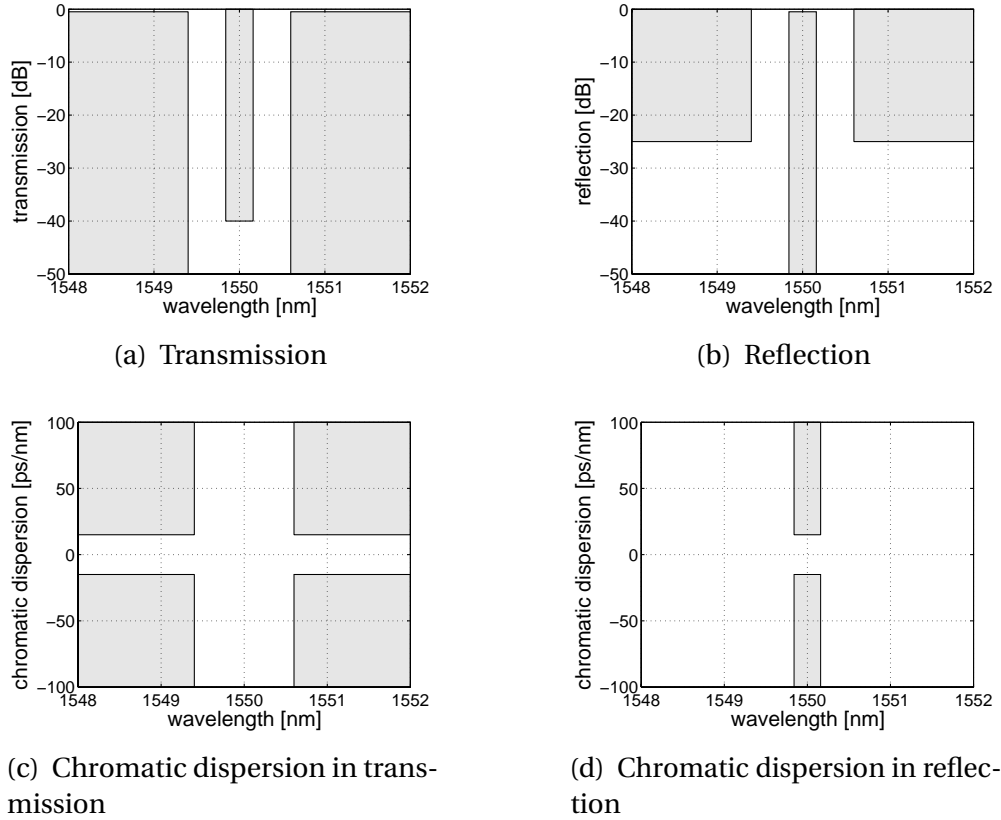


**Figure 6.3.:** Spectral specifications for the Bragg gratings used in a 100 GHz channel spacing OADM [160]. The gray areas represent the forbidden zones.

### 6.3. Bragg grating design by layer-peeling algorithm

Several approaches exist for the design or synthesis of Bragg gratings. A review of the different methods is given in [159]. The most widely used algorithms are the differential methods and in particular the layer-peeling algorithm. It is based on causality arguments and identifies the grating structure recursively layer by layer. A first practical implementation of this principle for the design and reconstruction of Bragg gratings was reported in [73].

#### 6.3.1. Commercial Bragg grating design program

The first attempt to design the required Bragg gratings was done by using a commercial Bragg grating design program [161] based on the so called layer-peeling algorithm [73]. This program needs a complex reflection or transmission

### 6.3. Bragg grating design by layer-peeling algorithm

spectrum as input and calculates the corresponding grating structure. Whereas this is the ideal approach for the reconstruction of Bragg gratings profiles from measured data, it has some disadvantages for the design of Bragg gratings.

The layer-peeling algorithm provides a unambiguous relation between the complex spectra and the grating structure. As the specifications are given with *better than* relations, there exist an infinite number of spectra – all of them within the specifications – which can be used as the input spectra. Each of them will result in a different corresponding grating structure, but some of them will be easier to implement than the other. In addition, the spectrum has to be defined at all wavelengths, even in regions where no specifications are given. This reduces design freedom, which is required in other spectral regions, where the specifications are hard to meet.

In Fig. 6.4 the input spectrum, which was used for the following reconstruction, is shown. For the reflection a super gaussian shape was chosen, whereas the chromatic dispersion in reflection was given as zero over the full wavelength range. The maximum reflection value was calculated in such a way that the -40 dB in transmission are reached.

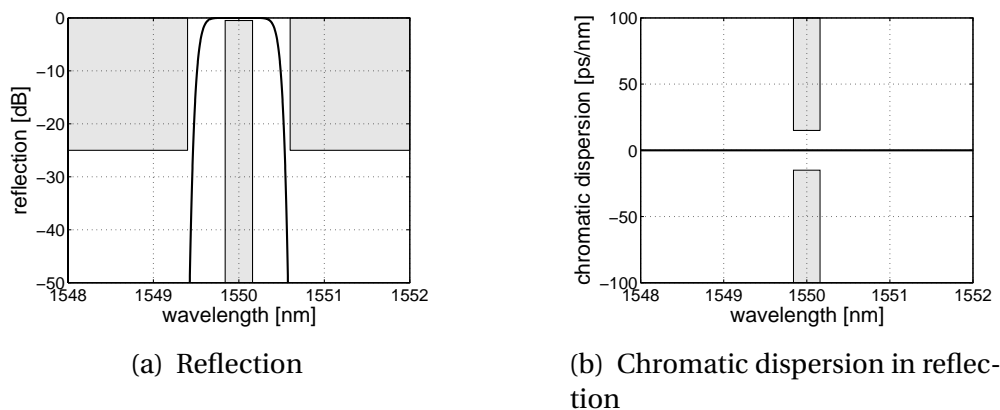


**Figure 6.4.:** Reflection and chromatic dispersion in reflection as input for the layer-peeling algorithm. The gray areas represent the forbidden zones.

Fig. 6.5(a) shows the result of the inverse scattering solver. The length of the grating was fixed to 30 mm by using the option provided to window the resulting grating structure. In order to test the design obtained the corresponding reflection and transmission spectra were calculated using the transfer matrix method. The reflection/transmission and chromatic dispersion spectra are shown in Fig. 6.5(b)–(f).

## 6. Design and realization of Bragg gratings

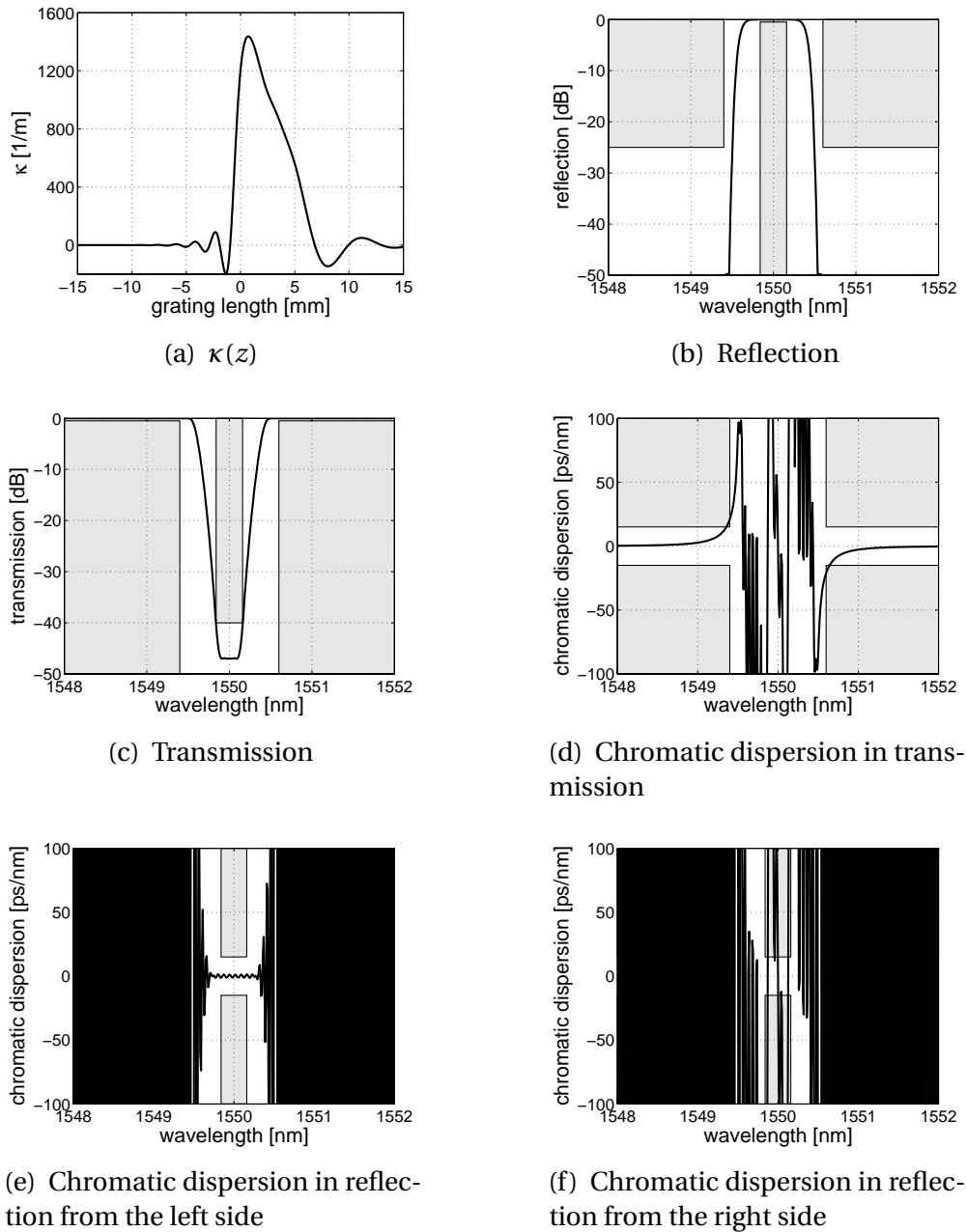


**Figure 6.5.:** Reconstructed Bragg grating structure  $\kappa(z)$  and corresponding transmission/reflection/chromatic dispersion spectra. The gray areas represent the forbidden zones.

### 6.3. Bragg grating design by layer-peeling algorithm

The calculated power reflection spectrum (Fig. 6.5(b)) coincides with the input spectrum (Fig. 6.4(a)), so that the reflection and transmission specifications are fulfilled. The situation for the chromatic dispersion, however, is different. The calculated chromatic dispersion in reflection is not zero over the full wavelength range. This discrepancy to the input spectrum is based on the fact that the complex input spectrum did not belong to a realizable grating. Nevertheless the chromatic dispersion in reflection from the left side only has values within  $\pm 1.5$  ps/nm over the required wavelength range, so that the specifications are fulfilled there. This is not the case for the chromatic dispersion in transmission, where the resulting spectra are exceeding the specifications in a small wavelength range near the edges of the grating stop band. The situation is even worse for the chromatic dispersion in reflection from the right side of the grating. The specifications are missed here by several orders of magnitude. The reason for the different chromatic dispersion curves from both sides of the grating is the asymmetric spatial structure of the grating.

With the approach described so far, it was not possible to design Bragg gratings, which fulfill the specifications from both sides. In the next section an algorithm will be presented, which solves this problem.

#### 6.3.2. Spectrally assisted layer-peeling algorithm

It was shown in the previous section, that it was not possible to design Bragg gratings which fulfill the given specifications from both sides. The requirement that the specifications are fulfilled from both sides of the Bragg grating is automatically fulfilled for spatially symmetric grating profiles. As the layer-peeling algorithm is a unique relation between grating spectrum and grating profile it can only yield a spatially symmetric grating profile if the grating spectrum belongs to such a grating structure.

In this section an algorithm for the determination of spatially symmetric grating structures by a layer-peeling algorithm will be presented [16]. The first step is the creation of a spectrum, which belongs to such a grating. This calculated spectrum is then the starting point for the layer peeling algorithm. In contrast to other design methods for spatially symmetric Bragg gratings like optimization algorithms (see section 6.4) this method is very fast, because there is no need to solve the coupled mode equations in every iteration step.

In general, a single-mode waveguide Bragg grating is a 2-port device which can be characterized by four scattering parameters  $S_{11}$ ,  $S_{12}$ ,  $S_{21}$ , and  $S_{22}$  each of

## 6. Design and realization of Bragg gratings

which is a complex function of the optical frequency. Reciprocity and losslessness reduce the number of independent parameters and further restrictions are due to causality and minimum-phase considerations. The final result [162, 163] yields simple general relations for the absolute values  $|S_{ik}|$

$$|S_{11}| = |S_{22}|, \quad S_{12} = S_{21}, \quad |S_{12}| = \sqrt{1 - |S_{11}|^2} \quad (6.1)$$

and their phase angles  $\Phi_{ik}$ , the latter becoming particularly simple in the case of spatially symmetric gratings which are considered here:

$$\Phi_{11} = \Phi_{22} = -\frac{\pi}{2} - \frac{1}{2} \mathcal{H} \{ \ln(1 - |S_{11}|^2) \}, \quad \Phi_{12} = \Phi_{11}. \quad (6.2)$$

$\mathcal{H}$  denotes the Hilbert transform. These equations show that for spatially symmetric Bragg gratings the power transmission already determines the phase characteristics and in addition that the group delays in reflection and transmission are the same.

On these grounds the design procedure looks like this: First, the target specifications must be fixed. An example is given in Fig. 6.3 where the non-desired (forbidden) ranges of parameters are marked gray. For the starting solution the Fourier approximation eq. (2.26) between grating spectrum and structure was used. Using the coupling coefficient obtained the power transmission is calculated by the transfer matrix method. From this power transmission the chromatic dispersion in reflection is calculated using eq. (6.2). The spectral characteristics obtained are then compared with the given specifications and an overall error value  $\chi^2$  is calculated.

$$\chi^2 = \sum_{i=1}^M (P' - P)^2 \cdot Q \quad (6.3)$$

The vector  $P' = [R'(\lambda), T'(\lambda), D'_R(\lambda)]$  contains the spectral specifications (power reflection, power transmission, chromatic dispersion in reflection), whereas  $P = [R(\lambda), T(\lambda), D_R(\lambda)]$  contains the corresponding values of the calculated spectra. The squared difference between these two vectors is weighted by the elements  $q_i$  of the vector  $Q$ . For different properties different weighting coefficients  $q_i$  are used. In particular the spectral regions where no specifications are given are not weighted at all and the weighting coefficients are also set to zero if the calculated spectra is already lower than the required specifications at that

### 6.3. Bragg grating design by layer-peeling algorithm

spectral position. The error value  $\chi^2$  is then minimized using built-in MATLAB optimization functions (lsqnonlin [164]).

An example of such an optimization run is shown in Fig. 6.6 which was obtained in less than 30 s. The specifications in reflection and transmission are fully fulfilled. For the chromatic dispersion there remained a small wavelength range near the edges of the grating stop band, where the specifications are slightly missed.

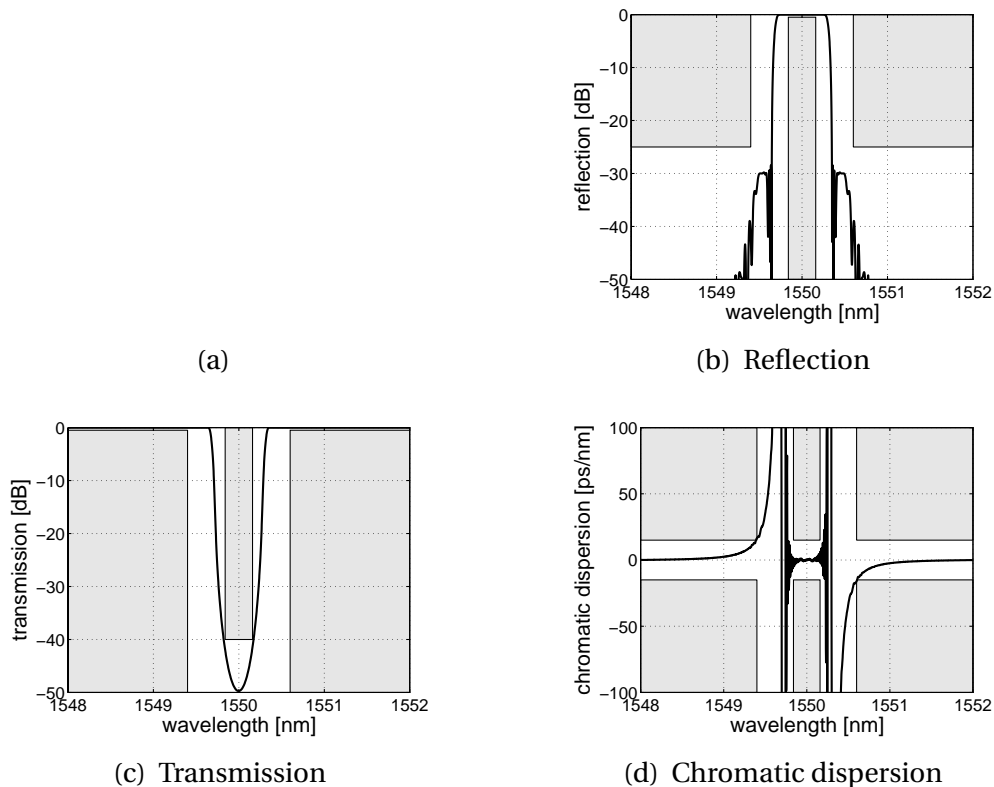


**Figure 6.6.:** Designed transmission/reflection/chromatic dispersion spectra as input for the layer-peeling algorithm. The gray areas represent the forbidden zones.

After having determined the spectral properties which meet the requirements, the spatial structure  $\kappa(z)$  of the grating is determined by using a single run of a layer-peeling algorithm<sup>1</sup>. The resulting grating structure for the above example is shown in Fig. 6.7(a). The grating length was fixed to 30 mm by windowing the resulting grating structure with a Hanning window.

<sup>1</sup>programmed by Sven Kieckbusch using [73]

## 6. Design and realization of Bragg gratings

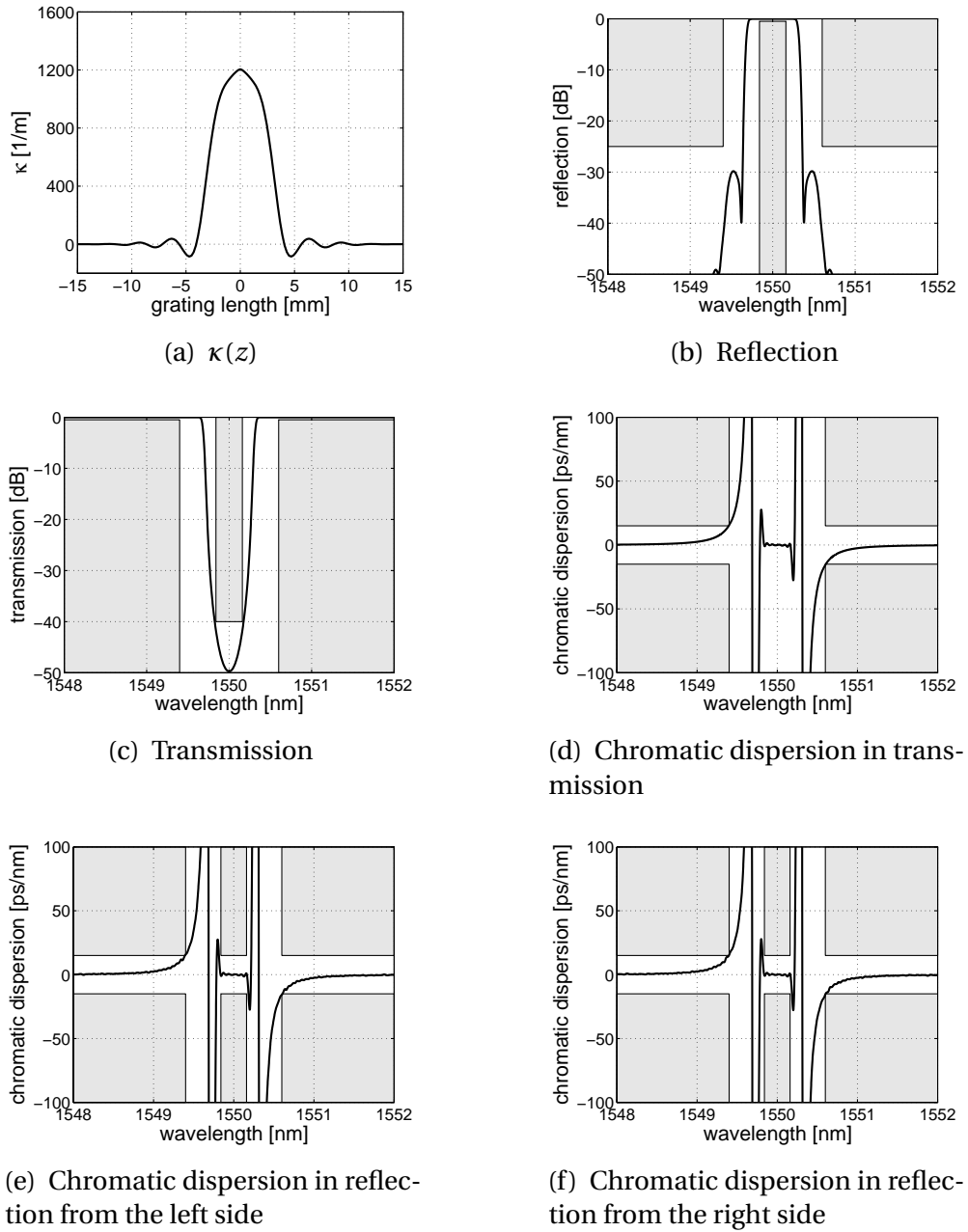


**Figure 6.7.:** Reconstructed Bragg grating structure  $\kappa(z)$  for the spectra given in Fig. 6.6 and corresponding transmission/reflection/chromatic dispersion spectra. The gray areas represent the forbidden zones.

#### 6.4. Bragg grating design by optimization algorithm

In order to verify the design obtained, the corresponding reflection and transmission spectra were calculated using the transfer matrix method. The resulting reflection/transmission and chromatic dispersion spectra are shown in Fig. 6.7(b)–(f).

The grating profile obtained is spatially symmetric. This is also manifested by the fact that the chromatic dispersion curves in transmission and reflection are the same. As expected from the input spectra all specifications, with the exception of the chromatic dispersion in transmission near the edges of the grating stop band, are fulfilled. The slight deviations of the calculated spectra from the given input spectra are caused by the necessary windowing of the coupling coefficient. This problem could be avoided if the design of the input spectra already takes into account the realizability with a finite grating length. Such a design procedure is given in [165].

In conclusion it was shown that by proper choice of the input spectra spatially symmetric Bragg gratings can be designed by the layer-peeling algorithm. With such grating structures given specifications can be fulfilled from both sides of the grating. There remains, however, the question, if the designs obtained can be realized by the available Bragg grating setup. How such additional constraints can be taken into account will be shown in the next section.

### 6.4. Bragg grating design by optimization algorithm

In this section a Bragg grating design algorithm will be presented which enables the full consideration of constraints imposed by the Bragg grating writing facility used. Examples for such constraints are maximum grating length, capability of realizing  $\pi$ -phase shifts and maximum spatial frequencies for the coupling coefficient.

#### 6.4.1. Algorithm

The design procedure used is based on optimization algorithms [166, 167]. Starting from an initial guess of the coupling coefficient  $\kappa(z)$  the transfer matrix method is used to calculate the transfer matrix of the full grating. From the transfer matrix the transmission, reflection, group delay and chromatic dispersion in transmission and from both reflection sides are obtained. Like in the

## 6. Design and realization of Bragg gratings

previous section the spectral characteristics obtained are compared with the given specifications and an overall error value  $\chi^2$  is calculated.

$$\chi^2 = \sum_{i=1}^M (P'_i - P_i)^2 \cdot Q_i \quad (6.4)$$

The vectors  $P'$  and  $P$  are expanded compared to the previous section.  $P' = [R'(\lambda), T'(\lambda), D'_T(\lambda), D'_{R1}(\lambda), D'_{R2}(\lambda)]$  contains the spectral specifications (power reflection, power transmission, chromatic dispersion in transmission, chromatic dispersion in reflection from the left side, chromatic dispersion in reflection from the right side) and  $P$  the corresponding values of the calculated spectra. The weighting coefficients  $q_i$  are used in the same fashion as in the previous section. In this work a nonlinear least square algorithm (lsqnonlin [164]) and a differential evolution algorithm (devec3 [168]) were used to minimize  $\chi^2$ . Only unchirped gratings were considered, so that the complex value  $\kappa(z)$  can be reduced to a real value. The negative values for  $\kappa(z)$  are realized later on with  $\pi$ -phase shifts.

As it was pointed out in the previous sections, it is absolutely necessary that the specifications are fulfilled from both sides. The easiest way to achieve this is to consider spatially symmetric gratings only, because this results in equal reflection properties of the gratings from both sides. For this special case also the group delays and chromatic dispersions in reflection and transmission are the same. Therefore only a single chromatic dispersion curve is shown in the following figures.

In the early design stages it was found that for good design results (especially for the chromatic dispersion) the length of the individual grating sections has to be in the order of 100  $\mu\text{m}$ . As the grating length will be of the order of several millimeters this results in a large number of unknown values to be optimized and yields long computation times. This drawback was avoided by using longer grating sections and using cubic splines for the intermediate values. By using this approach and taking advantage of the demanded spatial symmetry of the coupling coefficient (only one half of the grating structure has to be designed) the number of values to be optimized could be dramatically reduced. In order to find a decent starting solution for the optimization algorithm once again the Fourier approximation between coupling coefficient and reflection spectrum eq. (2.26) was used.

#### 6.4. Bragg grating design by optimization algorithm

The constraints which can be taken into account are the grating length, existence of  $\pi$ -phase shifts, maximum values and maximum spatial frequencies for the coupling coefficient. This enables the design of Bragg gratings which are fully adapted to the material systems and writing facility used. Through the choice of the weighting factors  $q_i$  certain spectral characteristics can be emphasized.

##### 6.4.2. Designs

Based on the algorithm presented, Bragg gratings for use inside a MZI-based OADM were designed. The main focus was put on a design for a 100 GHz channel spacing, for which the spectral requirements are shown in Fig. 6.3. Calculations for a 50 GHz channel spacing and a 400 GHz waveband filter were also performed, but the results will not be presented here. As all designs are spatially symmetric, the chromatic dispersion spectra in transmission and reflection are the same. Therefore only one curve is shown for the chromatic dispersion.

The first design runs were based on the maximum allowed length for the Bragg gratings, which was fixed to 30 mm [160]. Fig. 6.8 shows a design obtained which fulfills all specifications. The impression that at several locations the specifications are not fulfilled is caused by the linewidth used to display the spectra. By zooming into the problematic sections it was made sure that the spectral curves are always inside the white areas. This statement is valid for all the designs presented in this section.

The margins for the reflection spectra are quite high, whereas this is not the case for the required width of the transmission dip and for the chromatic dispersion in transmission. As the amplitude and phase characteristics of Bragg gratings are related to each other, it is not possible to improve one characteristic without affecting the other. By a proper choice of the different weighting factors  $q_i$ , a tradeoff has to be found. It should be noted that even for grating lengths up to 100 mm no significant improvement could be achieved.

Such long grating designs require that the waveguide properties are constant over the full grating length. Whereas this is no problem for fibers, it can impose a problem for etched channel waveguides. In addition, phase masks longer than 25 mm are quite expensive. Shorter grating designs are therefore preferable. Since the amplitudes of  $\kappa(z)$  outside the central part of Fig. 6.8(a) are quite low, a shorter design seems to be possible.

## 6. Design and realization of Bragg gratings

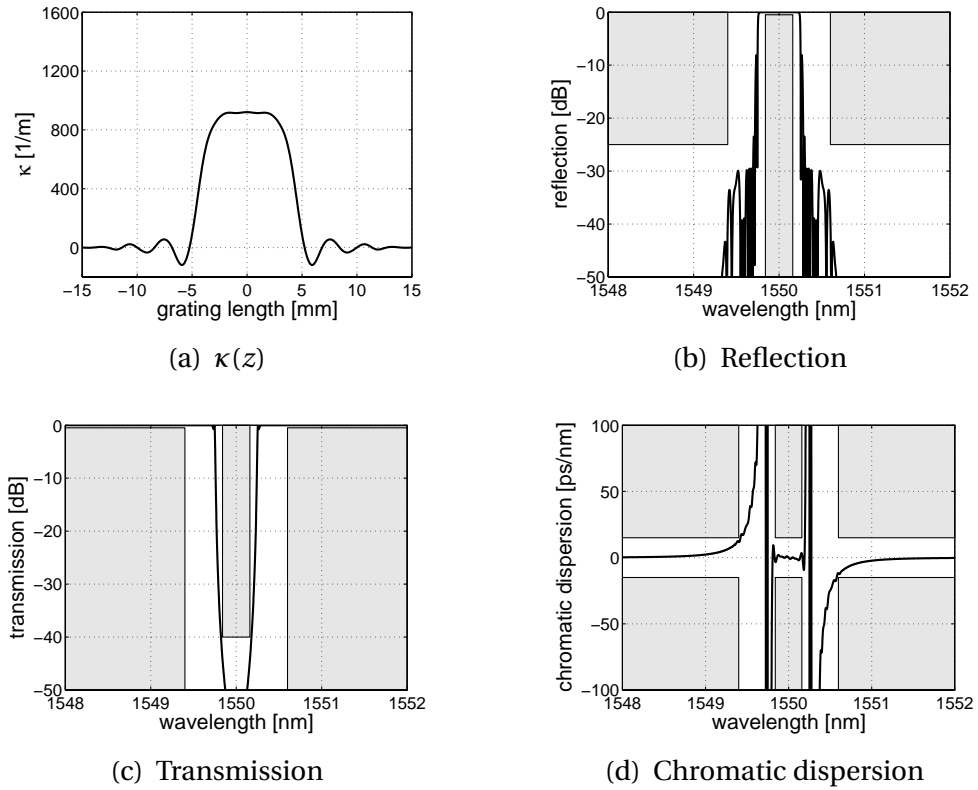


**Figure 6.8.:** 30 mm long Bragg grating design  $\kappa(z)$  for a 100 GHz channel spacing and corresponding transmission/reflection/chromatic dispersion spectra.

As the available phase mask for the realization of the designed gratings only had a length of 15 mm, the following designs were based on this practical limitation. The length was further restricted to 13 mm in order to avoid the outermost sections of the phase mask. Fig. 6.9 shows such a design, which still fulfils all specifications. In comparison to the result obtained for the longer grating length, the grating strength required is slightly higher and more importantly the margins are smaller. Whereas for the 30 mm long design the dispersion in reflection stays within  $\pm 4$  ps/nm, this value is increased to  $\pm 14$  ps/nm for the 13 mm long design.

As already mentioned earlier, in most of the published papers about Bragg grating design the chromatic dispersion in transmission was not taken into account. Using the algorithm presented this omission can easily be implemented by setting the corresponding weighting factor  $q_i$  to zero. Such a design is shown in Fig. 6.10.

#### 6.4. Bragg grating design by optimization algorithm

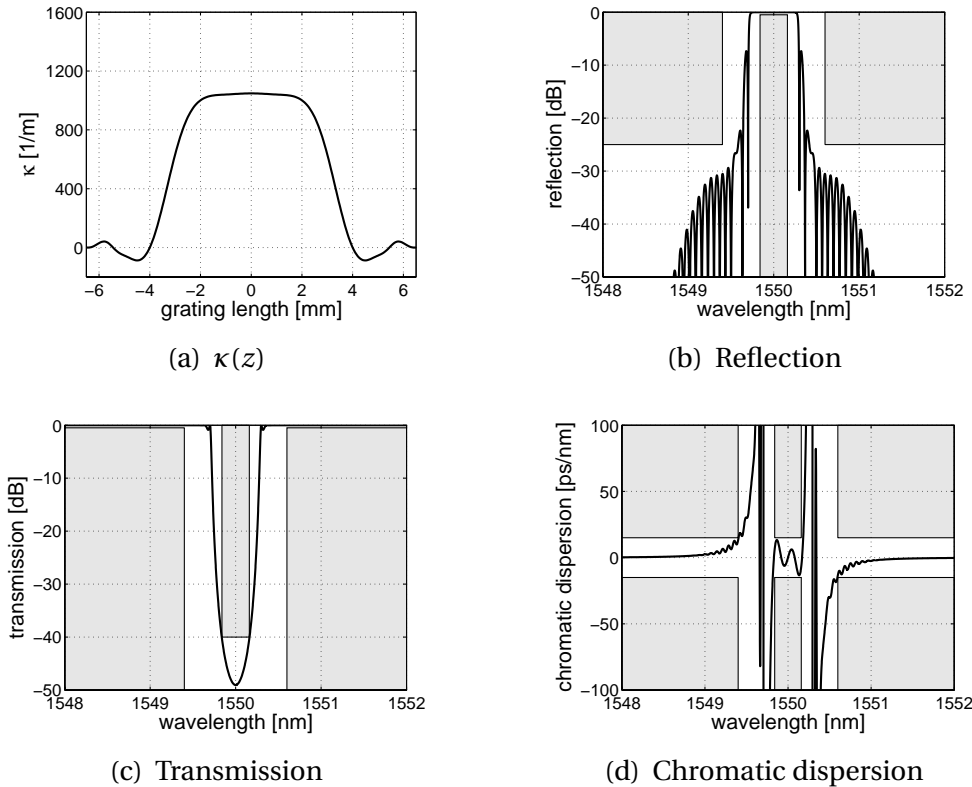


**Figure 6.9.:** 13 mm long Bragg grating design  $\kappa(z)$  for a 100 GHz channel spacing and corresponding transmission/reflection/chromatic dispersion spectra.

This limited set of specifications enables a design with greater margins regarding all remaining specifications. The width of the transmission curve at -40 dB is increased to 0.5 nm, all neighboring wavelength channels are suppressed by at least -40 dB and the chromatic dispersion inside the reflection band is smaller than  $\pm 0.5$  ps/nm. However, the grating strength required is about 50 % higher than in the previous design.

Further discussions with systems designers are necessary in order to find out how detrimental the higher values for the chromatic dispersion in transmission within the small affected spectral range are for the whole system. Certainly a compromise between system aspects and grating writing capability has to be found.

All the grating designs presented so far require the incorporation of  $\pi$ -phase shifts in order to realize the negative values for  $\kappa(z)$ . Depending on the level of sophistication of the Bragg grating writing setup used,  $\pi$ -phase shifts are difficult

## 6. Design and realization of Bragg gratings

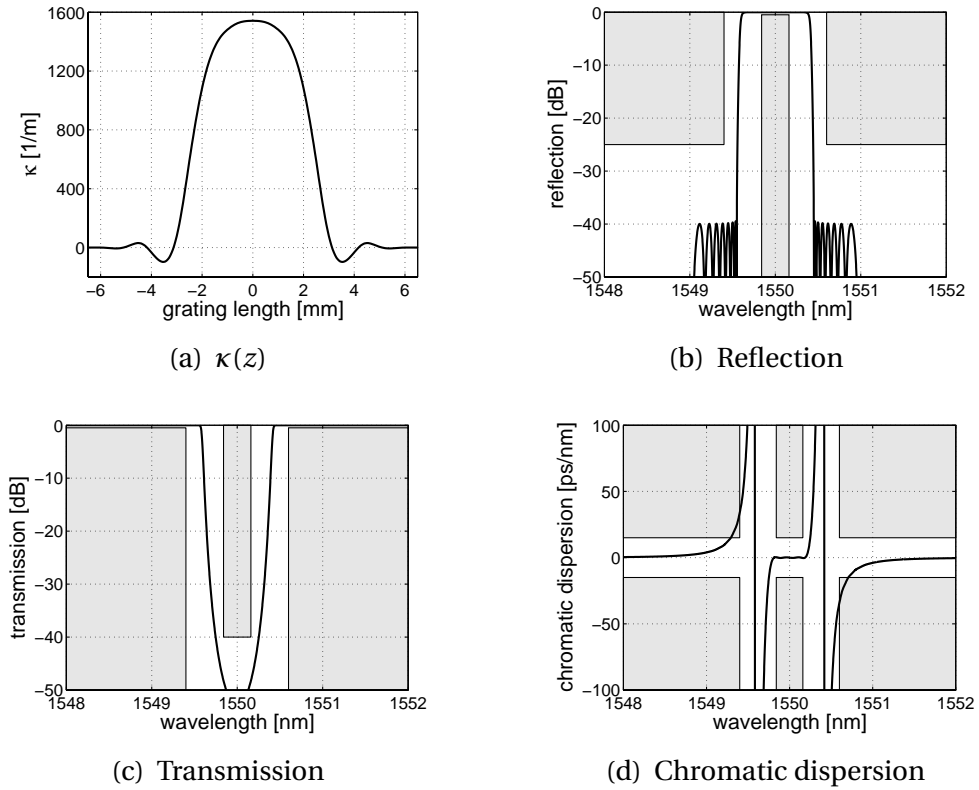


**Figure 6.10.:** 13 mm long Bragg grating design  $\kappa(z)$  for a 100 GHz channel spacing and corresponding transmission/reflection/chromatic dispersion spectra. For this design the specifications for the chromatic dispersion in transmission were not taken into account.

to realize or not realizable at all. It is therefore interesting to know, to what extend the specifications can be fulfilled without  $\pi$ -phase shifts. Whereas such a constraint-based grating design is not possible with the current layer peeling algorithms, this can easily be incorporated into the developed optimization algorithm. The result of a design run, where only positive  $\kappa(z)$  values were allowed, is shown in Fig. 6.11. Due to the omission of the  $\pi$ -phase shifts the necessary length could be further reduced to 7 mm.

The transmission and reflection characteristics are not strongly affected by this constraint. However, the situation is different for the chromatic dispersion, where now both the specifications in transmission and reflection are slightly missed. The comparison of grating designs with and without  $\pi$ -phase shifts yields that the incorporation of phase shifts enable additional degrees of freedom for the shaping of the dispersion curves. Bragg gratings without  $\pi$ -phase

#### 6.4. Bragg grating design by optimization algorithm

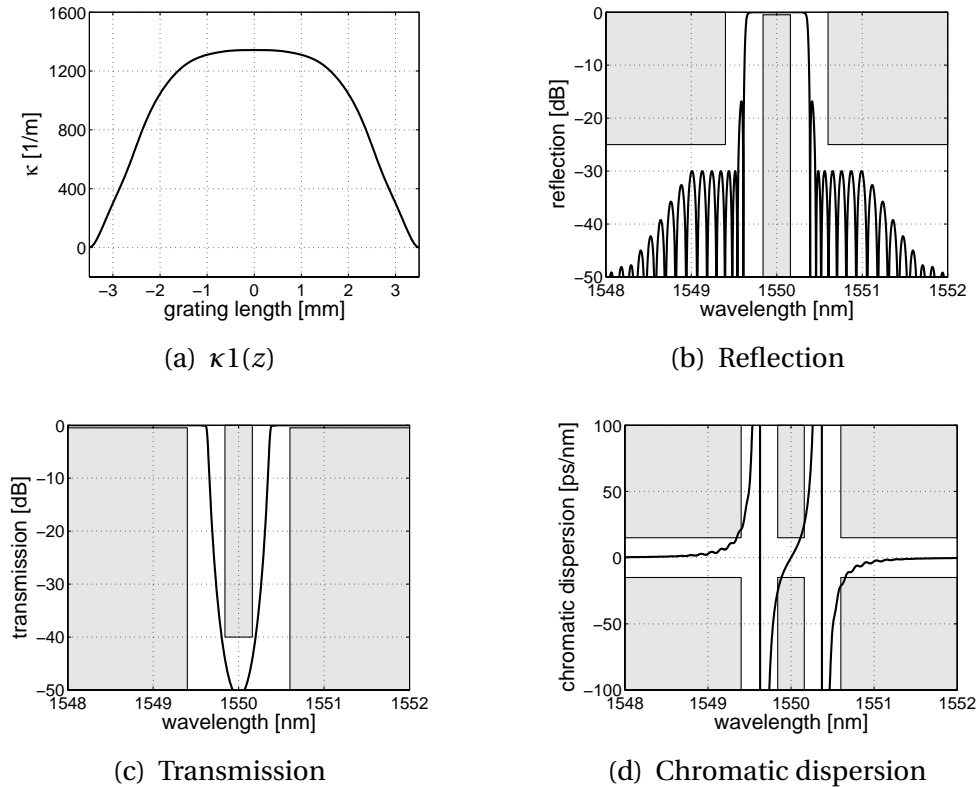


**Figure 6.11.:** 7 mm long Bragg grating design  $\kappa(z)$  with no  $\pi$ -phase shifts for a 100 GHz channel spacing and corresponding transmission/reflection/chromatic dispersion spectra. This design represents the best achieved compromise regarding the dispersion in transmission and reflection.

shifts, however, are easier to fabricate. Further discussions with systems designers will have to show if the values reached for such gratings are still sufficient for deployment.

Also other constraints imposed by the writing setup used can be taken into account by using the optimization algorithm developed. The width of the writing beam, which limits the maximum spatial frequencies of the grating structure, is implemented by an averaging of  $\kappa(z)$ . By setting a limit for the modulus of  $\kappa(z)$  the finite photosensitivity of the material system used is accounted for.

## 6. Design and realization of Bragg gratings

### 6.5. Writing setup

The writing setup used for the fabrication of the Bragg gratings presented in this thesis is sketched in Fig. 6.12. The arrangement is based on the combination of two-beam interferometry with phase mask technique and differential optical phase-shifting [169]. A detailed description of the whole setup is given in [80].

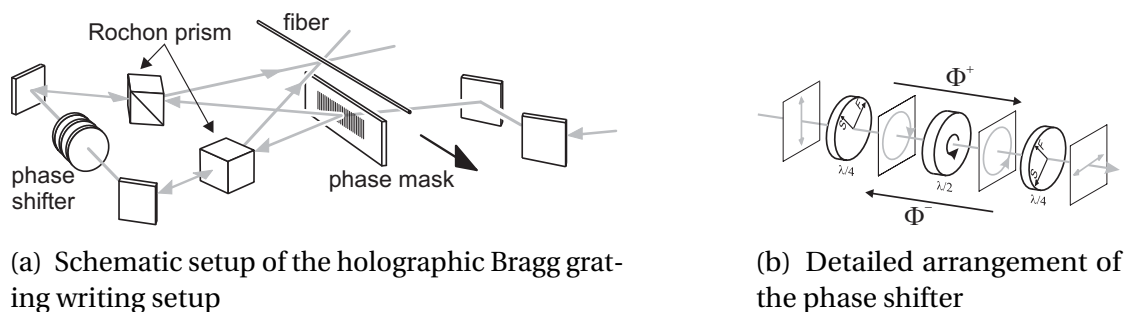


**Figure 6.12.:** Holographic Bragg grating writing setup used [80].

The writing system is basically a Sagnac interferometer with additional polarization rotating/splitting and phase shifting components. The fiber to be illuminated and the beam-splitting phase mask are mounted on a common translation stage. This enables the fabrication of Bragg gratings up to the length of the phase mask used. All the other components shown in Fig. 6.12(a) are fixed in their position.

The incident vertically polarized UV laser beam is diffracted by the phase mask. The 1<sup>st</sup> order diffracted beams then pass through their respective Rochon prism. Inside the phase shifter the polarization of the beams is rotated by 90°. This results in a deflection of the beams at the second Rochon prism. By this means the requirement of a spatial separation between the interference pattern and the phase mask is fulfilled.

The phase shifter (see Fig. 6.12(b)) consists of two crossed quarter-wave plates with a motorized rotating half-wave plate in between. This arrangement introduces a phase delay for the transmitted waves which depends on the angular position of the half-wave plate and on the propagation direction:  $\Phi^+ / 2 = -\Phi^- / 2$ . This enables the setting of a variable and reset-free phase difference between the two counter-propagating waves:  $\Phi = \Phi^+ / 2 - \Phi^- / 2 = 4\Theta$ , where  $\Theta$  denotes the rotation angle of the half wave plate.

The capability provided by the phase shifter is used for three different purposes:

**Windowing of the coupling coefficient  $\kappa(z)$**  By applying a rapidly alternating angular movement of the half-wave plate a reduced contrast of the UV-induced refractive index modulation inside the fiber can be achieved. This enables a windowing of  $\kappa(z)$  while keeping the effective index constant. A special case of this capability is the introduction of  $\pi$ -phase shifts along the grating length, which enables the realization of  $\kappa(z)$  with negative values even if only positive refractive index changes can be achieved. Examples for the windowing of  $\kappa(z)$  and the introduction of  $\pi$ -phase shifts can be found in sections 6.6.1 and 6.6.2.

**Bragg wavelength shift and chirp** By choosing a constant rotation of the half-wave plate it is possible to realize a refractive index modulation other than given by the phase mask and still obtain a full contrast of the index modulation. Gratings with a Bragg wavelength shift of  $\pm 28$  nm have been fabricated this way (see section 8.4.2 in [80]). If the angular speed of the half-wave plate is varied during the writing process, chirped Bragg gratings can be realized.

**Correction of errors due to the translation stage** The pitch error of the translation stage yields a non-constant phase of the coupling coefficient. As this error is of a systematic nature, it can be compensated by a proper rotation sequence of the phase shifter. Examples of obtained  $\kappa(z)$  distributions with and without this phase correction are given in [169].

A GF4AA fiber from NUFERN and etched channel waveguides in material system A1 were used for all of the following writing experiments. In order to enhance the photosensitivity the fibers and planar waveguide samples were hydrogen loaded at 300 bar and room temperature for at least 10 days.

## 6.6. Realization in fibers

In [80] it was already shown that Bragg gratings with complex  $\kappa(z)$  distributions can be realized with the above mentioned setup. However the grating strength was always kept quite low (3... 12 dB) in these experiments. In order to check the

## 6. Design and realization of Bragg gratings

performance of the writing setup, Bragg gratings with identical grating profiles and decreasing writing velocity (corresponding to increasing writing fluence) were fabricated. Whenever it was possible to reconstruct the written grating profiles (using OFDR and an inverse scattering solver, see section 4.7), they were compared with the design.

Fibers were chosen for this task because of their high homogeneity of the refractive index distribution (important for the effective index of the fundamental mode) and of the photosensitivity. Any deviations of the obtained coupling coefficient distributions from the intended design are therefore caused by the writing facility. In addition the available fibers have already been proven to be highly photosensitive. UV-induced refractive index changes up to  $16 \times 10^{-3}$  and an almost linear relation between fluence and index change up to  $8 \times 10^{-3}$  have been measured for the fiber used [62, 170]. However these experiments were performed with a fringeless UV-exposure so that changes of the mean refractive index were measured. It will be shown in the next sections that such large values can also be obtained in combination with a high contrast of the index modulation.

### 6.6.1. Bragg gratings without $\pi$ -phase shifts

Based on an early design for Bragg gratings without phase shifts (similar to the one shown in Fig. 6.11) a series of Bragg gratings were fabricated. The writing velocities  $v$  used were 7/3.5/2/1/0.75/0.5/0.25 mm/min, respectively. The corresponding transmission and reflection spectra are presented in Fig. 6.13. The spectrum for the 2 mm/min grating is not shown because of a malfunction of the control program towards the end of the writing process. Strong gratings could be easily fabricated. In the case of 0.25 mm/min writing velocity the minimum transmission was appreciably below -80 dB, which is even beyond the dynamic range of our measurement setup (tunable laser source with low source spontaneous emission and power meter).

Only the three fastest written gratings were weak enough for reconstruction of the spatial grating structure. Their reconstructed coupling coefficients and the design are shown in Fig. 6.14(a). The high peak towards the end of the 2 mm/min grating was caused by the aforementioned malfunction. Whereas out of normal transmission or reflection spectra, no useful information can be obtained from such gratings, OFDR followed by an inverse scattering algorithm can still determine the spatial grating structure. To compare the grating shapes

## 6.6. Realization in fibers

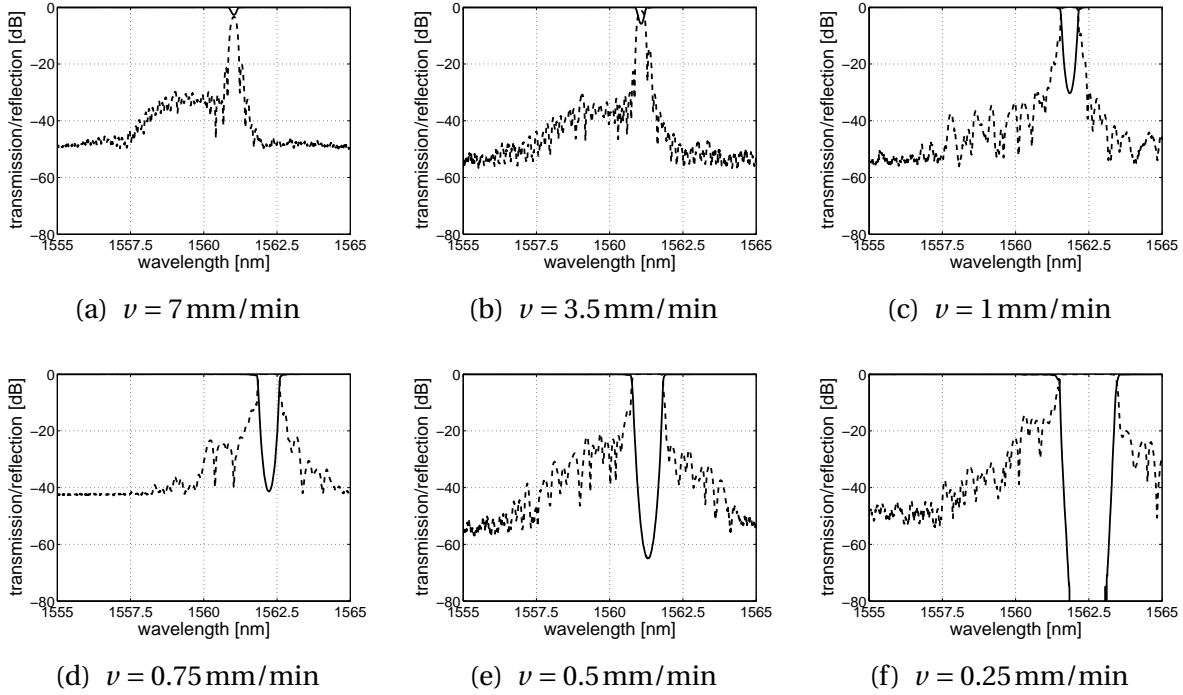


**Figure 6.13.:** Transmission and reflection spectra (solid/dashed line) of UV-written fiber Bragg gratings realized with different writing velocities ( $\nu = 2$  mm/min omitted).

a normalized representation is given in Fig. 6.14(b). This shows that the required grating shape can be realized.

In order to test if the required values for the coupling coefficient can be achieved with the fiber and writing setup used, the grating strength of the written Bragg gratings was determined. For the weak and moderate gratings the reconstructed values from Fig. 6.14(a) were used. The grating strengths of the stronger gratings were obtained by a visual best fit (taking into account transmission depth and 3 dB reflection bandwidth) of the measured spectra and a grating calculation with a linear scaling of the reconstructed 3.5 mm/min profile. These values yielded a linear dependence relation between writing fluence and the coupling coefficient up to the maximum value of  $\kappa \sim 4000 \text{ m}^{-1}$ , corresponding in an UV-induced refractive index modulation of  $\delta n_G \approx \pm 4 \times 10^{-3}$ . Therefore, no saturation effects have to be taken into account for the realization of the intended Bragg gratings. These experiments have shown that the required grating shapes and values for  $\kappa(z)$  can be achieved in hydrogen-loaded GF4AA fibers with the holographic writing setup used.

## 6. Design and realization of Bragg gratings

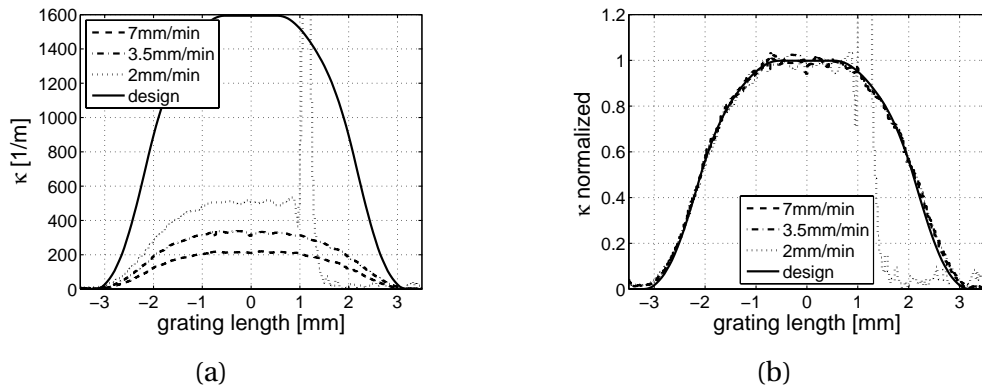


**Figure 6.14.:** Comparison of reconstructed grating profiles without  $\pi$ -phase shifts with the intended design.

In Fig. 6.15 the measured spectral characteristics of a 7 mm long Bragg grating with no  $\pi$ -phase shifts are shown in combination with the specifications. This grating was written with a scanning velocity of 0.5 mm/min and was best in terms of fulfilling the specifications. For an easier comparison of the measured spectra with the specifications and the design, the Bragg wavelength was manually aligned to a full nanometer value.

A good agreement of the measured spectra with the design (Fig. 6.11) was obtained. The grating is stronger, and due to this also broader, than required. Nevertheless most of the specifications are fulfilled. The transmission specifications are completely satisfied. In reflection the required suppression of -25 dB was not fully achieved, especially on the short wavelength side. As expected from the design section the chromatic dispersion specifications are only partially fulfilled. The most problematic characteristic is the chromatic dispersion in transmission near the edges of the grating stop band, where the specifications are exceeded by a factor of 10. No chromatic dispersion values in transmission are shown around the Bragg wavelength, as there is nearly no transmitted power. The chromatic dispersion in reflection is only a factor of two too high and, apart from the ripples, according to the design.

The fact that the two chromatic dispersion spectra from both sides of the grating nearly coincide proves that the the grating structure is spatially symmetric. The origin of the observed ripples is not known at the moment. As the chromatic dispersion is calculated by a differentiation of the measured group delay values small ripples (as shown in Fig. 4.7(a) for a SMF patch cord) can

## 6.6. Realization in fibers

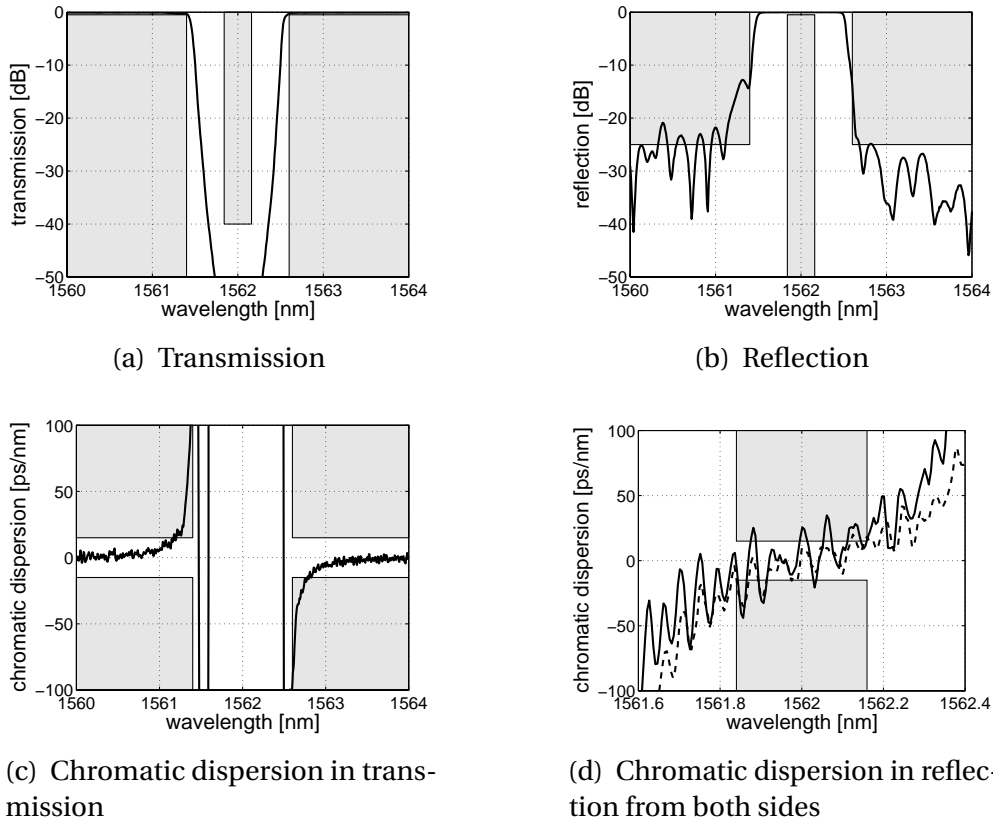


**Figure 6.15.:** Transmission/reflection and chromatic dispersion spectra of a 7 mm long Bragg grating without  $\pi$ -phase shifts. The gray regions denote violations of the system specifications.

already have a significant impact on the chromatic dispersion values. It can, however, not be excluded that the ripples are caused by the grating structure, too. The periodicity corresponds to a Fabry-Pérot resonator of 1.6 cm in glass, but no such resonator could be found in the measurement setup used.

In conclusion it can be stated that high-quality fiber Bragg gratings can be fabricated. The required specifications can mostly be fulfilled, even without the need of  $\pi$ -phase shifts.

### 6.6.2. Bragg gratings with $\pi$ -phase shifts

It was shown in section 6.4.2 that by incorporating  $\pi$ -phase shifts into the coupling coefficient the dispersion characteristics of Bragg gratings can be improved. The writing setup introduced in section 6.5 is able to realize such structures.

## 6. Design and realization of Bragg gratings

As was the case for the gratings without  $\pi$ -phase shifts, first a series of weak gratings was written in order to compare the realized profiles with the design. This comparison showed that the writing setup used is capable to realize the required complicated grating profiles very closely. Based on these experiences Bragg gratings with the required grating strength were written into hydrogen-loaded GF4AA fibers.

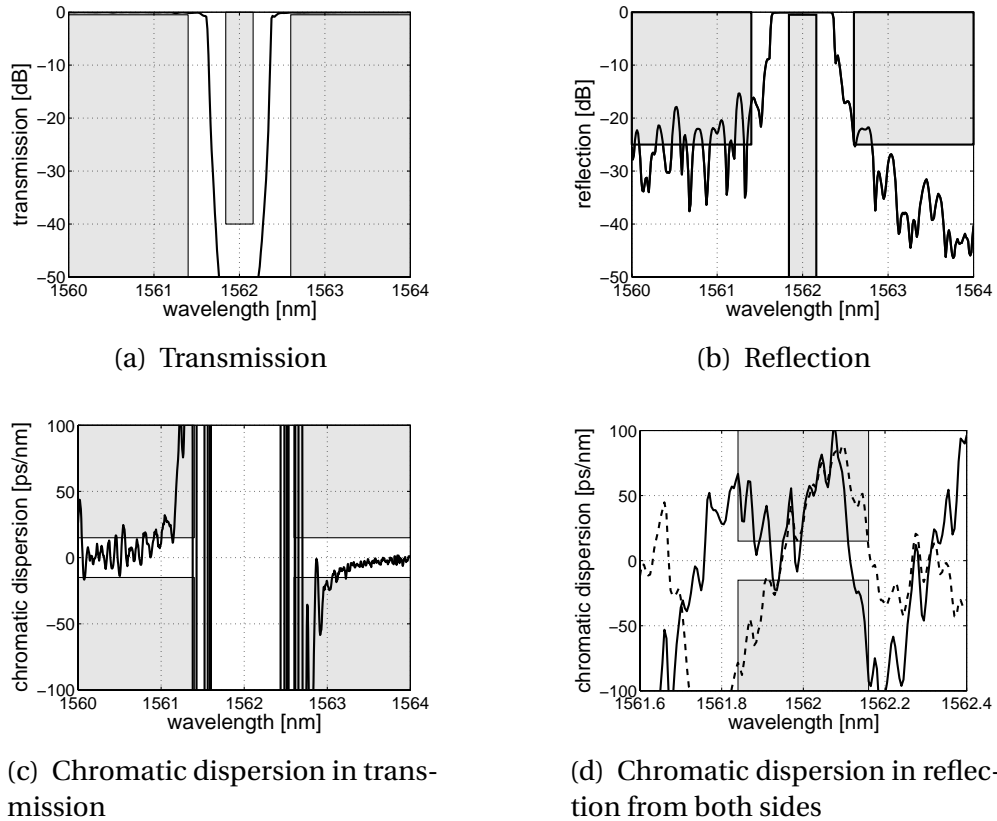


**Figure 6.16.:** Transmission/reflection and chromatic dispersion spectra of a 13 mm long Bragg grating with  $\pi$ -phase shifts. The gray regions denote violations of the system specifications.

The measured spectral characteristics of the best realized Bragg grating with  $\pi$ -phase shifts are shown in Fig. 6.16. The grating is 13 mm long, was written with a scanning velocity of 0.25 mm/min and was realized according to the design in Fig. 6.9. For the display here, the Bragg wavelength was again manually aligned to a full nanometer value.

This grating is also stronger than required. The transmission and reflection properties are slightly better compared to the grating in Fig. 6.15 and fulfill most

## 6.7. Realization in channel waveguides

of the specifications. On the short wavelength side the required suppression in reflection of -25 dB was slightly missed. Contrary to the design, the chromatic dispersion properties of this Bragg grating are worse compared to the results shown in Fig. 6.15 for a grating with no  $\pi$ -phase shifts. In addition, the chromatic dispersion curves from both sides are different here. The intended spatial symmetry is therefore not fulfilled for this grating. Once again no chromatic dispersion values in transmission are shown around the Bragg wavelength, as there is nearly no transmitted power.

In conclusion it can be stated that the advantages offered by the incorporation of  $\pi$ -phase shifts could not be transferred from the design to the fabrication so far. More work is needed in order to improve the quality of strong Bragg gratings with  $\pi$ -phase shifts.

## 6.7. Realization in channel waveguides

In the previous sections it was shown that the holographic writing setup used is capable of writing high quality Bragg gratings in fibers. The next step was the realization of such gratings in planar waveguide structures. The planar waveguide samples were etched channel waveguides in silica-on-silicon (material system A1, see appendix D and Fig. 5.3(a)).

In some earlier work it was already shown that strong Bragg gratings can be fabricated inside etched channel waveguides by the scanning phase mask technique [133, 171]. The detection of the grating strength was limited by the dynamic range of the equipment then in use, but transmission dips in excess of -25 dB for 10 mm long uniform Bragg gratings have been achieved. As no OFDR setup in connection with an inverse scattering algorithm was available at that time, no information about the spatial structure of the Bragg gratings written could be obtained.

A comparison between UV-written Bragg gratings in a fiber and in an etched channel waveguide is given in Fig. 6.17. Both gratings have about the same transmission dip, but from a comparison of the writing velocities used it follows that the planar waveguide material has a lower photosensitivity. A ten-fold increase of the writing fluence is necessary in order to reach the same grating strength.

One way to increase the writing fluence is a lower scanning velocity. By writing point gratings (the translation stage is not moved, yielding grating struc-

## 6. Design and realization of Bragg gratings

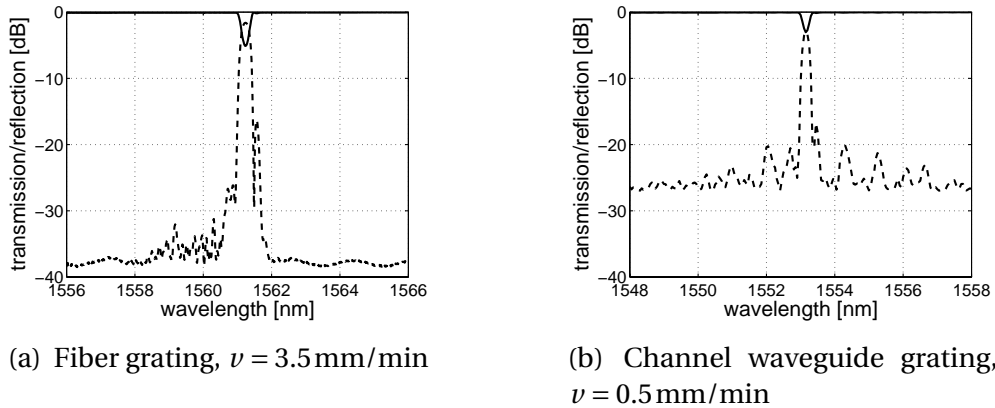


**Figure 6.17.:** Transmission/reflection spectra (solid/dashed line) of Bragg gratings written in a fiber and an etched channel waveguide. The higher floor in the reflection measurement of the etched channel waveguide is caused by the fiber–waveguide transition and not by the Bragg grating.

tures of the size of the static interference pattern) maximum values for  $\kappa(z)$  of  $\sim 4000 \text{ m}^{-1}$  were achieved. However, an irradiation time of about 1000 s was necessary. In order to achieve the required grating strength (-40 dB transmission dip) writing times of more than 3 h would be necessary for the 7 mm long Bragg grating design. As two identical gratings have to be fabricated, this is not a practical approach because of the outdiffusion of the hydrogen. Increasing the writing fluence by increasing the power density is not possible because of the damage threshold of the Rochon prism used in the writing setup.

Within the framework of the PLATON project Bragg gratings were also written in the same material system at the Institute for Physical High Technology, Jena (IPHT) and Institute for Systems and Computer Engineering of Porto (INESC). In both setups no damage endangered components were present, so that higher power densities could be used. Bragg gratings with a transmission dip of more than -40 dB were realized with the design shown in Fig. 6.11 [172].

As both gratings presented in Fig. 6.17 were rather weak, it was possible to reconstruct the spatial grating structure. Modulus and phase of  $\kappa(z)$  for both gratings are compared in Fig. 6.18. The flat curves for the phase distributions indicate that both the effective index of the fundamental mode of the pristine waveguides and the mean UV-induced refractive index increases in both waveguides were constant along the grating location (-3 to 3 mm). The comparison of the local grating strength revealed that the fiber grating profile has the intended

## 6.7. Realization in channel waveguides

shape but the channel grating waveguide profile is spatially structured. The periodicity is not related to any moving part of the setup used. Such a spatial structuring was present for all Bragg gratings written in etched channel waveguides within the framework of this thesis, however, the shape of the structuring differed between the samples.

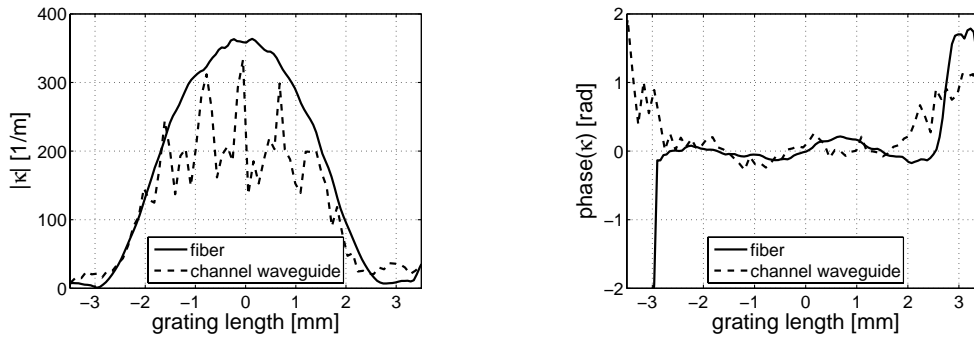


**Figure 6.18.:** Comparison of reconstructed grating profiles (modulus and phase) in a fiber and an etched channel waveguide.

For the weak gratings shown the consequences of a spatially structured coupling coefficient are not visible. Fig. 6.19 shows the calculated transmission and reflection spectra of the fiber and the channel waveguide grating when their coupling coefficient is linearly scaled by a factor of 5.5. The most prominent differences are the transmission depth and the out-of-band rejection, which is lower than 10 dB for the grating inside the etched channel waveguide. This low out-of-band rejection was also experimentally observed in the strong gratings fabricated by INESC and IPHT and limited the performance of the final OADM.

All of the gratings presented so far were written with a frequency-doubled argon ion laser. In Fig. 6.20 the measured transmission/reflection spectra and the reconstructed coupling coefficient of a Bragg grating written in the same material system but with a 193 nm excimer laser<sup>2</sup> are shown. No significant spatial structuring of the coupling coefficient was observed. The writing setup used for this experiment, however, was limited to fabrication of uniform Bragg gratings. No grating structures according to the designs from section 6.4.2 could be realized with it.

<sup>2</sup>Bragg grating writing performed by Vincent Beugin (Université des Sciences et Technologies de Lille)

## 6. Design and realization of Bragg gratings

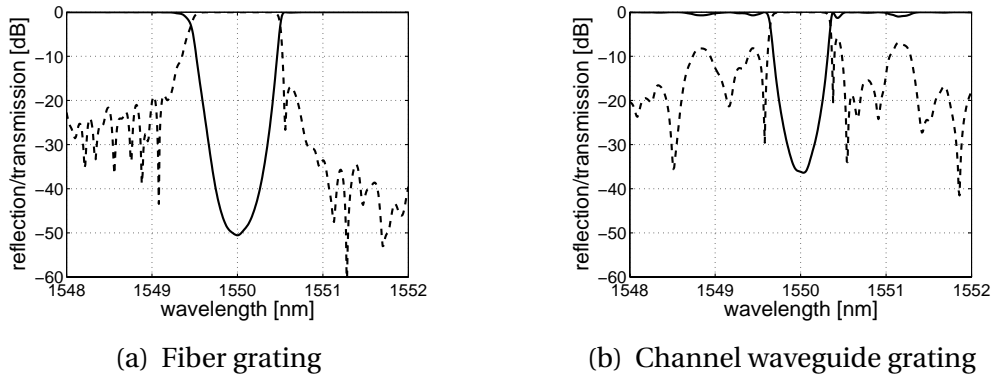


**Figure 6.19.:** Simulated transmission and reflection spectra (solid/dashed line) for the scaled reconstructed grating profiles of Fig. 6.18.

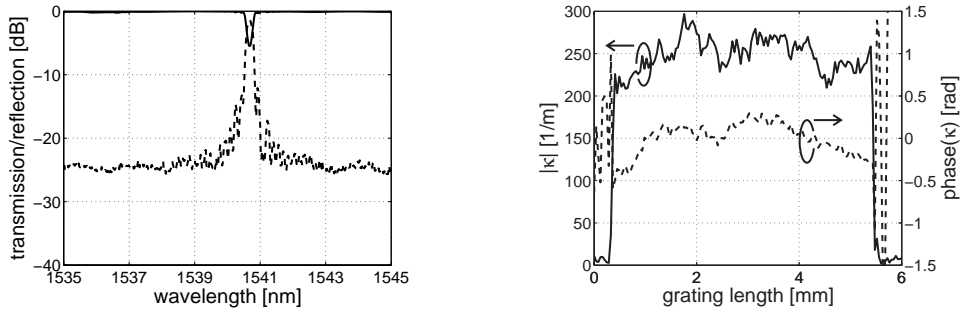


**Figure 6.20.:** Transmission/reflection spectra (solid/dashed line) and reconstructed coupling coefficient of a Bragg grating written with a 193 nm excimer laser into an etched channel waveguide.

The reason for the spatial structuring is still unknown at the moment. One origin could be the interference of back-reflected light from the silicon substrate with the incident light, in connection with variations of the optical thickness of the buffer/core/cladding layer. One possibility to inhibit this interference is the use of a short coherence length laser, as done for the grating shown in Fig. 6.20. However, with a value of 100...200  $\mu\text{m}$  the coherence length of the laser used is still larger than the propagation difference of the interfering waves ( $2 \times 15 \mu\text{m}$  in silica). A second possibility to prevent the aforementioned interference is reported in [173]. By placing the waveguide sample at a  $4^\circ$  angle with respect to the phase mask and using a tightly focussed laser beam, interference between the incident and back-reflected waves was avoided. This method, however, requires a specially designed phase mask, where the interference pattern is located at a given working distance behind the mask.

## 6.8. Conclusion

In this chapter three different approaches for the design of low chromatic dispersion Bragg gratings were presented. With the commercial Bragg grating design program it was not possible to design Bragg gratings, which fulfill the given specifications from both sides. This condition is automatically fulfilled for spatially symmetric grating structures. Such structures were obtained by using a spectrally assisted layer peeling algorithm, resulting in a design which nearly fulfills all required specifications. All required specifications were satisfied by the designs obtained with an optimization algorithm. This method also enables the design of Bragg gratings which are fully adapted to the material systems and writing facility used. Bragg grating designs are shown with different lengths and with/without  $\pi$ -phase shifts.

The Bragg gratings designed were fabricated afterwards by using a holographic writing setup which enables full control over local grating strength and period. The Bragg gratings fabricated mostly fulfilled the required specifications in transmission and reflection, but the chromatic dispersion properties have to be improved. The photosensitivity of the planar waveguide samples was found not to be sufficient to realize the required grating strength with the available writing setup. In addition to the lower photosensitivity, an unwanted spatial structuring of the realized Bragg gratings inside the etched channel waveguides was observed. It was shown that this phenomenon prevents the fabrication of strong, high-quality Bragg gratings.

## 7. Conclusion

Within this thesis the use of UV-induced refractive index changes for waveguide structuring and Bragg gratings was demonstrated.

The direct writing technique uses a focussed UV-laser which is scanned over the waveguide sample. By means of a two axis translation stage arbitrary waveguide structures can be produced.

The standard material systems for this fabrication technique are germanium-doped silica films sandwiched between two non-photosensitive layers. In order to enhance the photosensitivity the samples were hydrogen-loaded prior to UV-irradiation. UV-induced refractive index changes up to  $10 \times 10^{-3}$  were achieved in such material systems. The fiber-waveguide coupling losses were reduced to  $< 0.1$  dB by using an index-matched material system. Low loss straight waveguides ( $< 0.3$  dB/cm) and S-bends were produced. The combination of these two building blocks enabled the fabrication of directional couplers. Due to the asymmetry of the waveguides inside the coupling region no full overcoupling was achieved.

Devices based on multi-mode waveguides can also be realized with the direct writing technique. As an example the fabrication of multi-mode interference couplers was shown.  $1 \times 2$ ,  $1 \times 3$  and  $1 \times 4$  splitters with high-quality images have been experimentally realized on the basis of BPM designs.

During experiments with non-hydrogen-loaded samples it was also observed that their boron-phosphorus-doped cladding layer was highly photosensitive. The achieved refractive index changes of up to  $9 \times 10^{-3}$  were even higher than in the subjacent germanium-doped core layer. The photosensitivity was found to be dependent on the boron concentration. Contrary to the germanium-doped layers, hydrogen-loading decreases the photosensitivity. Based on this finding, waveguides were realized in an all germanium free layered material system without any pretreatment.

Germanium-doped silica layers deposited by MDECR-PECVD exhibited a large negative photosensitivity. Without any presensitization refractive index changes down by  $-10 \times 10^{-3}$  were observed. Waveguides were realized in this

material system by the negative direct writing technique, i. e. the waveguide cladding instead of the core was written. Several experiments were performed in order to explain these large refractive index changes. UV-absorption changes and material expansion can explain a large, but not the full part of the measured refractive index changes. More puzzling is the fact that the refractive index reductions, calculated from UV-absorption changes and material expansion, get stronger with increasing writing velocity, whereas the the opposite is true for the measured refractive index changes. More experiments are needed in order to solve this discrepancy.

Channel waveguides were also fabricated in bulk glasses by the direct writing technique. Refractive index increases in non-hydrogen-loaded samples of up to  $5 \times 10^{-3}$  were achieved. Directly UV-written buried X-shaped waveguides in a bulk multicomponent silicate glass have been produced by a special X-shaped writing geometry. The writing technique presented is also suitable to produce waveguides at variable depths, which dive under the surface and may crop out at certain locations. This might be of interest for sensor applications.

The UV-induced refractive index changes offer a great potential for post processing or trimming of integrated optical components. As an example the fabrication-induced phase errors of arrayed waveguide gratings have been reduced using UV-trimming of the individual grating waveguides. Phase error compensation up to 5 rad and a crosstalk reduction by 8 dB down to -35 dB have been achieved without hydrogen loading. In addition the chromatic dispersion within the 1 dB window of the transmission spectrum was reduced from -0.7 to 0.1 ps/nm. Therefore, the complex transmission characteristic of the arrayed waveguide grating has been improved by reducing phase fluctuations of the grating waveguides.

All these results have shown that the direct writing technique is a promising technique for the fabrication of waveguide structures in a variety of different material systems. In order to use the direct writing technique in a commercial environment the photosensitivity decrease due to the hydrogen outdiffusion has to be counteracted. This can be either done by cooling the sample down to  $-30^\circ\text{C}$  during the writing process or by photosensitivity locking techniques. This problem is less detrimental for trimming applications, where the photosensitivity of non-hydrogen-loaded samples should be sufficient.

The second part of this thesis dealt with the design and fabrication of Bragg gratings. It was shown that layer-peeling is well suited for the reconstruction of Bragg gratings from the measured complex reflection factor, but only has limited

## 7. Conclusion

use for the design process when specifications from both grating sides have to be fulfilled. This prerequisite is automatically satisfied when the grating structure is spatially symmetric. For this purpose an algorithm was developed which yields a spectrum, fulfilling the given specifications and belonging to a spatially symmetric Bragg grating. This spectrum is then used as the input spectrum for the layer-peeling algorithm. By using this spectrally assisted layer-peeling algorithm a design was obtained which nearly fulfills all required specifications.

All required specifications were satisfied by the designs obtained with an optimization algorithm. This algorithm also allowed for the consideration of constraints imposed by the writing facility. The constraints which can be taken into account are the grating length, existence of  $\pi$ -phase shifts, maximum values and maximum spatial frequencies for the coupling coefficient. This enables the design of Bragg gratings which are fully adapted to the material systems and writing facility used. Bragg grating designs are shown with different lengths and with/without  $\pi$ -phase shifts. Through the choice of the weighting factors  $q_i$  certain spectral characteristics can be emphasized. As an example a Bragg grating was designed, whose chromatic dispersion in transmission outside the grating stop band was not considered.

The designed Bragg gratings were fabricated afterwards by using a holographic writing setup which enables full control over local grating strength and period. Through the reconstruction of weak Bragg gratings it was shown that the designs can be realized in optical fibers. More work, however, is needed to improve the quality of strong Bragg gratings, especially if they contain  $\pi$ -phase shifts. The required specifications in transmission and reflection were mostly fulfilled, but the chromatic dispersion characteristics in reflection and transmission have to be improved.

The photosensitivity of the planar waveguide samples was found not to be sufficient to realize the required grating strength with the available writing setup. Due to the damage threshold of the Rochon prism inside the setup the power density could not be increased. For the future a focussing after the prism should be considered. In addition to the lower photosensitivity, an undesired spatial structuring of the realized Bragg gratings inside the etched channel waveguides was observed. It was shown that this phenomenon prevents the fabrication of strong, high-quality Bragg gratings.

The results presented show that the methods developed in this thesis are highly efficient for fabrication of complex waveguide devices and Bragg gratings in photosensitive optical materials.

# A. Photosensitivity of amorphous aluminium oxide

The work presented in this chapter was done in cooperation with the institute of Micro Systems Technology at the Technische Universität Hamburg-Harburg, where the fabrication of the material samples and the non-optical characterization experiments were performed. The aim was to investigate the photosensitivity of amorphous aluminium oxide.

## A.1. Motivation

There is a constant search going on for new optical materials, which can be used for integrated optical waveguides. Aluminium oxide is a promising material because of its low absorption values ( $< 0.3$  dB/cm between 1000 and 1800 nm after tempering) and high refractive index ( $n = 1.66 \dots 1.78$ ). In addition it is a good host material for metal or rare earth ions like titanium, chromium or erbium [174].

Waveguides were defined in this material system as strip-loaded waveguides. First a  $3 \mu\text{m}$  thick buffer layer was realized by thermal oxidization of the silicon substrate. An aluminium oxide layer with a thickness of 600 nm and a silica layer of thickness 400 nm were deposited on top of the buffer layer by plasma-enhanced chemical vapor deposition (PECVD). By means of photolithography and etching processes the thickness of the silica layer outside the waveguide regions was decreased to 200 nm. A general description of the processing steps used is given in [174], whereas the detailed parameters can be found in [175].

Two different samples (M1, M2: see appendix D) were used for the UV-irradiation experiments. No waveguiding in the slab and strip-loaded waveguides was observed for sample M1, but was observed for sample M2. For the writing experiments the setup described in section 5.2 was used. The incident power was 50 mW and the beam was focussed onto the sample surface by a 10 mm lens to a  $1/e^2$ -diameter of about  $4 \mu\text{m}$ . Straight lines with writing veloci-

## A. Photosensitivity of amorphous aluminium oxide

ties of 0.25 to 2000  $\mu\text{m/s}$  were written. The writing experiments were performed on wafer regions where no strip-loaded waveguides were present.

## A.2. Results

All UV-written lines on sample M1 were visible under an optical microscope. In the Linnik interferometer measurements an increase of the optical path length in the UV-written line was observed, see Fig. A.1(a). The lines shown were written with velocities of 10/25/50/100/250/1000  $\mu\text{m/s}$ , respectively (left to right). These positive phase shifts can either be caused by a refractive index increase, a positive surface expansion or a combination of both. Measurements of the surface profile performed with an atomic force microscope (AFM) revealed that the UV-irradiation yielded surface trenches as shown in Fig. A.1(b). This trench was written with a velocity of 2000  $\mu\text{m/s}$  and has a depth of  $\sim 50$  nm.

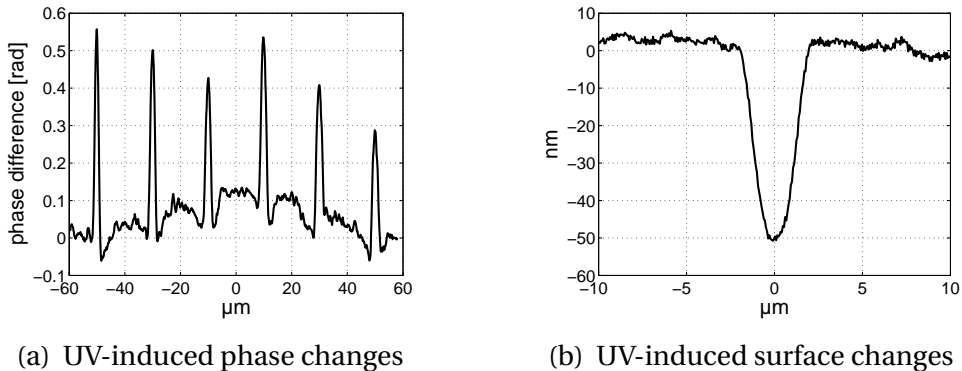


**Figure A.1.:** Measurement results on UV-irradiated areas on sample M1.

The reason for the positive phase shifts has therefore to be caused by a refractive index increase either in the silica or in the aluminium oxide layer. Measurements of refractive index changes by means of the refracted near-field method were not possible because of the small thicknesses of the two layers. Attempts were therefore made to remove the silica layer by chemical etching. For this, the samples were put into a 50 % HF-acid solution for one minute. Standard PECVD-deposited aluminium oxide has a very low etching rate (below 20 nm/min [174]), so it was expected that no significant thickness changes of the aluminium oxide layer occur. The results obtained with the samples used, however, were different.

In Fig. A.2 scanning electron microscope (SEM) pictures of the resulting surface are shown. Both the silica and the aluminium oxide layer were etched away. An exception were the UV-irradiated lines, where now ribs are present. AFM measurements have shown that these ribs have the original 600 nm height of the aluminium oxide layer. Depending on the writing velocity the width of the ribs is between 2 and 5.5  $\mu\text{m}$ .

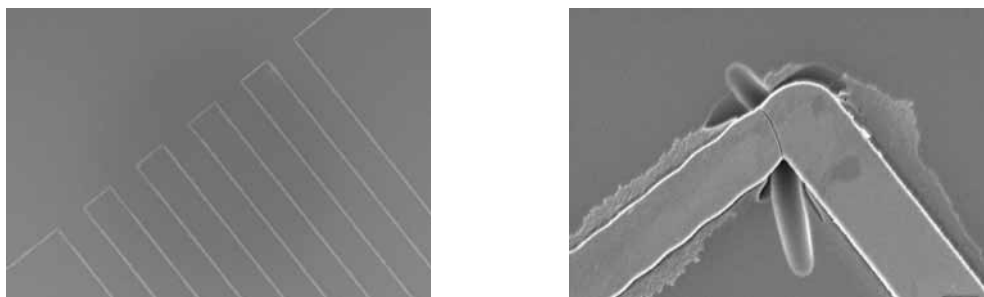


**Figure A.2.:** Scanning electron microscope pictures of ribs produced by etching of the UV-irradiated areas on sample M1. In the right picture cracks and an under-etching are visible at a turning point of the UV laser.

The writing experiments on sample M2 resulted in an irregular appearance of dark dots on the UV-irradiated areas. The etching with HF-solution only removed the silica layer and no signs of the UV-irradiated areas were present on the aluminium oxide surface.

Two conclusions can be drawn from these results. First, the aluminium oxide deposited for sample M1 had a different chemical composition than the one for sample M2. Second, the UV-irradiation yielded a change of the chemical composition of sample M1, so that the etching rate was reduced. The reason for this behavior is still unclear.

In order to find the origin of this behavior several experiments were performed with pristine samples M1, M2 and UV-irradiated areas on sample M1. In SEM measurements no visible difference between the aluminium oxide layers on sample M1 and M2 were detected. Measurements of the chemical composition of sample M1 and M2 using energy dispersive X-ray spectroscopy yielded, that the carbon content in sample M1 was higher than in sample M2. On UV-irradiated areas on sample M1 however no carbon was present anymore. After the etching of sample M1, hollow spaces were visible on SEM pictures of the end faces of the resulting ribs. These could be the result of a carbon outdiffusion.

### *A. Photosensitivity of amorphous aluminium oxide*

The UV-induced changes of the chemical etching rate could be the basis for a promising structuring method of aluminium oxide layers. For use as optical waveguides the optical properties of the resulting waveguide structures have to be checked. A big problem could be scattering losses due to the surface roughness. Other applications could be found in the area of micro systems.

## **B. Thermal stability of directly UV-written waveguides**

One of the most important prerequisite for using UV-induced refractive index changes in commercial available devices is a sufficient stability over the lifetime. Typical specifications for the lifetime are 20 years at ambient temperatures between -20 and 80 °C. Lifetime predictions are mostly based on accelerated testing experiments, in which devices are stressed at extreme conditions (for instance temperature, humidity, mechanical stresses) for a short time. From the measured degradations of device characteristics a model is build in order to predict the behavior over decades under moderate stress [176]. For the case of UV-induced refractive index changes these stresses are introduced by high temperatures [177], which are applied in either isochronal or isothermal fashion [178] or by using a continuous temperature ramp method [179].

Whereas the aging characteristics of Bragg gratings in various fiber types have been extensively studied, only a small number of temperature stability experiments were performed on UV-written waveguide structures [180,181]. The samples used in those publications were hydrogen-loaded germanium-doped silica on silicon samples.

It was shown in section 5.6 that large UV-induced refractive index changes can also be obtained in non hydrogen-loaded germanium-free boron phosphorus doped silica layers. These index changes were used for the patterning of waveguide structures. A decrease of the UV-induced index changes will result in changes of the mode field, which will influence e. g. bending losses or the coupling ratio of directional couplers.

In order to compare the stability of the UV-induced refractive index changes in the two different layers, waveguides with different UV-powers and writing velocities were fabricated in sample A1 (see Fig. 5.16(a)). The core layer consists of germanium doped silica, whereas the the cladding layer is made of boron phosphorus doped silica. With these samples isochronal annealing experiments were performed. The heating times were 30 min/8 h/24 h, respectively. After each temperature rise the samples cooled down to room temperature and the

## B. Thermal stability of directly UV-written waveguides

refractive index changes in both layers were measured by the refracted near-field method. The normalized index changes versus the annealing temperature for one set of writing conditions are shown in Fig. B.1. The UV-induced refractive index changes both in the core and in the cladding layer decrease with increasing temperature.

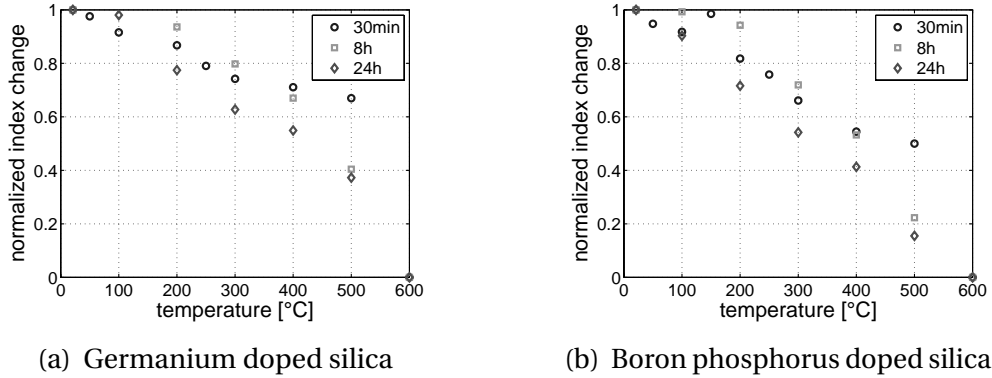


**Figure B.1.:** Decrease of normalized UV-induced refractive index changes during an isochronal annealing experiment.

In order to predict the stability of the refractive index changes under normal temperature conditions a master curve has to be build out of these results. The master curve formalism enables the calculation of the decrease of the refractive index changes over time and the definition of a burn-in process. Such a burn-in process ensures that the changes over time stays within a given limit. An example for such a procedure is given in [182]. Due to the limited number of data points and as the accuracy of the refractive index measurement is only  $3 \times 10^{-4}$  no master curve could be obtained for our material systems.

As it can be seen in Fig. B.1 the thermal behavior of both material systems is very similar. More work has to be done in order to make quantitative statements regarding the lifetime of refractive index changes in boron phosphorus doped silica layers.

## C. Fiber Bragg grating characterization by Optical Space Domain Reflectometry

This work was performed in cooperation with the Fiber Optics Research Center (FORC) at the General Physics Institute of the Russian Academy of Sciences. Results of this cooperation are published in [17] and [18].

### C.1. Motivation

Fiber Bragg gratings (FBGs) are widely used for telecommunication and sensor systems. In some cases it is important to know the axial distribution of the grating parameters as well as the exact grating location in the fiber. This is especially true, if the desired specifications are not fulfilled. The knowledge of the grating structure properties is an essential prerequisite for solving of the responsible problems.

The most common and simplest way of the grating characterization is measuring its power transmission/reflection spectrum. This method determines only the integral characteristics of the grating structure. To obtain the spatial distribution of local grating properties other techniques such as the Optical Low Coherence Reflectometry (OLCR) [183], side-diffraction [184, 185] or heat-scan [186] can be used. The Optical Frequency Domain Reflectometry followed by an inverse scattering solver, see section 4.7, offers a fast and accurate determination of the complex coupling coefficient. However this approach requires a lot of technical equipment (tunable laser source, polarization controller, fast AD converter card) and sophisticated algorithms for the evaluation of the sampled data. The Optical Space Domain Reflectometry (OSDR) has less demanding requirements on the hardware and the evaluation.

In previous experiments a He-Ne laser has been used to locally introduce a small optical phase perturbation in the grating structure. Because of the small absorption of this radiation type by silica glass, the tested grating had to be covered with an absorbing layer, typically with limited longitudinal homogeneity.

### C. Fiber Bragg grating characterization by OSDR

Within the framework of the aforementioned cooperation the application of more suitable laser sources (a CO-laser and a frequency-doubled Ar-ion laser) for local induction of a phase perturbation was investigated.

## C.2. Measurement principle

The complex reflection factor  $r(\tilde{\nu})$  is related to the complex reflection coefficient  $\kappa(z)$  by the following equation (see section 2.2.2):

$$r(\tilde{\nu}) = - \int_0^{L_g} \kappa(z) e^{-j2\pi\tilde{\nu}z} dz - p(\tilde{\nu}). \quad (\text{C.1})$$

The term  $p(\tilde{\nu})$  accounts for multiple reflections within the grating structure and can be omitted if the grating is sufficiently weak. This is either the case, when  $|\kappa(z)|$  is sufficiently small, or the operating wavelength is sufficiently distanced from the Bragg wavelength, resulting in a sufficiently large  $|\tilde{\nu}|$ . The technique presented tries to satisfy the latter condition, see Fig. C.1(a).

The OSDR technique for spatial characterization of grating properties is based on the introduction of a local AC phase perturbation  $\delta\Phi_p/2$ , which is scanned along the grating and measuring the reflection/transmission variations at a fixed wavelength outside the stop band. The measurement setup used is sketched in Fig. C.1(b). Both the UV and the IR laser beams used for phase perturbation were chopped with a frequency of  $\sim 230$  Hz and the OSDR signal was detected by a lock-in amplifier.

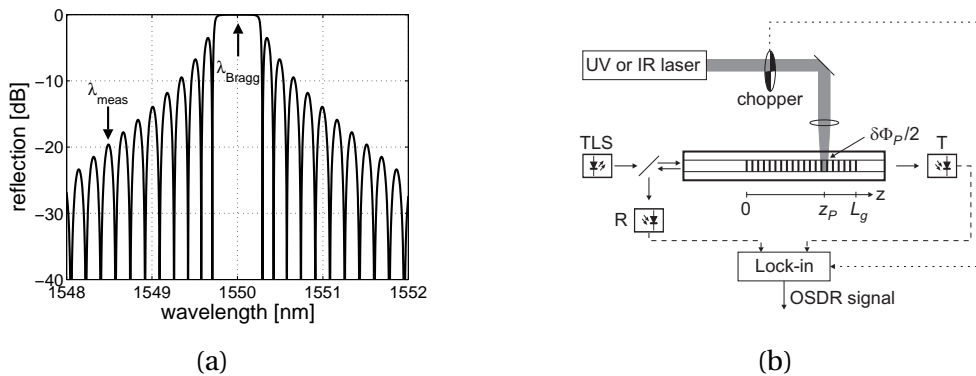


**Figure C.1.:** Location of measuring wavelength with respect to the Bragg wavelength and OSDR measurement setup.

From the measured transmission variations the coupling coefficient  $\kappa(z)$  can be calculated using the following formula [187]:

$$\begin{aligned} \frac{\partial T(z_P; \tilde{\nu}_{\text{meas}})}{\partial z_P} &= \frac{\partial [1 - R(z_P; \tilde{\nu}_{\text{meas}})]}{\partial z_P} = -r^*(\tilde{\nu}_{\text{meas}}) \cdot \frac{\partial \Delta r(z_P; \tilde{\nu}_{\text{meas}})}{\partial z_P} - c. c. \\ &= 2|r(\tilde{\nu}_{\text{meas}})| \delta\Phi_P |\kappa(z_P)| \cdot \cos[2\pi\tilde{\nu}_{\text{meas}}z_P - \phi_\kappa(z_P) + \phi_{0\tilde{\nu}}]. \end{aligned} \quad (\text{C.2})$$

The obtained signal is a cosine function, where the varying amplitude determines the modulus of  $\kappa(z)$  and the argument the phase of  $\kappa(z)$ .

### C.3. Experiments

Instead of the previously used He-Ne laser either a frequency-doubled Ar-ion laser ( $\lambda = 244 \text{ nm}$ ) or a CO-laser ( $\lambda \sim 5 \mu\text{m}$ ) was used here. The penetration depth of CO-laser radiation into silica glass is 100–200  $\mu\text{m}$  which allows one to heat the fiber cross-section with good uniformity. The UV-light of the Ar-ion laser induces a transient optical phase perturbation directly in the fiber core [188]. In both cases no additional absorbing coating is required and the spatial resolution and uniformity of phase changes are improved. In addition these radiation types can induce a rather large phase which increases the sensitivity of the method.

Highly reflecting Bragg gratings written in a hydrogen loaded single-mode fiber (SMF-28) have been tested in these experiments. The gratings were written at FORC with a frequency-doubled Ar-ion laser by means of a Lloyd interferometer. The resulting Bragg gratings therefore had a half-gaussian shape. The length was about 5 mm.

It should be noted that the radiation types used here can permanently change the refractive index distribution. The CO-laser radiation at high power can heat the fiber strongly which can lead to annealing of the induced index, whereas UV-irradiation can induce an additional average index change. Therefore the irradiation dose, which depends on the irradiation density and the scan speed, should be small in order to avoid grating degradation. On the other hand, these effects could be used intentionally for modification of the grating structure.

During the grating testing UV and IR power densities were used that did not lead to perceptible permanent changes of the grating's overall spectrum. For the UV-laser, the power density was  $\sim 30 \text{ W/cm}^2$ , that resulted in a cumulated UV-dose of about  $700 \text{ J/cm}^2$  per scan. This dose yields permanent refractive index

### C. Fiber Bragg grating characterization by OSDR

changes of about  $\Delta n_{\text{ind}} \sim 2 \times 10^{-5}$ , which is relatively small compared to the mean refractive index change induced in the fiber during the grating preparation of  $\Delta n_{\text{mean}} \sim 10^{-3}$ . In the case of the CO-laser irradiation the introduced phase shift provided measurable change of the grating transmission spectrum and was estimated as 0.14 rad. This phase value corresponds to a heating temperature of about 30 °C which is much less than the annealing temperature of the UV-induced index. Thus for weak Bragg gratings with a small  $\Delta n_{\text{mean}}$  in the order of  $10^{-4}$  the CO-laser irradiation seems to be the more appropriate solution.

## C.4. Results and discussion

An OSDR trace measured for a detuning  $\Delta\lambda \approx 1.5$  nm of the probe laser wavelength from the central grating wavelength is plotted in Fig. C.2(a). The grating position corresponds to the region between 1 and 6 mm in the trace where the signal oscillations are clearly visible. The number of OSDR oscillations in the trace is defined by the detuning and was selected in order to be suitable for qualitative processing of the measured OSDR signal.

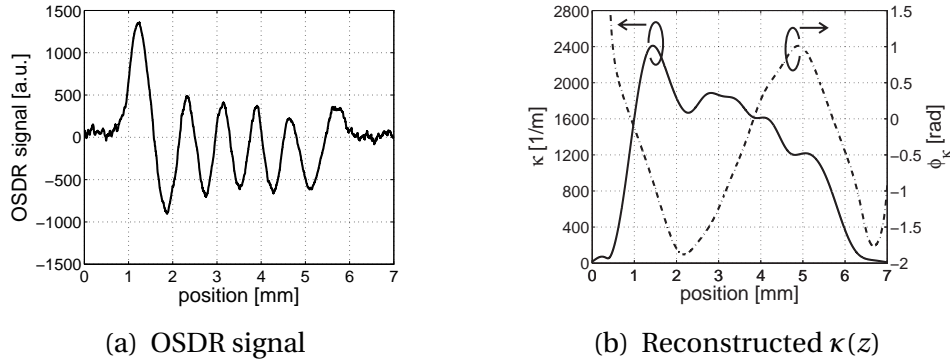


**Figure C.2.:** OSDR-signal measured for CO-laser light excitation and modulus and phase of the grating coupling coefficient  $\kappa(z)$  reconstructed from the OSDR-data.

From the measured OSDR signal the axial distributions of modulus  $|\kappa(z)|$  and phase  $\phi_{\kappa}(z)$  of the coupling coefficient are calculated using eq. (C.2) and shown in Fig. C.2(b). The modulus of the coupling coefficient is related to the amplitude of the refractive index modulation as  $|\kappa(z)| = \eta\pi\Delta n_{\text{mod}}(z)/\lambda_0$ , where  $\eta$  is the overlap between the fundamental mode and the transverse refractive index changes structure of the Bragg grating. The latter relation allows one to obtain  $n_{\text{mod}}(z)$ .

#### C.4. Results and discussion

Fig. C.3(a) shows the axial distribution of the induced index modulation measured by different methods (OSDR techniques with IR and UV excitation as well as with the side-diffraction technique using a He-Ne laser). Coincidence within 10–15 % deviation between these curves has been achieved.

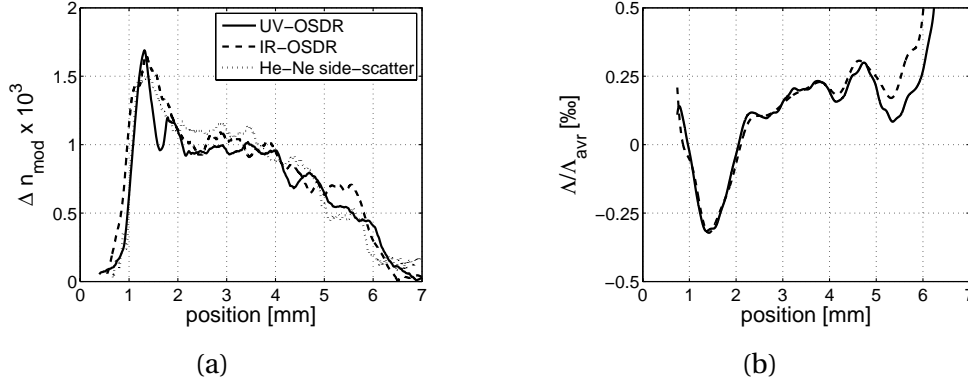


**Figure C.3.:** Comparison of the obtained modulation amplitude distributions measured by UV- and IR-OSDR techniques as well as by side-diffraction technique and relative period distributions for two different IR-OSDR measurements.

The spatial derivative of the phase is related to the grating parameters as

$$\frac{d\phi(z)}{dz} \approx 2\pi \left[ 2n_{\text{eff}}^0 \frac{\Delta\lambda}{\lambda_0^2} + \frac{2\Delta n_{\text{eff}}(z)}{\lambda_0} + \frac{\Delta\Lambda(z)}{\Lambda_{\text{avr}}^2} \right], \quad (\text{C.3})$$

where  $\lambda_0 = 2n_{\text{eff}}^0\Lambda_{\text{avr}}$  is the Bragg resonance wavelength,  $\Delta n_{\text{eff}}(z) = n_{\text{eff}}(z) - n_{\text{eff}}^0$  is the deviation of the local effective index from that of the fundamental mode  $n_{\text{eff}}^0$  and  $\Delta\Lambda(z) = \Lambda(z) - \Lambda_{\text{avr}}$  is the grating period deviation from the average period  $\Lambda_{\text{avr}}$ . The first term in eq. (C.3) is defined by the wavelength detuning  $\Delta\lambda$  and is constant. The second and the third terms are determined by the FBG properties and cannot be obtained independently. Both of them can give a Bragg wavelength shift and special assumptions or experiments have to be made in order to separate these grating parameters. It seems reasonable to assume high contrast in the index modulation and an approximately sinusoidal pitch profile. This assumption gives

$$\Delta n_{\text{avr}}(z) = \Delta n_{\text{mod}}(z), \quad (\text{C.4})$$

where  $\Delta n_{\text{avr}}(z)$  is defined through  $\Delta n_{\text{eff}} = \eta\Delta n_{\text{avr}}(z)$ . Using this assumption and eq. (C.3) the relative variation of the grating period has been calculated and is presented in Fig. C.3(b).

### C. Fiber Bragg grating characterization by OSDR

The importance of the information obtained about the spatial distribution of the grating period is shown in Fig. C.4. With the derived data for the coupling coefficient the transmission spectra of the grating was calculated. Using only the index modulation distribution and falsely assuming the grating period to be constant, only a poor coincidence between the calculated and the measured spectra (dashed and solid lines, respectively) was obtained. Taking into account both the period variation and the index modulation distributions, however, yielded a spectrum (dotted line) close to the measured one (solid line). The fact that the measured spectrum seems to be have a floor at around -20 dB transmsion is caused by the limited dynamic range of the measurement equipment at FORC at that time.

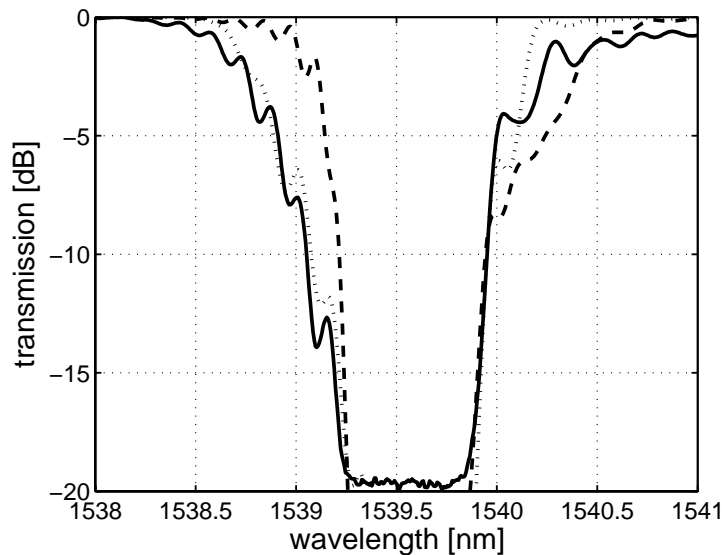


**Figure C.4.:** Comparison of the measured FBG transmission spectrum (solid line), the calculated spectra taking into account the measured  $\Delta n_{\text{mod}}(z)$  (dashed line) only and both  $\Delta n_{\text{mod}}(z)$  and  $\Delta \Lambda(z)$  (dotted line).

## C.5. Conclusion

The original concept of the Optical Space Domain Reflectometry was enhanced by using IR (CO-laser) or UV (frequency-doubled Ar-ion laser) irradiations for inducing the phase perturbation. These irradiation wavelengths do not require an additional coating of the grating with an absorbing layer and yielded improved

### *C.5. Conclusion*

sensitivity, uniformity and spatial resolution. Comparison of obtained  $\Delta n_{\text{mod}}(z)$  distributions with that measured by the side-diffraction technique showed good coincidence within 10–15 % deviation. By taking into account the grating phase information provided by the OSDR technique a satisfactory agreement between calculated and measured grating spectra was obtained.

The OFDR technique in combination with an inverse scattering solver (see section 4.7), however, has proven to be a better solution for the spatial characterization of Bragg gratings. It offers a faster measurement time, a higher spatial resolution and most importantly a higher accuracy of the reconstructed grating profile.

## D. Sample data

Below are data regarding the different material samples mentioned in this thesis. All the values given here were specified by the manufacturer of the respective samples.

### Sample I1

fabricated by: NKT Integration A/S  
deposition method: PECVD  
cladding layer: 12  $\mu\text{m}$  BPSG,  $n = 1.444@1550\text{ nm}$   
core layer: 5.5  $\mu\text{m}$  Ge : B : SiO<sub>2</sub>,  $n = 1.444@1550\text{ nm}$   
buffer layer: 16  $\mu\text{m}$  TOS,  $n = 1.445@1550\text{ nm}$   
substrate: ~ 600  $\mu\text{m}$  silicon

### Sample A1

fabricated by: ALCATEL SEL  
deposition method: FHD  
cladding layer: 20  $\mu\text{m}$  BPSG,  $n = 1.449@1310\text{ nm}$   
core layer: 4.5  $\mu\text{m}$  Ge : SiO<sub>2</sub>,  $n = 1.464@1310\text{ nm}$   
buffer layer: 15  $\mu\text{m}$  TOS,  $n = 1.449@1310\text{ nm}$   
substrate: ~ 1 mm silicon

### Sample A2

fabricated by: ALCATEL SEL  
deposition method: FHD  
cladding layer: 15  $\mu\text{m}$  BPSG,  $n = 1.449@1310\text{ nm}$   
core layer: 4.5  $\mu\text{m}$  Ge : B : SiO<sub>2</sub>,  $n = 1.449@1310\text{ nm}$   
buffer layer: 15  $\mu\text{m}$  TOS,  $n = 1.449@1310\text{ nm}$   
substrate: ~ 1 mm silicon

### Sample J1

fabricated by: Institute for Physical High Technology, Jena  
deposition method: FHD  
cladding layer 2: 12  $\mu\text{m}$  BPSG,  $n = 1.448@1310\text{ nm}$ , low boron concentration  
cladding layer 1: 20  $\mu\text{m}$  BPSG,  $n = 1.448@1310\text{ nm}$ , high boron concentration  
core layer: 5.5  $\mu\text{m}$  Ge : SiO<sub>2</sub>,  $n = 1.4625@1310\text{ nm}$   
buffer layer: 12  $\mu\text{m}$  TOS,  $n = 1.449@1310\text{ nm}$   
substrate: ~ 1 mm silicon

### Sample J2

fabricated by: Institute for Physical High Technology, Jena  
deposition method: FHD  
cladding layer: 9  $\mu\text{m}$  BPSG,  $n = 1.448@1310\text{ nm}$ , low boron concentration  
core layer: 17  $\mu\text{m}$  BPSG,  $n = 1.448@1310\text{ nm}$ , high boron concentration  
buffer layer: 4  $\mu\text{m}$  TOS,  $n = 1.449@1310\text{ nm}$   
substrate: ~ 500  $\mu\text{m}$  silicon

### Sample U1

fabricated by: Laboratoire de Physique des Interfaces et des Couches Minces, Paris  
deposition method: MDECR-PECVD  
cladding layer: 15  $\mu\text{m}$  silica  
core layer: 4.5  $\mu\text{m}$  Ge : SiO<sub>2</sub>  
substrate: ~ 1 mm Suprasil<sup>®</sup>

### Sample U2

fabricated by: Laboratoire de Physique des Interfaces et des Couches Minces, Paris  
deposition method: MDECR-PECVD  
core layer: 4.5  $\mu\text{m}$  Ge : SiO<sub>2</sub>  
substrate: ~ 1 mm Suprasil<sup>®</sup>

#### *D. Sample data*

##### **Sample U3**

fabricated by: Laboratoire de Physique des Interfaces et des Couches  
Minces, Paris  
deposition method: MDECR-PECVD  
cladding layer: 15  $\mu\text{m}$  silica  
substrate:  $\sim 1$  mm Suprasil<sup>®</sup>

##### **Sample M1**

fabricated by: Institute of Micro Systems Technology, TUHH  
deposition method: PECVD  
cladding layer: 200 nm silica  
core layer: 600 nm aluminium oxide  
buffer layer: 3  $\mu\text{m}$  TOS  
substrate:  $\sim 500$   $\mu\text{m}$  silicon

##### **Sample M2**

identical to sample M1 but different process parameters were used

## List of publications

- [1] E. Brinkmeyer, D. Johlen, F. Knappe, and H. Renner. Methods for experimental characterization of UV-written gratings and waveguides. *OSA Trends in Optics and Photonics*, 33:155–175, 2000.
- [2] E. Brinkmeyer, S. Kieckbusch, and F. Knappe. Techniques for characterizing waveguide gratings and grating-based devices (Invited talk). In *Photonics North*, 2006. paper GW-08-1-1.
- [3] S. Kieckbusch, F. Knappe, and E. Brinkmeyer. UV Writing of Accurately Chirped FBGs using in-situ Optical Frequency Domain Reflectometry and Inverse Scattering. In *OSA Topical Meeting on Bragg Gratings, Poling and Photosensitivity*, page 29, 2005.
- [4] F. Knappe, J. Voigt, H. Renner, and E. Brinkmeyer. Direct UV writing of Multimode-Interference Couplers. In *OSA Topical Meeting on Bragg Gratings, Photosensitivity and Poling in Glass Waveguides*, pages 184–186, 2003. paper TuA4.
- [5] F. Knappe, C. Aichele, S. Grimm, M. Alke, H. Renner, and E. Brinkmeyer. Ready-to-use silica slab waveguides for pretreatmentless UV-fabrication of customized Planar Lightwave Circuits. In *OSA Topical Meeting on Bragg Gratings, Poling and Photosensitivity*, page 38, 2005.
- [6] C. Aichele, M. Becker, S. Grimm, F. Knappe, and M. Rothhardt. Eigenschaften dotierter SiO<sub>2</sub>-Wellenleiterschichten für UV-Strukturierungsverfahren zur Realisierung passiver optischer Wellenleiterkomponenten. In *VDE-ITG-Fachausschuss 9.1 - Diskussionsitzung: Messung und Modellierung in der Optischen Nachrichtentechnik*, 2005.
- [7] F. Knappe, G. Girard, B. Poumellec, J.-E. Bourée, D. Dragoë, E. Billi, H. Renner, and E. Brinkmeyer. Waveguide patterning by Directly UV-written trenches. In *OSA Topical Meeting on Bragg Gratings, Poling and Photosensitivity*, page 38, 2005.

## List of publications

- [8] E. Billi, D. Dragoe, B. Poumellec, F. Knappe, H. Renner, E. Brinkmeyer, G. Girard, and J.-E. Bourée. Topographic Study of a Direct UV Patterned Planar Waveguide with Negative Index Change. In *30th Australian Conference on Optical Fibre Technology*, page 45, 2005.
- [9] E. Billi, D. Dragoe, F. Knappe, B. Poumellec, J. Davis, G. Girard, H. Renner, and E. Brinkmeyer. Strong negative index change achieved in H:Ge:SiO<sub>2</sub> for direct UV writing. In *First Conference on Advances in Optical Materials*, 2005.
- [10] G. Manolescu, L. Favaro, F. Knappe, G. Girard, B. Poumellec, H. Renner, and E. Brinkmeyer. Structural transformations induced by direct UV writing in MDECR-PECVD silica layer exhibiting negative index change. In *First Conference on Advances in Optical Materials*, 2005.
- [11] F. Knappe, Y. Menke, F. Grézaud, J. Voigt, H. Renner, M. Ferraris, and E. Brinkmeyer. Buried X-shaped channel waveguides directly UV-written in a multicomponent silicate glass. In *OSA Topical Meeting on Bragg Gratings, Poling and Photosensitivity*, page 38, 2005.
- [12] J. Gehler and F. Knappe. Crosstalk reduction of arrayed waveguide gratings by UV trimming of individual waveguides without H<sub>2</sub>-loading. In *Optical Fiber Communication Conference*, volume 2, pages 236–238, 2000.
- [13] D. Johlen, F. Knappe, H. Renner, and E. Brinkmeyer. UV-induced absorption, scattering and transition losses in UV side-written fibers. In *Optical Fiber Communication Conference and the International Conference on Integrated Optics and Optical Fiber Communication*, volume 3, pages 50–52, 1999. paper ThD1.
- [14] F. Knappe, D. Johlen, M. Grimm, H. Renner, and E. Brinkmeyer. Verlustmechanismen in UV-geschriebenen Wellenleitern. In *100. DGaO Jahrestagung*, 1999. paper P29.
- [15] E. Brinkmeyer and F. Knappe. Variable Fiber-Optic Delay Lines Based on Chirped Gratings. In *Optical Fiber Communication Conference and the International Conference on Integrated Optics and Optical Fiber Communication*, 1999. Workshop W202.

## *List of publications*

- [16] F. Knappe, H. Renner, and E. Brinkmeyer. Efficient design of spatially symmetric Bragg gratings in add-drop multiplexers. In *VDE-ITG-Fachausschuss 9.1 - Diskussionssitzung: Messung und Modellierung in der Optischen Nachrichtentechnik*, 2005.
- [17] I. Korolev, S. Vasiliev, O. Medvedkov, E. Dianov, F. Knappe, Ch. Knothe, H. Renner, and E. Brinkmeyer. Application of UV and IR radiation for spatial characterization of Bragg gratings. In *Bragg Gratings, Photosensitivity, and Poling in Glass Waveguides*, 2001. paper BWA2.
- [18] I. Korolev, S. Vasiliev, O. Medvedkov, E. Dianov, F. Knappe, Ch. Knothe, H. Renner, and E. Brinkmeyer. Spatial characterization of fiber Bragg gratings by Optical Space Domain Reflectometry (OSDR) applying local IR- or UV-light perturbations. In *VDE-ITG-Fachausschuss 9.1 - Diskussionssitzung: Messung und Modellierung in der Optischen Nachrichtentechnik*, 2001.

## Bibliography

- [19] A. E. Wilner, editor. *IEEE Journal of Selected Topics in Quantum Electronics*, 6(6), 2000. Millenium Issue.
- [20] T. H. Maiman. Stimulated optical radiation in ruby. *Nature*, 187(4736):493–494, August 1960.
- [21] K. C. Kao and G. A. Hockham. Dielectric-fiber surface waveguides for optical frequencies. *Proc. Inst. Electr. Eng.*, 113(3):1151–1158, 1966.
- [22] T. Miya, Y. Terunuma, T. Hosaka, and T. Miyashita. Ultimate low-loss single-mode fibre at 1.55  $\mu\text{m}$ . *Electronics Letters*, 15(4):106–108, February 1979.
- [23] R. J. Mears, L. Reekie, I. M. Jauncey, and D. N. Payne. Low-noise erbium-doped fibre amplifier operating at 1.54  $\mu\text{m}$ . *Electronics Letters*, 23(19):1026–1028, 1987.
- [24] H. G. Weber, S. Ferber, M. Kroh, C. Schmidt-Langhorst, R. Ludwig, V. Marembert, C. Boerner, F. Futami, S. Watanabe, and C. Schubert. Single channel 1.28 Tbit/s and 2.56 Tbit/s DQPSK transmission. *Electronics Letters*, 42(3):178–179, 2006.
- [25] S. Bigo, Y. Frignac, G. Charlet, W. Idler, S. Borne, H. Gross, R. Dischler, W. Poehlmann, P. Tran, C. Simonneau, D. Bayart, G. Veith, A. Jourdan, and J.-P. Hamaide. 10.2 Tbit/s ( $256 \times 42.7$  Gbit/s PDM/WDM) transmission over 100 km TeraLight<sup>TM</sup> fiber with 1.28 bit/s/Hz spectral efficiency. In *Optical Fiber Communication Conference*, 2001. paper PD25.
- [26] K. Fukuchi, T. Kasamatsu, M. Morie, R. Ohhira, T. Ito, K. Sekiya, D. Ogasahara, and T. Ono. 10.92-Tb/s ( $273 \times 40$ -Gb/s) triple-band/ultra-dense WDM optical-repeated transmission experiment. In *Optical Fiber Communication Conference*, 2001. paper PD24.

- [27] Y. Chigusa, Y. Yamamoto, T. Yokokawa, T. Sasaki, T. Taru, M. Hirano, M. Kakui, M. Onishi, and E. Sasaoka. Low-loss pure-silica-core fibers and their possible impact on transmission systems. *Journal of Lightwave Technology*, 23(11):3541–3550, 2005.
- [28] M. Yamada. Overview of Wideband Optical Fiber Amplification Technologies. *NTT Technical Review*, 2(12):34–37, 2004.
- [29] P. Bayvel. Future high-capacity optical telecommunication networks. *Philosophical Transactions of the Royal Society Of London Series A: Mathematical, Physical & Engineering Sciences*, 358(1765):303–329, January 2000.
- [30] S. E. Miller. Integrated Optics: An Introduction. *Bell Syst. Techn. J.*, 48(7):2059–2069, 1969.
- [31] M. R. Poulsen, P. I. Borel, J. Fage-Pedersen, J. Hübner, M. Kristensen, J. H. Povlsen, K. Rottwitt, M. Svalgaard, and W. Svendsen. Advances in silica-based integrated optics. *Optical Engineering*, 42(10):2821–2834, 2003.
- [32] K. O. Hill, Y. Fujii, D. C. Johnson, and B. S. Kawasaki. Photosensitivity in optical fiber waveguides: Application to reflection filter fabrication. *Applied Physics Letters*, 32:647–649, 1978.
- [33] G. Meltz, W. W. Morey, and W. H. Glenn. Formation of Bragg gratings in optical fibers by a transverse holographic method. *Optics Letters*, 14:823–825, 1989.
- [34] M. Svalgaard, C. V. Poulsen, A. Bjarklev, and O. Poulsen. Direct UV writing of buried singlemode channel waveguides in Ge-doped silica films. *Electronics Letters*, 30(17):1401–1403, 1994.
- [35] H. Renner. Modes of UV-written planar waveguides. *Optics Letters*, 23(2):111–113, January 1998.
- [36] H. Renner. Effective-index increase, form birefringence and transition losses in UV-side-illuminated photosensitive fibers. *Optics Express*, 9(11):546–560, November 2001.
- [37] A. Yariv and P. Yeh. *Photonics: Optical Electronics in Modern Communication*. Oxford University Press, 6th edition, 2006.

## Bibliography

- [38] M. Yamada and K. Sakuda. Analysis of almost-periodic distributed feedback slab waveguides via a fundamental matrix approach. *Applied Optics*, 26:3474–3478, 1987.
- [39] R. Kashyap. *Fiber Bragg Gratings*. Academic Press, 1999.
- [40] A. Othonos and K. Kalli. *Fiber Bragg Gratings: Fundamentals and Applications in Telecommunications and Sensing*. Artech House Publishers, 1999.
- [41] D. P. Hand and P. S. J. Russell. Photoinduced refractive-index changes in germanosilicate fibers. *Optics Letters*, 15:102–104, January 1990.
- [42] H. G. Limberger, P. Y. Fonjallaz, R. P. Salathé, and F. Cochet. Compaction- and photoelastic-induced index changes in fiber Bragg gratings. *Applied Physics Letters*, 68(22):3069–3071, 1996.
- [43] M. G. Sceats, G. R. Atkins, and S. B. Poole. Photolytic Index Changes in Optical Fibers. *Annual Review of Materials Science*, 23(1):381–410, 1993.
- [44] V. B. Neustruev. Colour centres in germanosilicate glass and optical fibres. *Journal of Physics: Condensed Matter*, 6(35):6901–6936, 1994.
- [45] R. M. Atkins, V. Mizrahi, and T. Erdogan. 248 nm induced vacuum UV spectral changes in optical fibre preform cores: Support for a colour centre model of photosensitivity. *Electronics Letters*, 29(4):385–386, 1993.
- [46] M. J. Digonnet. Kramers-Kronig analysis of the absorption change in fiber gratings. In Michel J. Digonnet and Francois Ouellette, editors, *Doped Fiber Devices, Proc. SPIE Vol. 2841*, pages 109–120, 1996.
- [47] J. P. Bernardin and N. M. Lawandy. Dynamics of the formation of Bragg gratings in germanosilicate optical fibers. *Optics Communications*, 79(3-4):194–199, October 1990.
- [48] C. Fiori and R. A. B. Devine. Ultraviolet irradiation induced compaction and photoetching in amorphous, thermal SiO<sub>2</sub>. *Materials Research Society Symposia*, 61:187–195, 1986.

- [49] C. Z. Tan and J. Arndt. The refractive index of silica glass and its dependence on pressure, temperature, and wavelength of the incident light. In Hari Singh Nalwa, editor, *Silicon Based Material and Devices*, volume 2, chapter 2, pages 51–91. Academic Press, 2001.
- [50] E. M. Dianov, V. M. Mashinsky, V. B. Neustruev, O. D. Sazhin, V. V. Brazhkin, and V. A. Sidorov. Optical absorption and luminescence of germanium oxygen-deficient centers in densified germanosilicate glass. *Optics Letters*, 22(14):1089–1091, July 1997.
- [51] H. Mueller. The theory of photoelasticity. *Journal of the American Ceramic Society*, 21:27–33, 1938.
- [52] R. E. Schenker and W. G. Oldham. Ultraviolet-induced densification in fused silica. *Journal of Applied Physics*, 82(3):1065–1071, 1997.
- [53] F. Dürr. *Laser-induced stress changes in optical fibers*. PhD thesis, École Polytechnique Fédérale de Lausanne, Faculté des sciences et techniques de l'ingénieur STI, Section de microtechnique, (Institut d'imagerie et optique appliquée), 2005.
- [54] D. L. Williams, B. J. Ainslie, J. R. Armitage, R. Kashyap, and R. Campbell. Enhanced UV photosensitivity in boron codoped germanosilicate fibres. *Electronics Letters*, 29(1):45–47, 1993.
- [55] M. Fokine. *Photosensitivity, chemical composition gratings and optical fiber based components*. PhD thesis, Royal Institute of Technology, Stockholm, Department of Microelectronics and Information Technology, Optics Section; Electrum 229; SE-164 40 Kista, 2002.
- [56] G. Meltz and W. W. Morey. Bragg grating formation and germanosilicate fiber photosensitivity. In F. Ouellette, editor, *International Workshop on Photoinduced Self-Organization Effects in Optical Fiber, Proc. SPIE Vol. 1516*, pages 185–199, 1991.
- [57] P. J. Lemaire, R. M. Atkins, V. Mizrahi, and W. A. Reed. High pressure H<sub>2</sub> loading as a technique for achieving ultrahigh UV photosensitivity and thermal sensitivity in GeO<sub>2</sub> doped optical fibres. *Electronics Letters*, 29(13):1191–1193, 1993.

## Bibliography

- [58] R. M. Atkins, P. J. Lemaire, T. Erdogan, and V. Mizrahi. Mechanisms of enhanced UV photosensitivity via hydrogen loading in germanosilicate glasses. *Electronics Letters*, 29(14):1234–1235, 1993.
- [59] G. E. Kohnke, D. W. Nightingale, P. G. Wigley, and C. R. Pollock. Photosensitization of optical fiber by UV exposure of hydrogen loaded fiber. In *Optical Fiber Communication Conference and the International Conference on Integrated Optics and Optical Fiber Communication*, pages PD20/1–PD20/3 Suppl., 1999.
- [60] M. Åslund, J. Canning, and G. Yoffe. Locking in photosensitivity within optical fiber and planar waveguides by ultraviolet preexposure. *Optics Letters*, 24(24):1826–1828, December 1999.
- [61] M. Fokine and W. Margulis. Large increase in photosensitivity through massive hydroxyl formation. *Optics Letters*, 25(5):302–304, 2000.
- [62] D. Johlen, H. Renner, A. Ewald, and E. Brinkmeyer. Fiber Bragg grating Fabry-Perot interferometer for a precise measurement of the UV-induced index change. In *24th European Conference on Optical Communication*, volume 1, pages 393–394, 1998.
- [63] K. I. White. Practical application of the refracted near-field technique for the measurement of optical fibre refractive index profiles. *Optical and Quantum Electronics*, 11(2):185–196, March 1979.
- [64] N. H. Fontaine and M. Young. Two-dimensional index profiling of fibers and waveguides. *Applied Optics*, 38(33):6836–6844, 1999.
- [65] Rinck elektronik. *Refractive Index Profilometer – Technical data*, 2006. also available online [http://www.rinck-elektronik.de/www/pages/technical\\_data.html](http://www.rinck-elektronik.de/www/pages/technical_data.html).
- [66] P. Oberson, B. Gisin, B. Huttner, and N. Gisin. Refracted near-field measurements of refractive index and geometry of silica-on-silicon integrated optical waveguides. *Applied Optics*, 37(31):7268–7272, 1998.
- [67] L. Leick, A. Harpøth, and M. Svalgaard. Empirical model for the waveguiding properties of directly UV-written waveguides. *Applied Optics*, 41(21):4325–4330, 2002.

- [68] M. Svalgaard, A. Harpøth, and T. Rosbirk. Characterization of UV written waveguides with luminescence microscopy. *Optics Express*, 13(13):5170–5178, 2005.
- [69] D. Inniss, Q. Zhong, A. M. Vengsarkar, W. A. Reed, S. G. Kosinski, and P. J. Lemaire. Atomic force microscopy study of uv-induced anisotropy in hydrogen-loaded germanosilicate fibers. *Applied Physics Letters*, 65(12):1528–1530, September 1994.
- [70] E. Chierici, M. C. Didavide, A. Moro, O. Rossotto, and L. Tallone. Direct writing of channel waveguide on a tellurite glass using a focused ultraviolet laser beam. In *Proceedings of 2002 IEEE/LEOS Workshop on Fibre and Optical Passive Components*, pages 24–28, 2002.
- [71] H. Rosenfeldt, Ch. Knothe, J. Cierullies, and E. Brinkmeyer. Evolution of Amplitude and Dispersion Spectra During Fiber Bragg Grating Fabrication. In *Bragg Gratings, Photosensitivity, and Poling in Glass Waveguides*, 2001. paper BWA4.
- [72] S. Kieckbusch, Ch. Knothe, and E. Brinkmeyer. Fast and accurate characterization of fiber Bragg gratings with high spatial and spectral resolution. In *Optical Fiber Communications Conference*, volume 1, pages 379–381, 2003.
- [73] R. Feced, M. N. Zervas, and M. A. Muriel. An Efficient Inverse Scattering Algorithm for the Design of Nonuniform Fiber Bragg Gratings. *IEEE Journal of Quantum Electronics*, 35(8):1105–1115, 1999.
- [74] G. Meltz, W. W. Morey, W. H. Glenn, and D. J. Fritz. UV-induced Bragg gratings in optical fibers and thin-film waveguides. In F. Ouellette, editor, *Photosensitivity and Self-Organization in Optical Fibers and Waveguides*, *Proc. SPIE Vol. 2044*, pages 236–245,
- [75] V. Mizrahi, P. J. Lemaire, T. Erdogan, W. A. Reed, D. J. DiGiovanni, and R. M. Atkins. Ultraviolet laser fabrication of ultrastrong optical fiber gratings and of germania-doped channel waveguides. *Applied Physics Letters*, 63(13):1727–1729, September 1993.
- [76] M. Svalgaard, K. Fjærch, and L. U. Andersen. Variable optical attenuator fabricated by direct UV writing. *Journal of Lightwave Technology*, 21(9):2097–2103, 2003.

## Bibliography

- [77] Coherent Inc. *Coherent Innova 300 FreD*, 2004.
- [78] Micos GmbH. *Ultra Precision Linear Stage UPM160*, 2002.
- [79] National Instruments Corporation. *NI PCI-7344*, 2002.
- [80] Ch. Knothe. *Holographisches Herstellungsverfahren für Bragg-Gitter in UV-sensitiven Wellenleitern*. Dissertation, Technische Universität Hamburg-Harburg, 2004.
- [81] M. Svalgaard. Effect of D<sub>2</sub> outdiffusion on direct UV writing of optical waveguides. *Electronics Letters*, 35(21):1840–1842, 1999.
- [82] K. Fjærch and M. Svalgaard. Symmetrical waveguide devices fabricated by direct UV writing. *IEEE Photonics Technology Letters*, 14(2):173–175, 2002.
- [83] M. Olivero and M. Svalgaard. Direct UV-written broadband directional planar waveguide couplers. *Optics Express*, 13(21):8390–8399, 2005.
- [84] R. Ulrich and G. Ankele. Self-imaging in homogeneous planar optical waveguides. *Applied Physics Letters*, 27:337–339, 1975.
- [85] L. B. Soldano and E. C. M. Pennings. Optical multi-mode interference devices based on self-imaging: principles and applications. *Journal of Lightwave Technology*, 13(4):615–627, 1995.
- [86] P. A. Besse, M. Bachmann, H. Melchior, L. B. Soldano, and M. K. Smit. Optical Bandwidth and Fabrication Tolerances of Multimode Interference Couplers. *Journal of Lightwave Technology*, 12(6):1004–1009, 1994.
- [87] Optiwave Systems Inc. *OptiBPM 6.2*, 2004.
- [88] J. Z. Huang, R. Scarmozzino, and R. M. Osgood. A New Design Approach to Large Input/Output Number Multimode Interference Couplers and Its Application to Low-Crosstalk WDM Routers. *IEEE Photonics Technology Letters*, 10(9):1292–1294, 1998.
- [89] H. Renner. pers. communication.
- [90] M. Kawachi. Recent progress in silica-based planar lightwave circuits on silicon. *IEE Proceedings Optoelectronics*, 143(5):257–262, 1996.

- [91] M. C. Didavide, L. Cognolato, and O. Rossotto. UV written buried waveguide on P-B codoped silica on silicon layer. In *11th European Conference on Integrated Optics*, pages 7–10, 2003.
- [92] A. K. Sheridan, C. B. E. Gawith, G. D. Emmerson, J. A. Milton, P. G. R. Smith, and J. S. Wilkinson. Channel waveguides in ion-exchanged pyrex by direct UV writing. *Optics Communications*, 242:109–114, 2004.
- [93] J. E. Stevens. Electron Cyclotron Resonance Plasma Sources. In O. Popov, editor, *High Density Plasma Sources - Design, Physics and Performance*, pages 312–379. Noyes Publications, 1995.
- [94] J. Pelletier, A. Lacoste, Y. Arnal, T. Lagarde, C. Lincot, and D. Hertz. New trends in DECR plasma technology: applications to novel duplex treatments and process combinations with extreme plasma specifications. *Surface and Coatings Technology*, 139(2-3):222–232, May 2001.
- [95] J. Pelletier and T. Lagarde. Chemical vapor deposition in high-density low-pressure plasmas: reactor scale-up and performance. *Thin Solid Films*, 241(1-2):240–246, 1994.
- [96] D. Daineka, P. Bulkin, G. Girard, J.-E. Bourée, and B. Drevillon. High density plasma enhanced chemical vapor deposition of optical thin films. *The European Physical Journal - Applied Physics*, 26(1):3–9, 2004.
- [97] A. Lacoste, T. Lagarde, S. Bechu, Y. Arnal, and J. Pelletier. Multi-dipolar plasmas for uniform processing: physics, design and performance. *Plasma Sources Science & Technology*, 11(4):407–412, 2002.
- [98] R. Münzer, B. Poumellec, and S. Zheng. Deliverable D21.1: Report on first improvements for wafer, waveguide and thermo-optic switch elaboration. Internal document, PLATON consortium, 2003.
- [99] R. Germann, H. W. M. Salemink, R. Beyeler, G. L. Bona, F. Horst, I. Masarek, and B. J. Offrein. Silicon oxynitride layers for optical waveguide applications. *Journal Of The Electrochemical Society*, 147(6):2237–2241, 2000.
- [100] R. A. Jarvis, J. D. Love, A. Durandet, G. D. Conway, and R. W. Boswell. UV-induced index change in hydrogen-free germane-silicate waveguides. *Electronics Letters*, 32(6):550–552, 1996.

## Bibliography

- [101] A. Durandet, R. Boswell, and D. McKenzie. New plasma-assisted deposition technique using helicon activated reactive evaporation. *Review of Scientific Instruments*, 66(4):2908–2913, April 1995.
- [102] D. Wiesmann, J. Hübner, R. Germann, I. Massarek, H. W. M. Salemink, G. L. Bona, M. Kristensen, and H. Jackel. Large UV-induced negative index changes in germanium-free nitrogen-doped planar SiO<sub>2</sub> waveguides. *Electronics Letters*, 34(4):364–366, 1998.
- [103] J. Canning, D. Moss, M. Åslund, and M. Bazylenko. A study of negative index grating growth in germanosilicate planar waveguides. *Optical and Quantum Electronics*, 31(5 - 7):469–480, July 1999.
- [104] B. Poumellec. pers. communication.
- [105] M. Svalgaard, A. Harpøth, and M. Andersen. The role of local heating in the formation process of UV written optical waveguides. *Optics Express*, 13(20):7823–7831, 2005.
- [106] L. Dong, J. L. Archambault, L. Reekie, P. S. J. Russell, and D. N. Payne. Photoinduced absorption change in germanosilicate preforms: evidence for the color-center model of photosensitivity. *Applied Optics*, 34:3436–3438, June 1995.
- [107] E. M. Dianov, V. G. Plotnichenko, V. V. Koltashev, Y. N. Pyrkov, N. H. Ky, H. G. Limberger, and R. P. Salathé. UV-irradiation-induced structural transformation of germanosilicate glass fiber. *Optics Letters*, 22(23):1754–1756, December 1997.
- [108] J. Davies. pers. communication.
- [109] J. H. Davies. Elastic Field in a Semi-Infinite Solid due to Thermal Expansion or a Coherently Misfitting Inclusion. *Journal of Applied Mechanics*, 70(5):655–660, September 2003.
- [110] T. Augustsson. Bragg grating-assisted MMI-coupler for add-drop multiplexing. *Journal of Lightwave Technology*, 16(8):1517–1522, 1998.
- [111] L. Dong and W. F. Liu. Thermal decay of fiber Bragg gratings of positive and negative index changes formed at 193 nm in a boron-codoped germanosilicate fiber. *Applied Optics*, 36(31):8222–8226, November 1997.

- [112] M. Bazylenko, M. Åslund, and B. Vandenberg. Novel technique for UV-writing of low-loss and high-temperature stable channel waveguides. In *Optical Fiber Communication Conference and the International Conference on Integrated Optics and Optical Fiber Communication. OFC/IOOC '99. Technical Digest*, volume 4, pages 93–95, 1999. paper FE4.
- [113] D. W. J. Harwood, A. Fu, E. R. Taylor, R. C. Moore, Y. D. West, and D. N. Payne. A 1317 nm neodymium doped fluoride glass waveguide laser. In *26th European Conference on Optical Communication*, pages 191–192, 2000.
- [114] L. Ç. Özcan, V. Tréanton, R. Kashyap, and L. Martinu. Direct Laser Ablation Technique For Fabrication Of Optical Waveguides In Amorphous Materials And Nonlinear Crystals. In *OSA Topical Meeting on Bragg Gratings, Poling and Photosensitivity*, 2005.
- [115] L. M. Tong, L. L. Hu, J. J. Zhang, J. R. Qiu, Q. Yang, J. Y. Lou, Y. H. Shen, J. L. He, and Z. Z. Ye. Photonic nanowires directly drawn from bulk glasses. *Optics Express*, 14(1):82–87, January 2006.
- [116] J.-F. Viens, C. Meneghini, A. Villeneuve, T. V. Galstian, E. J. Knystautas, M. A. Duguay, K. A. Richardson, and T. Cardinal. Fabrication and characterization of integrated optical waveguides in sulfide chalcogenide glasses. *Journal of Lightwave Technology*, 17(7):1184–1191, 1999.
- [117] R. V. Ramaswamy and R. Srivastava. Ion-exchanged glass waveguides: a review. *Journal of Lightwave Technology*, 6(6):984–1000, 1988.
- [118] K. Liu and E. Y. B. Pun. Buried ion-exchanged glass waveguides using field-assisted annealing. *IEEE Photonics Technology Letters*, 17(1):76–78, 2005.
- [119] H. Ebendorff-Heidepriem. Laser writing of waveguides in photosensitive glasses. *Optical Materials*, 25(2):109–115, 2004.
- [120] H. Ebendorff-Heidepriem, C. Riziotis, and E. R. Taylor. Novel photosensitive glasses. In *Proc. of the 7th International Otto Schott Colloquium*, pages 54–59, 2002.

## Bibliography

- [121] M. Ferraris, D. Milanese, Q. Chen, Y. Menke, and E. Monchiero. New glasses with high photosensitivity. In Giancarlo C. Righini and Anna Consortini, editors, *19th Congress of the International Commission for Optics: Optics for the Quality of Life, Proc. SPIE Vol. 4289*, pages 111–112, 2003.
- [122] D. Milanese, A. Fu, C. Contardi, E. R. M. Taylor, and M. Ferraris. Photosensitivity and directly UV written waveguides in an ion exchangeable bulk oxide glass. *Optical Materials*, 18(3):295–300, 2001.
- [123] C. B. E. Gawith, A. Fu, T. Bhutta, P. Hua, D. P. Shepherd, E. R. Taylor, P. G. R. Smith, D. Milanese, and M. Ferraris. Direct-UV-written buried channel waveguide lasers in direct-bonded intersubstrate ion-exchanged neodymium-doped germano-borosilicate glass. *Applied Physics Letters*, 81(19):3522–3524, 2002.
- [124] A. Favre, E. Lee, V. Apostolopoulos, C. B. E. Gawith, C. Y. Tai, E. Taylor, Y. Kondo, and F. Koizumi. Fabrication and characterization of UV-written channel waveguides in Bi<sub>2</sub>O<sub>3</sub>-based glass. *Optical Materials*, 27(1):7–13, 2004.
- [125] C. Contardi, E. R. Taylor, and A. Fu. Study of UV-written channels in lead silicate glasses. *Journal of Non-Crystalline Solids*, 291(1-2):113–120, 2001.
- [126] A. K. Mairaj, Ping Hua, H. N. Rutt, and D. W. Hewak. Fabrication and characterization of continuous wave direct UV ( $\lambda = 244$  nm) written channel waveguides in chalcogenide (Ga:La:S) glass. *Journal of Lightwave Technology*, 20(8):1578–1584, 2002.
- [127] H. Renner, R. Ulrich, J. P. Elbers, and C. Glingener. Einmodenfasern. In E. Voges and K. Petermann, editors, *Optische Kommunikationstechnik*, pages 80–213. Springer, 2002. page 95.
- [128] E.-G. Neumann. *Single-Mode Fibers*. Springer-Verlag, 1988. page 67.
- [129] D. Milanese, M. Ferraris, Y. Menke, M. Olivero, G. Perrone, C. B. E. Gawith, G. Brambilla, P. G. R. Smith, and E. R. Taylor. Photosensitive properties of a tin-doped sodium silicate glass for direct ultraviolet writing. *Applied Physics Letters*, 84(17):3259–3261, 2004.

- [130] E. A. J. Marcatili. Dielectric rectangular waveguide and directional coupler for integrated optics. *Bell Syst. Techn. J.*, 48(7):2071–2102, 1969.
- [131] G. D. Maxwell, R. Kashyap, B. J. Ainslie, D. L. Williams, and J. R. Armitage. UV written 1.5  $\mu\text{m}$  reflection filters in single mode planar silica guides. *Electronics Letters*, 28(22):2106–2107, 1992.
- [132] R. Kashyap, G. D. Maxwell, and B. J. Ainslie. Laser-trimmed four-port bandpass filter fabricated in single-mode photosensitive Ge-doped planar waveguide. *IEEE Photonics Technology Letters*, 5(2):191–194, 1993.
- [133] D. Johlen, F. Knappe, A. Bakhtyari, and E. Brinkmeyer. UV-geschriebene Bragg-Gitter für integriert-optische Add-Drop Multiplexer in Germanosilikatglas. In 99. *DGaO Jahrestagung*, 1998. paper P51.
- [134] H. Renner. Up and down UV-trimming of planar directional waveguide couplers: modeling. *IEEE Photonics Technology Letters*, 12(7):825–827, 2000.
- [135] L. Leick, M. Svalgaard, and J. H. Povlsen. Impact of weak index perturbations on 3 dB multi mode interference couplers. In *Proc. Integrated Photonics Research*, 2001. paper IMC3.
- [136] R. A. Jarvis, J. D. Love, and F. Ladouceur. Bend-radius reduction in planar waveguides using UV post-tuning. *Electronics Letters*, 33(10):892–894, 1997.
- [137] T. Naganawa, S. Ueno, and Y. Kokubun. Spectrum response improvement of higher order series coupled microring resonator filter by UV trimming. *IEEE Photonics Technology Letters*, 17(10):2104–2106, 2005.
- [138] M. K. Smit. New focusing and dispersive planar component based on an optical phased array. *Electronics Letters*, 24(7):385–386, 1988.
- [139] C. Dragone. An  $N \times N$  optical multiplexer using a planar arrangement of two star couplers. *IEEE Photonics Technology Letters*, 3(9):812–815, 1991.
- [140] K. Takada, M. Abe, T. Shibata, and K. Okamoto. 1-GHz-spaced 16-channel arrayed-waveguide grating for a wavelength reference standard in DWDM network systems. *Journal of Lightwave Technology*, 20(5):850–853, 2002.

## Bibliography

- [141] K. Takada, M. Abe, T. Shibata, and K. Okamoto. 5 GHz-spaced 4200-channel two-stage tandem demultiplexer for ultra-multi-wavelength light source using supercontinuum generation. *Electronics Letters*, 38(12):572–573, 2002.
- [142] T. Goh, S. Suzuki, and A. Sugita. Estimation of waveguide phase error in silica-based waveguides. *Journal of Lightwave Technology*, 15(11):2107–2113, 1997.
- [143] H. Yamada, H. Sanjoh, M. Kohtoku, K. Takada, and K. Okamoto. Measurement of phase and amplitude error distributions in arrayed-waveguide grating multi/demultiplexers based on dispersive waveguide. *Journal of Lightwave Technology*, 18(9):1309–1320, 2000.
- [144] H. Yamada, K. Takada, Y. Inoue, Y. Hibino, and M. Horiguchi. 10 GHz-spaced arrayed-waveguide grating multiplexer with phase-error-compensating thin-film heaters. *Electronics Letters*, 31(5):360–361, 1995.
- [145] H. Yamada, K. Takada, Y. Inoue, Y. Ohmori, and S. Mitachi. Statically-phase-compensated 10 GHz-spaced arrayed-waveguide grating. *Electronics Letters*, 32(17):1580–1582, 1996.
- [146] H. Yamada, K. Takada, Y. Inoue, K. Okamoto, and S. Mitachi. Low-crosstalk arrayed-waveguide grating multi/demultiplexer with phase compensating plate. *Electronics Letters*, 33(20):1698–1699, 1997.
- [147] D. A. Zauner, J. Hübner, K. J. Malone, and M. Kristensen. UV trimming of arrayed-waveguide grating wavelength division demultiplexers. *Electronics Letters*, 34(8):780–781, 1998.
- [148] K. Takada, Y. Inoue, H. Yamada, and M. Horiguchi. Measurement of phase error distributions in silica-based arrayed-waveguide grating multiplexers by using Fourier transform spectroscopy. *Electronics Letters*, 30(20):1671–1672, 1994.
- [149] J. Gehler and W. Spahn. Dispersion measurement of arrayed-waveguide gratings by Fourier transform spectroscopy. *Electronics Letters*, 36(4):338–339, 2000.

- [150] K. Takada and M. Abe. UV trimming of AWG devices. In *OSA Topical Meeting on Bragg Gratings, Photosensitivity and Poling in Glass Waveguides*, pages 175–177, 2003. paper TuA1.
- [151] K. Takada and M. Abe. Slab-waveguide irradiation of UV laser light for photosensitive phase error compensation of arrayed-waveguide gratings. *IEEE Photonics Technology Letters*, 14(6):813–815, 2002.
- [152] K. Takada, Y. Takada, A. Yokota, and S. Satoh. Metal mask fabrication with an inkjet printer for AWG phase trimming using a photosensitive refractive index change. *IEEE Photonics Technology Letters*, 17(4):813–815, 2005.
- [153] C. R. Giles. Lightwave applications of fiber Bragg gratings. *Journal of Lightwave Technology*, 15(8):1391–1404, 1997.
- [154] J.-L. Archambault and S. G. Grubb. Fiber gratings in lasers and amplifiers. *Journal of Lightwave Technology*, 15(8):1378–1390, 1997.
- [155] R. A. Minasian. Photonic signal processing of microwave signals. *IEEE Transactions on Microwave Theory and Techniques*, 54(2):832–846, 2006.
- [156] A. D. Kersey, M. A. Davis, H. J. Patrick, M. LeBlanc, K. P. Koo, C. G. Askins, M. A. Putnam, and E. J. Friebele. Fiber grating sensors. *Journal of Lightwave Technology*, 15(8):1442–1463, 1997.
- [157] F. Ouellette. Dispersion cancellation using linearly chirped Bragg grating filters in optical waveguides. *Optics Letters*, 12:847–849, 1987.
- [158] A. Yariv. Coupled-mode theory for guided-wave optics. *IEEE Journal of Quantum Electronics*, 9(9):919–933, 1973.
- [159] M. N. Zervas and R. Feced. Synthesis of fiber gratings. In *Optical Fiber Communication Conference*, volume 1, pages 112–114, 2000. paper TuH1.
- [160] L. Noirie. Deliverable D4.1: System specifications. public document, PLATON consortium, 2003.
- [161] Optiwave Systems Inc. *OptiGrating*, 2001.

## Bibliography

- [162] E. Brinkmeyer. Simple Algorithm for reconstructing fiber gratings from reflectometric data. *Optics Letters*, 20(8):810–812, 1995.
- [163] L. Poladian. Group-delay reconstruction for fiber Bragg gratings in reflection and transmission. *Optics Letters*, 22(20):1571–1573, 1997.
- [164] The MathWorks. *lsqnonlin :: Functions (Optimization Toolbox)*, 2006. also available online <http://www.mathworks.com/access/helpdesk/help/toolbox/optim/ug/lsqnonlin.html>.
- [165] J. Skaar and O. H. Waagaard. Design and characterization of finite-length fiber gratings. *IEEE Journal of Quantum Electronics*, 39(10):1238–1245, 2003.
- [166] J. Skaar and K. M. Risvik. A genetic algorithm for the inverse problem in synthesis of fiber gratings. *Journal of Lightwave Technology*, 16(10):1928–1932, 1998.
- [167] N. Plougmann and M. Kristensen. Efficient iterative technique for designing Bragg gratings. *Optics Letters*, 29(1):23–25, 2004.
- [168] R. Storn. *Differential Evolution Homepage*, 2006. <http://www.icsi.berkeley.edu/~storn/code.html>.
- [169] Ch. Knothe and E. Brinkmeyer. Reset-free phase shifter in a Sagnac-type interferometer for control of chirp and apodization of Bragg gratings. In *OSA Topical Meeting on Bragg Gratings, Photosensitivity and Poling in Glass Waveguides*, 2003.
- [170] F. Martens. Messung von UV-induzierten Brechzahländerungen im Germanium dotierten Quarzglas. Studienarbeit, Technische Universität Hamburg-Harburg, 2000.
- [171] D. Johlen. *Bragg Gitter und optische Wellenleiter in UV Schreibtechnik*. Dissertation, Technische Universität Hamburg-Harburg, 1999.
- [172] M. Rothhardt, U. Hübner, C. Aichele, M. Becker, E. Brinkmeyer, F. Knappe, H. Renner, P. Marques, and M. Melo. Deliverable D32.2: Final report on reconfigurable OADM and on devices implementation. Internal document, PLATON consortium, 2005.

- [173] P. Giaccari, S. Doucet, A. Têtu, S. LaRochelle, and M. Morin. Five-Channel Dispersion Compensators Written in Channel Waveguides. In *OSA Topical Meeting on Bragg Gratings, Poling and Photosensitivity*, page 15, 2005.
- [174] M. Mahnke. *Chrom- und Titan-dotiertes Aluminiumoxid zur Herstellung eines abstimmbaren integriert-optischen Lasers*. Dissertation, Technische Universität Hamburg-Harburg, 2003.
- [175] V. Mertens. Untersuchung der UV-Photosensitivität von amorphem Aluminiumoxid mit Hilfe von integriert-optischen Mach-Zehnder-Interferometern. Studienarbeit, Technische Universität Hamburg-Harburg, 2005.
- [176] M. J. LuValle. An approximate kinetic theory for accelerated testing. *IIE Transactions*, 31(12):1147–1156, September 1999.
- [177] T. Erdogan, V. Mizrahi, P. J. Lemaire, and D. Monroe. Decay of ultraviolet-induced fiber Bragg gratings. *Journal of Applied Physics*, 76(1):73–80, July 1994.
- [178] D. Razafimahatratra, P. Niay, M. Douay, B. Poumellec, and I. Riant. Comparison of isochronal and isothermal decays of Bragg gratings written through continuous-wave exposure of an unloaded germanosilicate fiber. *Applied Optics*, 39(12):1924–1933, April 2000.
- [179] J. Rathje, M. Kristensen, and J. E. Pedersen. Continuous anneal method for characterizing the thermal stability of ultraviolet Bragg gratings. *Journal of Applied Physics*, 88(2):1050–1055, July 2000.
- [180] I. J. G. Sparrow, G. D. Emmerson, C. B. E. Gawith, S. P. Watts, R. B. Williams, and P. G. R. Smith. Assessment of waveguide thermal response by interrogation of UV written planar gratings. *IEEE Photonics Technology Letters*, 17(2):438–440, 2005.
- [181] K. Kulstad and M. Svalgaard. Thermal stability of directly UV-written waveguides and devices. In *24th European Conference on Optical Communication*, volume 1, pages 33–34, 1998.
- [182] V. Beugin, P. Niay, and M. Douay. Isochronal annealing of Bragg gratings written in H<sub>2</sub>-loaded or in UV-hypersensitized germano-phosphosilicate

## Bibliography

- planar waveguides: a comparison. *Optics Express*, 13(18):6777–6790, September 2005.
- [183] P. Lambelet, P. Y. Fonjallaz, H. G. Limberger, R. P. Salathé, C. Zimmer, and H. H. Gilgen. Bragg Grating Characterization by Optical Low-Coherence Reflectometry. *IEEE Photonics Technology Letters*, 5(5):565–567, 1993.
- [184] P. A. Krug, R. Stolte, and R. Ulrich. Measurement of index modulation along an optical fiber Bragg grating. *Optics Letters*, 20(17):1767–1769, 1995.
- [185] P.-Y. Fonjallaz and P. Börjel. Interferometric side diffraction technique for the characterisation of fibre gratings. In *Bragg Gratings, Photosensitivity, and Poling in Glass Waveguides*, pages 230–232, 1999.
- [186] N. Roussel, S. Magne, C. Martinez, and P. Ferdinand. Measurement of index modulation along fiber Bragg gratings by side scattering and local heating techniques. *Optical Fiber Technology*, 5(1):119–132, 1999.
- [187] E. Brinkmeyer, G. Stolze, and D. Johlen. Optical space domain reflectometry (OSDR) for determination of strength and chirp distribution along optical fiber gratings. In *Bragg Gratings, Photosensitivity, and Poling in Glass Fibers and Waveguides: Applications and Fundamentals*, pages 33–35, 1997.
- [188] M. B. Danailov, T. Gasmi, and P. Apai. Transient refraction index changes in UV-exposed optical fibres. *Electronics Letters*, 32(5):482–483, 1996.

# Lebenslauf

## Frank Knappe

geboren am 13.Dezember 1972  
in Hagenow

- 06/1991                   Abitur an der Erweiterten Oberschule Boizenburg
- 07/1991 – 06/1992 Wehrdienst als Sanitäter in Hamm, Höxter und Hagenow
- 10/1992 – 07/1998 Studium der Elektrotechnik  
Technische Universität Hamburg-Harburg  
Studienrichtung: Meß-, Steuer- und Regelungstechnik  
Vertiefungsrichtung: Optische Meßtechnik
- 07/1998                   Abschluß als Diplom-Ingenieur
- 07/1998 – 07/2002 Wissenschaftlicher Mitarbeiter  
Technische Universität Hamburg-Harburg  
Arbeitsbereich Optische Kommunikationstechnik
- 07/2002 – 05/2003 Gastwissenschaftler  
Technische Universität Hamburg-Harburg  
Arbeitsbereich Optische Kommunikationstechnik
- 06/2003 – 05/2005 Wissenschaftlicher Mitarbeiter  
Technische Universität Hamburg-Harburg  
Arbeitsbereich Optische Kommunikationstechnik
- 06/2005 – 04/2006 Gastwissenschaftler  
Technische Universität Hamburg-Harburg  
Arbeitsbereich Optische Kommunikationstechnik
- 05/2006 – 10/2006 Entwicklungsingenieur  
adaptif PHOTONICS GmbH, Hamburg
- seit 10/2006            Entwicklungsingenieur  
Gemfire Europe Ltd., Livingston/Großbritannien





